RICE UNIVERSITY

Receiver Function Analysis and Acoustic Waveform Modeling for Imaging Earth's Crust: New Techniques and Their Applications

by

Huafeng Liu

A THESIS SUBMITTED
IN PARTIAL FULFILLMENT OF THE
REQUIREMENTS FOR THE DEGREE

Doctor of Philosophy

APPROVED, THESIS COMMITTEE

Fenglin Niu, Chair
Professor, Earth Science

Richard G. Gordon,
Keck Professor of Geophysics, Earth Science
Department Chair

Colin A. Zelt,
Professor, Earth Science

William W. Symes,
Noah Harding Professor, Computational and
Applied Mathematics

HOUSTON, TEXAS

March 2013

ABSTRACT

Receiver Function Analysis and Acoustic Waveform Modeling for Imaging Earth's Crust: New Techniques and Their Applications

by

Huafeng Liu

The crust is the outer-most layer of the earth with thickness up to 80 km. Massive seismic waveform data have enabled imaging fine crustal structures with the aid of new imaging techniques. In this thesis, I develop seismic imaging techniques to take full advantage of the expanding dataset as well as apply the imaging techniques to understand crustal seismic structures. First, I apply receiver function techniques to image the crustal thickness and average Vp/Vs in Northeast China. I found an uplifted Moho in eastern flank of the Songliao Basin and the Changbaishan region and suggest that dynamic mantle upwelling might be the cause of the observed uplift. With accumulated waveform data available, it becomes possible to extract more subtle structural information from receiver functions. Second, I develop a new technique to robustly estimate crustal seismic azimuthal anisotropy with radial and transverse receiver functions. My colleges and I have applied this technique to estimate the crustal anisotropy in Southeast Yunnan region and found that the significant crustal anisotropy may be caused by lower crust flow in this region. Full-wave based imaging techniques such as reverse time migration and full-wave inversion does not assume flat interfaces or infinite frequency rays as the receiver function techniques do and, hence, are desirable in imaging more complex crustal structures. However, their high computational cost is one of the issues that prevent their practical applications. In the last part, I developed an effective waveform modeling technique to

efficiently simulate wave propagation in acoustic media. With this novel modeling technique, the full-wave based imaging techniques can be accelerated by a factor up to 400%.

ACKNOWLEDGEMENTS

The five-year graduate study and research at Rice University has been the most valuable dates in my life. I have learned tremendously from the students and professors in the Earth Science department. Among them, I am indebted to my thesis advisor, Dr. Fenglin Niu, who has been always helpful in every way possible in both my life and my research. I have been benefited tremendously from his encouragement in developing my own ideas in research. Without his supports and efforts, it would not have been possible to conduct quality researches during my thesis work. I appreciate my thesis committee members, Richard Gordon, Colin Zelt and William Symes, all of who have been guiding my research progress annually with constructive comments. I am also benefited from the informative seminars and thoughtful discussion with my colleagues in the STAR (Seismology and Tectonics at Rice) group. The STAR leader, Dr. Alan Levander, always shares his insights with me and helps me in understanding wave phenomena. I can always absorb knowledge from the talented postdoctoral fellows, Imma Palomeras, Min Chen and Eric Kiser. My all-time labmate, Jeniffer Masy, has been helping me in many aspects of my research. I would like to thank NSF and BGP International, who have been funding my thesis research.

It would not have been possible to complete my thesis without the supports of my families. I appreciate my parents who nurtured me and always support me in the difficult times through my life. I am also grateful to my grandparents, who have introduced me to the world of Geophysics since I was a teenager and guided me through my career. Finally, I dedicate this thesis to my wife, Jingyi Geng, and my son, Zimo Liu, on his way to this world. My wife has been always understanding and supportive to my life and my research, especially during her pregnant time.

TABLE OF CONTENT

Introduction

The crust is the outer-most layer of the earth with perhaps the most complex structures and deformations. Traveling through the crust, seismic waves are unique tools that can image crustal seismic structures. With high-quality waveform data accumulated at existing stations and collected from new acquisitions, the power of constrain in seismic imaging has been increased significantly. To obtain finer seismic images and extract more information in the crust, new techniques need to be developed to take full advantage of the expanding data. In the three chapters of this thesis, I 1) image the crustal structures in Northeast China with receiver function technique and new-released dataset; 2) develop a new technique to estimate crustal azimuthal anisotropy using radial and transverse receiver functions; and 3) innovate an effective waveform-modeling technique that facilitates the applications of high-resolution imaging techniques. The appendixes consist of 1) derivation of the relation between the joint amplitude and splitting time for the joint anisotropy analysis and 2) an application of the joint anisotropy analysis in Southeast Tibatan Plateau.

Receiver function technique has been developed to extract structural response from seismic waves (Clayton and Wiggins, 1976). Based on the structural information carried in receiver functions, the H-k stacking method (Zhu and Kanamori, 2000; Niu et al., 2007) estimates the crustal thickness and average Vp/Vs ratio simultaneously. In the first chapter, I apply receiver function imaging techniques to study the crustal seismic structures in Northeast China region using recently released waveform data from the Chinese Earthquake Administration. I find the crustal thickness in Northeast China varies largely with topography except in eastern flank of

the Songliao Basin and the Changbaishan region. It suggests that dynamic mantle upwelling might have supported the uplifted Moho in this back-arc region.

The seismic anisotropy caused by microstructures and anisotropic minerals is an indicator of deformation processes in the crust. Receiver function has been used to estimate crustal anisotropy (e.g., McNamara and Owens, 1993; McNamara et al., 1994; Iidaka and Niu, 2001; Nagaya et al., 2008); however, the high noise level prevents the single-pair receiver function techniques from robustly estimating azimuthal anisotropy (Liu and Niu, 2012). The accumulated waveform data have provided more power in constraining azimuthal anisotropy in the crust. In the second chapter, I develop a joint approach to estimate azimuthal anisotropy using radial and transverse receiver functions. I use synthetic and real data examples to show that the new technique is robust in estimating anisotropy with presence of noise. We then apply this method to estimate the seismic anisotropy in Southeast Tibetan Plateau and find significant anisotropy in the crust. We observed high Vp/Vs ratios and significant anisotropies with their fast directions subparallel to the topographic gradient directions. It suggests that the Southeast Tibetan Plateau may hava been built by lower crust flow.

Fine crustal velocity structures and impedance boundaries can be imaged using local earthquakes or active sources with a dense seismic array. Full-wave inversion and reverse-time migration are waveform based imaging techniques that have perhaps the best potential in building high-resolution velocity model and imaging impedance boundaries. However, they have not been widely used in imaging crustal structures partly because of the high computational cost of waveform modeling (Failly et al., 1993). Hence, an effective waveform

modeling technique is desirable in facilitating the applications of the full-wave methods in understanding fine crustal structures. In the third chapter, I develop an effective wave extrapolation method to cost-effectively model acoustic waves. The efficiency of this novel waveform modeling technique can reduce the computational cost of full-wave inversion and reverse-time migration significantly.

The three chapters of this thesis are reformatted from three published or submitted work during my thesis research. Chapter 1 is based on a published paper on Earthquake Science (Liu and Niu, 2011). Chapter 2 is based on a published paper on Geophysical Journal International (Liu and Niu, 2012). Chapter 3 is based on a submitted manuscript to Geophysics (Liu et al., 2013). Appendix B is based on a published paper on Earth and Planetary Science Letters (Sun et al, 2012).

Chapter 1*

Receiver function study of the crustal structure of Northeast China: seismic evidence for a mantle upwelling beneath the eastern flank of the Songliao Basin and the Changbaishan region

Abstract

Northeast China is a unique place to study intra-plate volcanism. We analyzed P-wave receiver function data recorded by 111 permanent broadband seismic stations in northeast China. The results show that the crust thickness varies from 27.9 km beneath the eastern flank of the Songliao Basin to 40.7 km beneath the Great Xing'an Range region. The large depth variations of the Moho can be largely but not completely explained by surface topography. The residual Moho depth calculated based on the Airy's isostasy model indicates that the Moho is dynamically uplifted by <3 km beneath the eastern flank of the Songliao Basin and the Changbaishan region. We suggest that a mantle upwelling, which has been proposed by several recent seismic studies, might have caused the uplift.

1.1. Introduction

---

* This chapter is a reformatted version of the article "Receiver function study of the crustal structure of Northeast China: Seismic evidence for a mantle upwelling beneath the eastern flank of the Songliao Basin and the Changbaishan region", Earthquake Science (2011), 24, 27-33, doi:10.1007/s11589-001-0766-6. http://link.springer.com/article/10.1007%2Fs11589-011-0766-6?LI=true. The final publication is available at www.springerlink.com.

The Northeast China region consists of the Northeast China (NE China) Plain with the Songliao Basin in its center, the Central Asian Fold belt, known as the Great Xing'an Range to the west, the uplifted volcanic Changbaishan region to the east and the Sino-Korean Craton to the south. It is located more than 1000 km away from the Japan Trench, where the Pacific plate starts to subduct beneath the Eurasia plate (Figure 1.1). The region is also located roughly above the so-called stagnant slab where the subducted Pacific slab seems to be deflected sub-horizontally around the 660-km discontinuity (Fukao et al., 2001).

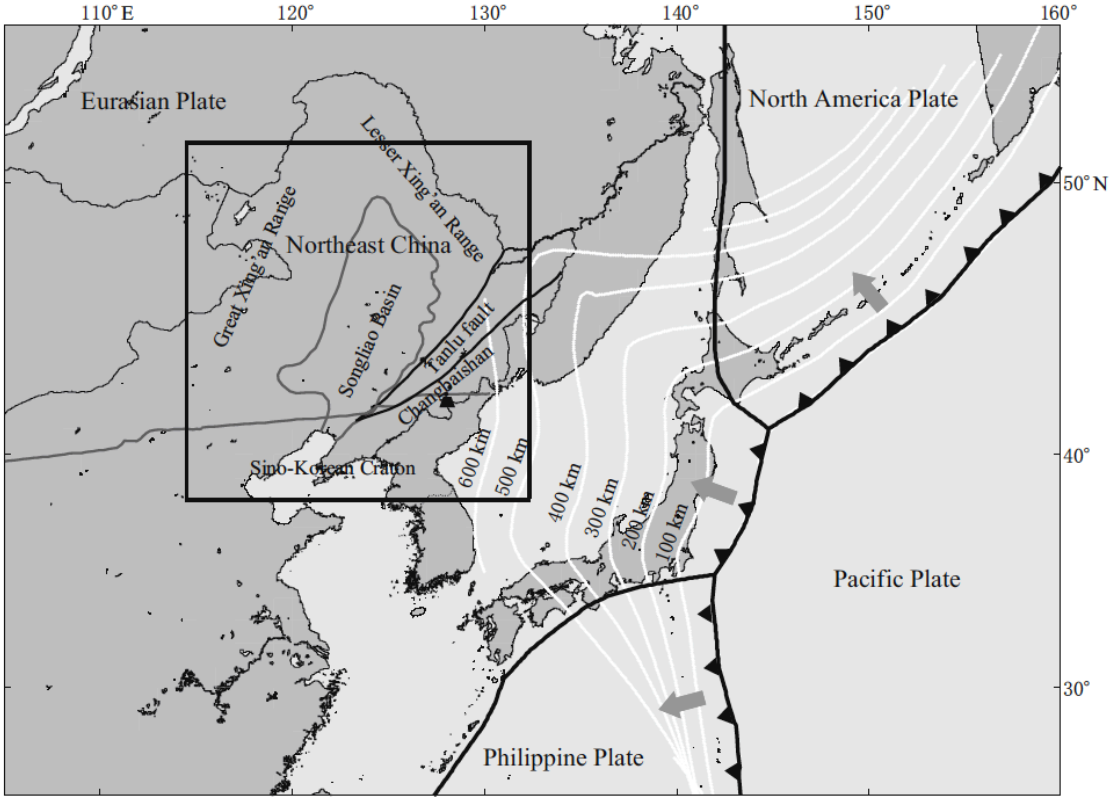

Figure 1.1. Map showing the major tectonic setting of Northeast China and the surrounding area. The subducting Pacific Plate is shown in white lines, which can be traced to 600 km from seismicity.

It is widely believed that the Songliao Basin was a rifting basin and the rifting process took place in the Mesozoic (Hu et al., 1997; Ren et al., 2001) immediately after the closure of the Mongol-Okhotsk Ocean. The collision between the Amurian plate and Siberia blocks after the closure caused lithospheric thickening of the Great Xing'an Range and NE China, and the later collapse of the thickened lithosphere caused convective thinning of the thermal boundary layer. Late Mesozoic volcanic rocks are widely distributed in the region, indicating that active volcanism occurred during the Mesozoic rifting. Volcanism continued in the Cenozoic time in a rather episodic and sporadic manner (Liu et al., 2001). Although it is generally believed that the Cenozoic volcanism in NE China is somehow related to the subduction of the Pacific plate beneath the area (e.g., Liu et al., 2001), one obviously cannot invoke a regular back arc volcanogenic model to explain the Cenozoic volcanism in this region.

One promising model, based on tomographic imaging, is the so-called big-mantle-wedge (BMW) model (Lei and Zhao, 2005; Zhao et al., 2009), which hypothesized a large-scale mantle upwelling in this region as the deep origin of the Cenozoic volcanism. Geochemical studies of volatiles and trace elements suggested that the origin of the Changbaishan volcano is the mantle (Hahm et al. 2008; Kuritani et al., 2009). While there are some geochemical constraints on the presence of an upper mantle upwelling beneath the region (Zou et al., 2008), the depth and lateral distribution remain poorly understood, as does the cause of the upwelling. By combining seismic and electrical conductivity data, Ichiki et al. (2006) proposed two possible mechanisms responsible for the upwelling. Further seismic data are needed to determine which mechanism is more appropriate. Here we investigated the lateral variations of

the crust-mantle boundary with receiver-function data to map out possible deformation at the boundary resulting from the upwelling.

1.2. CEA Regional Networks and Seismic Data

The recent release of broadband waveform data of permanent regional seismic networks in NE China by the China Earthquake Administration (CEA) provided an unprecedented opportunity to investigate the crustal structure of the area (Zheng et al., 2009). There are a total of 128 CEA broadband stations in the study area (115˚-132˚E and 40˚-52˚ N). We collected waveform data from 66 earthquakes with a magnitude Mw≥6.0 occurring between August 2007 and August 2008 recorded at an epicentral distance of 30˚-90˚ (Figure 1.2a). We visually checked all the seismograms and the receiver function data, and selected a total of 2359 receiver functions with a high signal-to-noise ration (SNR) for further analysis. Among the 128 stations, 111 (Figure 1.2b) had enough receiver function data to estimate Moho depth and Vp/Vs ratio.

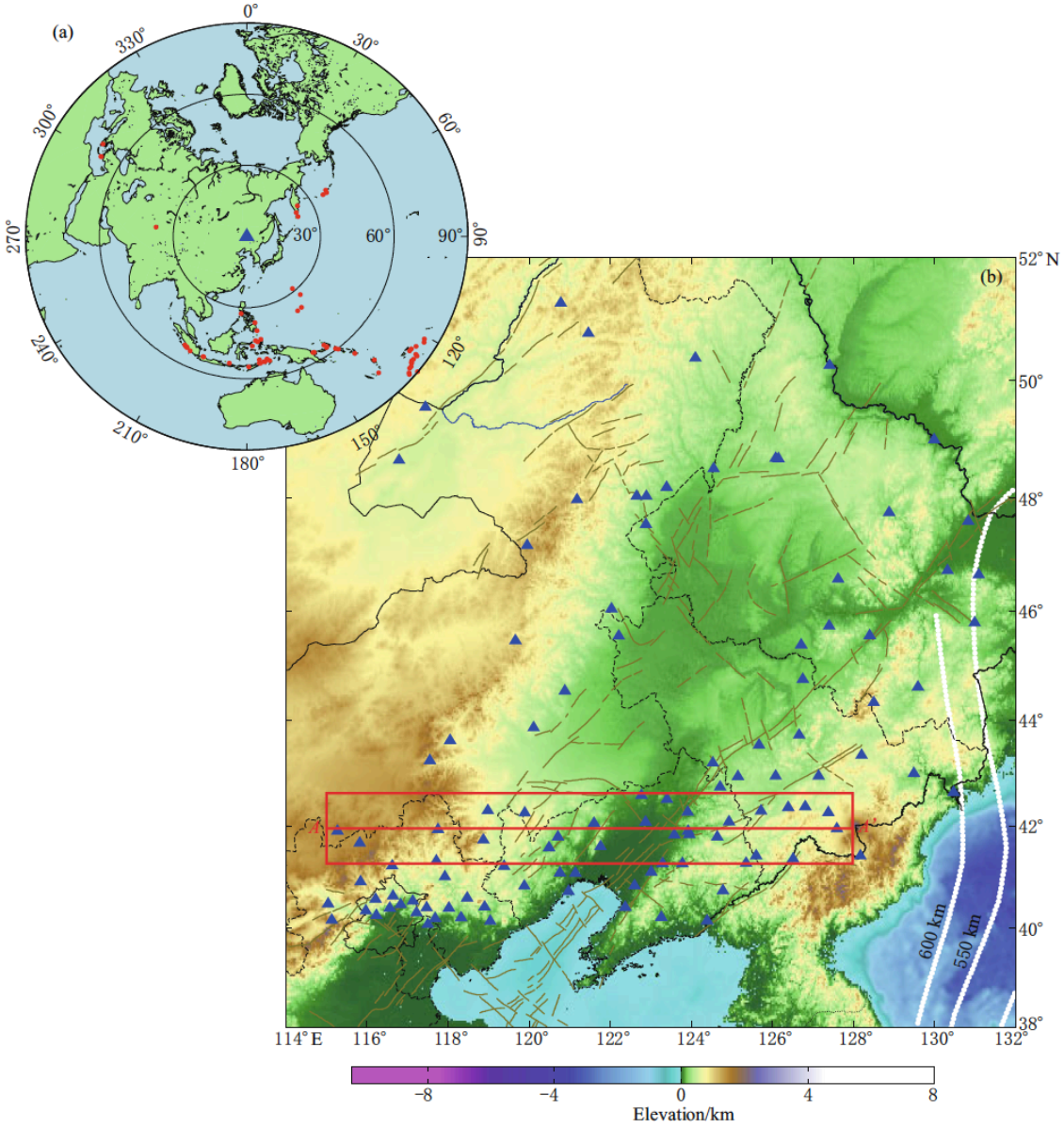

Figure 1.2. a) Locations of the 66 teleseismic events (dots) used in this study. Most of the earthquakes are located in the south Pacific and Indonesia regions. Note that although some of the events fall into the 30° circle to the array center, the data we used have an epicentral distance > 30°. b) Geographic map showing the 111 CEA stations from six regional seismic networks of the China Earthquake Administration. White lines indicate the Pacific subducting

slab and line AA' shows the location of the 2-D CCP image shown in Figure 1.4b. Brown lines indicate faults in the region.

1.3. Receiver Function Analysis

Early receiver function studies used radial and vertical components to form receiver function. In this case, significant P wave energy can be seen in receiver functions, which may interfere with the P-to-S converted phase at the Moho and hence affect the measurements. We thus further rotated the vertical and radial components to the P- and SV-components to avoid the interference and to enhance conversion energy (Niu and Kawakatsu, 1998). We employed the "water-level" deconvolution technique (Clayton and Wiggins, 1976) to generate receiver functions:

$$\mathrm{RF}(\omega)=\frac{\mathrm{V}(\omega)\mathrm{P}^{*}(\omega)}{\max\{\mathrm{P}(\omega)\mathrm{P}^{*}(\omega),\ \mathrm{k}|\mathrm{P}_{\max}(\omega_0)|^2\}}e^{-(\frac{\omega}{2a})^2} \tag{1.1}$$

Here the "water level" parameter k was set to 0.03 to reduce instability of the deconvolution and the Gaussian constant a was set to 1.5 (equivalent to a corner frequency of 0.5 Hz) to suppress higher frequencies. P(ω) and V(ω) are the spectra of the P- and SV-components computed from a 40s time window (5s before and 35s after the first P arrival).

We used a modified H-κ stacking method (Zhu and Kanamori, 2000; Niu et al., 2007) to estimate the Moho depth as well as average Vp/Vs ratio within the crust. Following Niu et al. (2007), we refer to the primary P to S conversion phase as 0p1s, and the two crustal reverberation phases as 1p2s and 2p1s. The numbers before p and s indicate the counts of P- and S-wave legs within the crust, respectively. For each receiver function, we first performed a time

to depth conversion by assuming three different modes: the primary P to S conversion 0p1s model and the reverberation 1p2s and 2p1s modes. The time to depth conversion was performed in the range of 0 to 80 km with an increment of 1 km using the P-wave velocity model based on Pn travel-time data (Sun and Toksöz, 2006) and an assumed Vp/Vs ratio. The ratio was varied from 1.5 to 2.5 with an increment of 0.001. The three depth traces were then summed with different weights. We further used the cross correlations between the three modes as a weight function and summed the three depth traces:

$$\mathrm{A}(d,r) = \frac{c(r)}{w_1 + w_2 + w_3}[w_1 A_{0p1s}(d,r) + w_2 A_{2p1s}(d,r) + w_3 A_{1p2s}(d,r)] \quad (1.2)$$

Where d and r are the Moho depth and Vp/Vs ratio. w_1, w_2, and w_3 are the weights for 0p1s, 2p1s and 1p2s phase respectively and c(r) is the cross correlation weight. Moho depth and Vp/Vs ratio were determined where the summed amplitude reaches its maximum.

For areas with enough station density, we also applied the CCP (common-conversion point) stacking method to image lateral variations of the Moho. To do this, we first ray traced the IASP91 mode (Kennett and Engdahl, 1991) to compute the P-to-S conversion points at different depths for each source-receiver pair. We then gathered receiver functions sharing conversion points along a 2-D cross section.

1.4. Results and Discussion

Crust thickness estimated from the H-κ stacking is shown in Figure 1.3a. Average crust thickness is ~29 km in the Songliao Basin and increases to ~38 km in Great Xing'an Range region. The Moho beneath the Great Xing'an Range region west to the basin is deep, while that

beneath the Changbaishan region east to the basin is a few kilometers shallower. The estimated average crustal Vp/Vs ratio is shown in Figure 1.3b. The Vp/Vs ratio varies between 1.6 and 1.9 and generally agrees with geological features of different blocks in the area. The low Vp/Vs ratio in the Changbaishan region is consistent with a previous seismic study of the region (Hetland, et al., 2004). Measurement errors of crustal thickness and Vp/Vs ratio are estimated to be ~±1 km and ~±0.03, respectively, using spectral analysis (Jenkins and Watts, 1968).

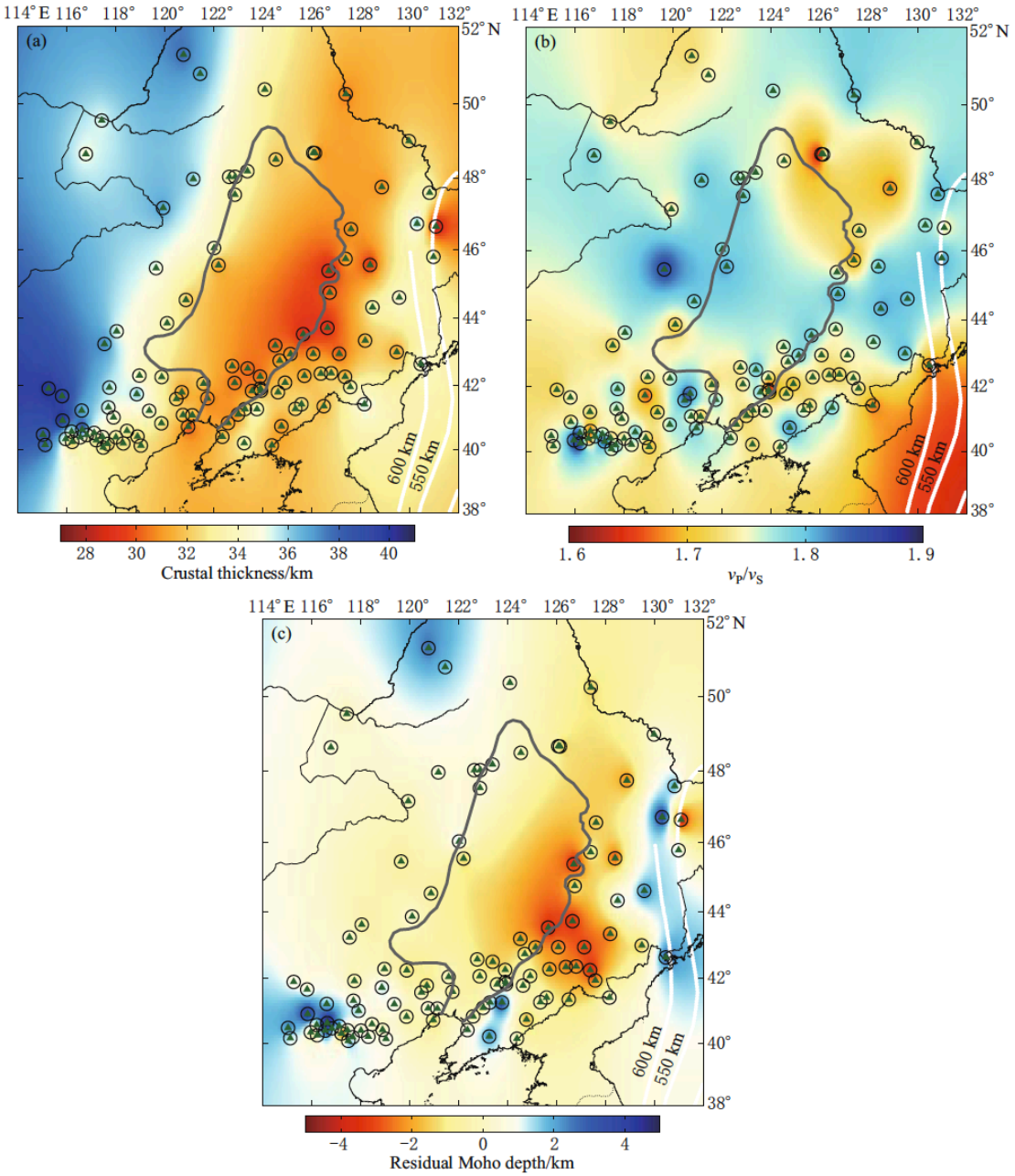

Figure 1.3. a) Moho relief map of the study area. The color contour is based on the observations at stations shown as green triangles. Circles roughly represent area sampled by receiver functions, and the crust thickness can be considered as the average over the circles. b) Map showing the lateral variations of the Vp/Vs ratio. Circles roughly represent area where Vp/Vs

ratio is averaged. c) Map showing the residual Moho depth (see text for detailed calculation). Note a broad uplifted with peak amplitude of 3 km centered in Changbaishan region.

To investigate causes of the depth variation of the Moho, we first calculated the predicted depth variation based on surface topography using the Airy model of isostasy that assumes a laterally uniform density within crust and balances the topographically high mountains with a deeply extend crustal roots. We used a constant density of 2.8×10^3 kg·m^{-3} and 3.3×10^3 kg·m^{-3} for the crust and upper mantle, respectively. We further removed the mean value to show lateral variations at Moho depth. The main feature shown in the residual Moho depth map is a broad negative anomaly along the eastern flank of the Songliao Basin and the Changbaishan region (Figure 1.3c). The negative anomaly has a ~3 km peak amplitude centered roughly at the Changbaishan volcano and extends ~300 km and ~400 km in the EW and NS directions, respectively.

To further illustrate the significant difference observed at Moho depth between the western and eastern edge of the Songliao Basin, we made a 2D CCP image along an EW line at 42°N (Figure 1.2b), where we have high enough station density. The CCP stacked image (Figure 1.4b) shows a clear Moho, which is ~40 km in the west, ~30 km beneath the southern margin of the Songliao Basin, and ~33 km in the east. The deep-shallow-intermediate Moho pattern generally corresponds to the high-low-intermediate pattern of average topography (Figure 1.4a). However, a careful comparison between the two indicates that the eastern side of the basin has a significantly shallower root than the western one although both rise to a roughly similar altitude (from 0.4 km to 1.2 km).

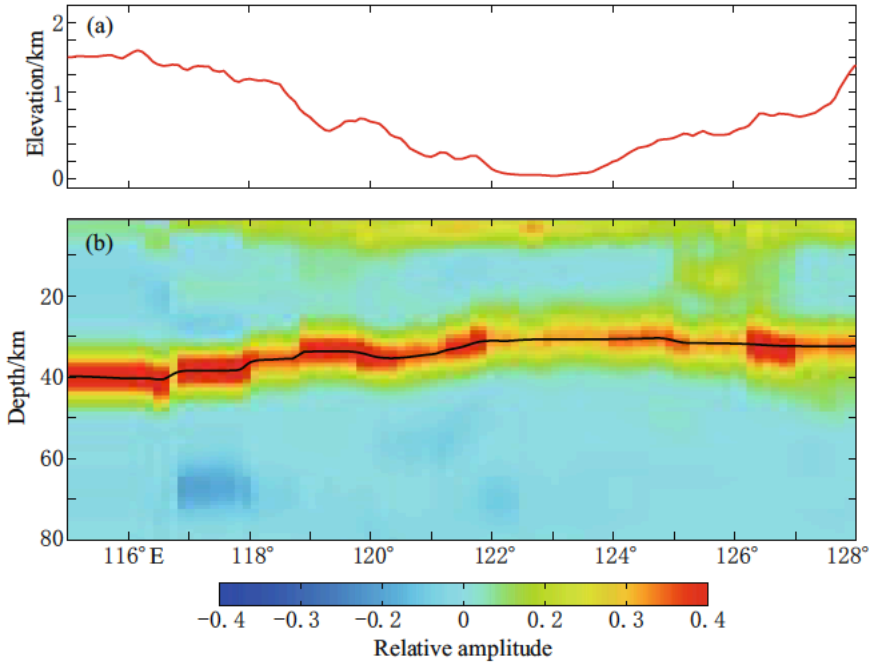

Figure 1.4. Elevation a) and CCP image b) along line AA' at 42˚N shown in Figure 1.3. P to S converted energy is indicated by colors; hotter colors represent greater energy. Note that the Moho is clearly imaged (black line). No significant deepening of Moho was observed beneath the Changbaishan region located at the eastern end of the profile.

A negative anomaly corresponds to a relatively shallower Moho compared to the Airy's static prediction. Since this anomaly roughly coincides with the region with a low velocity in the upper mantle, we assume that the uplift seen here reflects the dynamic deformation related to the low velocity anomaly (Lei and Zhao, 2005; Zhao et al., 2009). Lei and Zhao (2005) attributed the low velocity anomaly to dehydration from the sub-horizontally deflected slab. On the other hand, the lateral resolution of the tomographic images is of either local or global scale. Thus it is hard to identify a vertically consistent anomaly from these images. The Moho uplifted region is located ~200-500 km western of the 600 km contour of the observed deep seismicity

in the area (Figure 1.3c). We thus speculated that this broad uplift is somehow associated with the presence of deep subduction in this region.

While both thermal and compositional buoyancy have been proposed to be the driving force of the upwelling (Ichiki et al., 2006), here we assume the observed deformation at the Moho has a thermal origin. The thermal buoyancy force, ΔF_b, due to a temperature anomaly, ΔT, supports the mass contrast, ΔW, between mantle and crustal material filled within the uplift Moho space (Figure 1.5):

$$(\rho'_M - \rho_M)gh = (\rho_M - \rho_C)g\Delta h \tag{1.3}$$

Here ρ_C and ρ_M are the average densities of the crust and the upper mantle, respectively. H and Δh are the height of the temperature anomaly body and the amount of uplift of the crust-mantle boundary, respectively. ρ'_M is the mantle density with an elevated temperature (ΔT), which can be calculated from the thermal expansion coefficient, a:

$$\frac{\rho'_M - \rho_M}{\rho_M} = -\alpha\Delta T \tag{1.4}$$

From (1.3) and (1.4), we obtain:

$$\Delta T \cdot h = \frac{\Delta\rho\Delta h}{\alpha\rho_M} \tag{1.5}$$

Taking typical values of density and the thermal expansion coefficient of the crust and the mantle: $\rho_C=2.8\times10^3$ (kg·m^{-3}), $\rho_M=3.3\times10^3$ (kg·m^{-3}) and $\alpha=3\times10^{-5}$ (K^{-1}), a Δh of 3km would result in a $\Delta T\cdot h=1.5\times10^7$ (m·K). If we assume $\Delta T=150$ K, as suggested by Ichiki et al. (2006), the depth extension of the thermal upwelling is estimated to be ~100 km, which is consistent with the estimate of Ichiki et al. (2006).

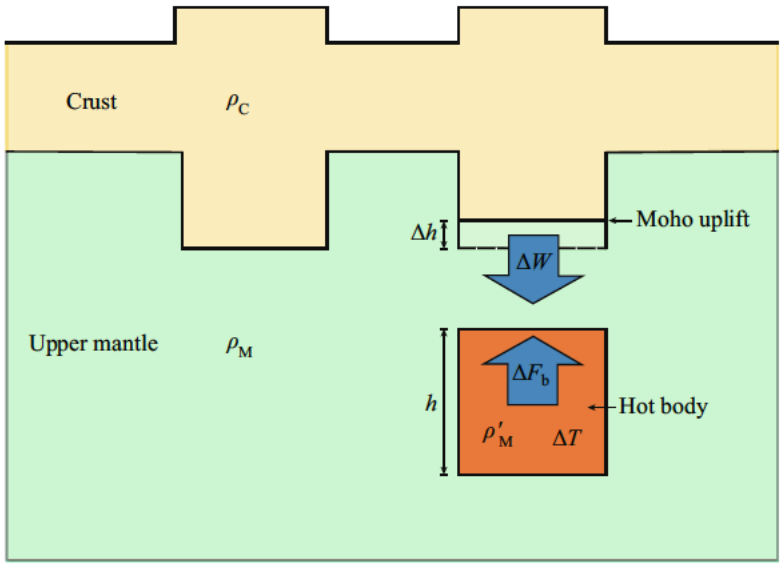

Figure 1.5. A schematic model showing the balance between the buoyancy (ΔF_b) caused by a hot upwelling shown in orange and the extra mass (ΔW) due to a reduced crustal root.

In Figure 1.6, we show a 3-D perspective view of the broad uplift observed at the Moho and surface topography. We also show a schematic upwelling at around ~150 km with a depth extension of 100 km. Further detailed modeling is required to constrain the lateral scale as well as the absolute depth of the anomaly.

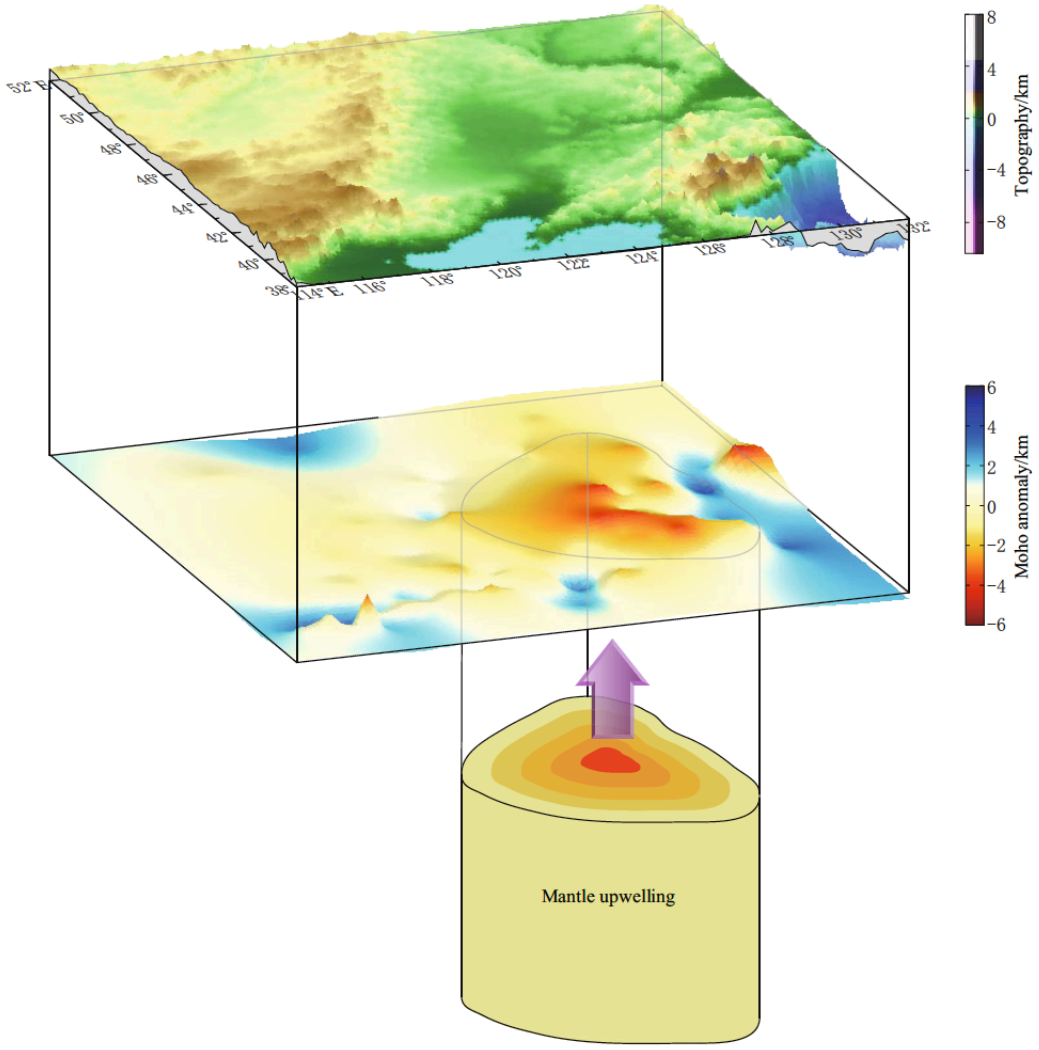

Figure 1.6. Map showing a 3D perspective view of the broad Moho uplift and the topography relief of the study area. A mantle upwelling is schematically shown beneath the Changbaishan area to indicate the dynamic origin of the observed deformation of the Moho.

1.5. Conclusions

We investigated crustal structure in the Northeast China region using receiver function data recorded by several regional seismic networks in the region. We found: (1) the Songliao Basin

has a relatively thin crust, probably resulting from rifting that occurred in the Mesozoic; (2) high topography of the Great Xing'an Range located at the western boundary of the basin is almost isostatically balanced by a thick crustal root; (3) The eastern margin of the Songliao Basin, where active Cenozoic volcanism occurred, is underlain by a relative thin crust, despite the relatively high topography in these regions, consistent with the presence of a mantle upwelling proposed by previous studies. Our observations suggested that variations in crustal thickness seem to play an important role in determining tectonic activity in the study region.

Chapter 2*

Estimating crustal seismic anisotropy with a joint analysis of radial and transverse receiver function data

Abstract

We developed an integrated technique for estimating crustal anisotropy with a horizontal axis using radial and transverse receiver functions. The technique includes computing three individual and one joint objective function, and a reliability analysis of the estimated anisotropy. The individual objective functions (IOFs) are designed to: 1) maximize the peak energy of the stacked R receiver function after a cosine moveout correction in the Ps arrival time; or 2) to maximize the correlation of the radial receiver functions after a full correction of anisotropy; or 3) to minimize the total energy of transverse receiver functions stacked after a removal of crustal anisotropy. The joint objective function (JOF) was computed by a weighted average of the three IOFs, while the reliability analysis utilizes the principle that stacking coherent signals can lead to an increase of signal to noise ratio. We applied the technique to synthetic receiver functions generated with 30-60% white noise from a variety of anisotropic and heterogeneous models. The synthetic tests indicate that the proposed technique has good capability to recover the input models. Despite the presence of random and other coherent noises, such as those caused by inhomogeneous structures, in the data, the technique can always

---

* This chapter is a reformatted version of the article "Estimating crustal anisotropy with a joint analysis of radial and transverse receiver function data", Geophysical Journal International (2012), 188, 144-164, doi:10.1111/j.1365-246X.2011.05249.x http://gji.oxfordjournals.org/content/188/1/144.full.pdf+html. The final publication is available at www.blackwell-synergy.com.

provide accurate estimates of crustal anisotropy. We applied the technique to two permanent seismic stations in western China, and found significant crustal anisotropy beneath one station located at the northern edge of the Tibetan plateau. The observed fast polarization direction at this station follows the direction of the maximum horizontal tensile stress, suggesting that the observed seismic anisotropy is likely caused by mineral alignment in the lower crust. The station situated in the Sichuan basin, on the other hand, shows little to no seismic anisotropy, which may suggest that the crust beneath the basin is nearly rigid with very little deformation. The developed technique can be applied to any broadband seismic stations that have a good back azimuthal coverage of teleseismic events.

2.1. Introduction

Numerous seismic observations have shown that the earth's upper crust and upper mantle exhibit anisotropy for seismic wave propagation (e.g., Crampin and Lovell, 1991; Silver, 1996). It is generally believed that seismic anisotropy observed in the upper crust is caused by stress-induced alignment of cracks. As the vertical stress increase steadily with depth, the minimum stress direction starts to lie in a horizontal direction below a critical depth of 0.5-1 km (Crampin, 1990). Such a stress field leads to the development of vertical cracks and azimuthal anisotropy. On the other hand, seismic anisotropy observed in the upper mantle is generally believed to be caused by preferentially orientation of the highly anisotropic upper mantle mineral, olivine, through mantle deformation (e.g., Nicolas and Christensen, 1987). The close relationship between the stress/strain field and seismic anisotropy thus can be used to map deformation associated with a wide range of tectonic processes.

Seismic anisotropy is often measured with two parameters, the fast polarization direction φ and delay time δt between the fast and slow directions, from splitting or birefringence of shear waves, such as the S, ScS and SKS phases, recorded at either local or teleseismic distances (e.g., Crampin, 1987; Silver and Chan, 1991). Kaneshima (1990) measured φ and δt using direct S waves recorded at ~40 seismic stations across Japan from local earthquakes with a focal depth ranging from 1.5 km to 100 km. The fast polarization direction φ measured at most of the stations aligns well with the direction of the maximum horizontal compressional stress. The observed δt varies between 0.03 and 0.2 s, and appears to increase with focal depth for earthquakes occurring shallower than 15 km. The correlation was not seen from events with a deeper focus, including those occurring in the mantle. The result suggests that the source region producing the observed splits is most likely located in the upper 15 km of the crust, and seismic anisotropy in the lower crust is relatively weak. However, if seismic anisotropy changes with depth and if local earthquakes are restricted to certain back azimuths, the local S-wave data could have very limited resolution of anisotropy in the lower crust, as the measured φ and δt could, in principle, reflect only the seismic anisotropy of the last traveled path, which is the upper crust.

Seismic anisotropy in the mantle is usually measured with the teleseismic SKS wave, a radially polarized phase at the core-mantle boundary (CMB) right after the P to S conversion. The observed seismic anisotropy could, in principle, be located anywhere along the S-wave ray path from the CMB to the surface at the receiver side. While the dominant contribution to the splitting can be attributed to the upper mantle above the transition zone, as splitting parameters measured from different types of shear waves recorded at a seismic station appear to be

consistent with each other (Silver and Chan, 1991; Meade et al., 1995; Niu and Perez, 2004), it is always difficult to pinpoint the exact depth range within the upper mantle for the observed anisotropy (Silver, 1996). Comparison with patterns of lithospheric deformation and asthenospheric flow are usually used to argue for the possible source region of the observed seismic anisotropy. For example, Masy et al. (2011) attributed the large splitting times observed at the Caribbean-South American plate boundary to a mantle flow induced by slab tears and the moderate splitting times from the Merida Andes to vertical coherent deformation in the lithosphere. Another ambiguity in interpreting SKS splitting is the crustal contribution. Although many studies indicate that splitting times due to upper crustal anisotropy is less than 0.2 s, as mentioned above, contributions from the lower crust is still unclear. This is particularly true in regions where lower crustal flow may be present, like in the eastern margin of Tibetan plateau (Clark and Royden, 2000).

McNamara and Owens (1993) found clear evidence of waveform splitting of the Moho Ps converted phase recorded at seismic stations in the Basin and Range province in US. They applied several shear-wave splitting analysis techniques developed for SKS/SKKS measurements (e.g., Bowman and Ando, 1987; Silver and Chan, 1991) to the Moho Ps conversion data and obtained a delay time of ~0.2 s. They found that the fast polarization directions at all the stations are either parallel or subparallel to the direction of maximum horizontal tensile stress. This is inconsistent with the upper crustal anisotropy mechanism discussed above; rather it suggests that preferred alignment of anisotropic minerals, which is used in interpreting mantle anisotropy, is the likely mechanism here. Nagaya et al. (2008) also applied the splitting measurement techniques to receiver function data recorded in the Chugoku

region of southwestern Japan. The fast polarization directions obtained from the Moho Ps conversion phase appeared to be also in the direction of maximum horizontal tensile stress, and normal to those from local earthquake measurements obtained by Kaneshima (1990). The observed splitting time ranges from 0.2 to 0.7 s, which should be no longer negligible in interpreting SKS splitting data. A robust estimate of crustal seismic anisotropy thus is not only critical in understanding crustal deformation, but also of great importance in deciphering dynamic processes at various depths in the upper mantle.

In general, the Moho Ps converted wave is a much weaker signal compared to the SKS/SKKS phase. As shown later, the techniques designed for extracting splitting parameters from individual SKS/SKKS waveform data could introduce significant measurement errors and may not be appropriate to receiver function data. To obtain robust estimates of seismic anisotropy from receiver function data, synthetic receiver function data from anisotropy velocity models have been computed for comparison (Levin and Park, 1997; Peng and Humphreys, 1997, Savage, 1998; Frederiksen and Bostock, 2000). Synthetic receiver functions show a clear $\cos 2\varphi$ variation in the peak Ps arrival time on the radial (R) receiver functions (Figure 2.1a) and in the polarity of the Ps waveform on the transverse (T) receiver functions (Figure 2.1b) in the presence of crustal anisotropy with a horizontal axis. These features have been used to identify crustal anisotropy and extract splitting parameters from receiver function data. Levin et al. (2008) employed a forward modeling approach to match directional gathers of receiver functions with synthetics computed from anisotropic models. To better constrain the models, they first used the polarity change observed in the transverse component to define the fast direction.

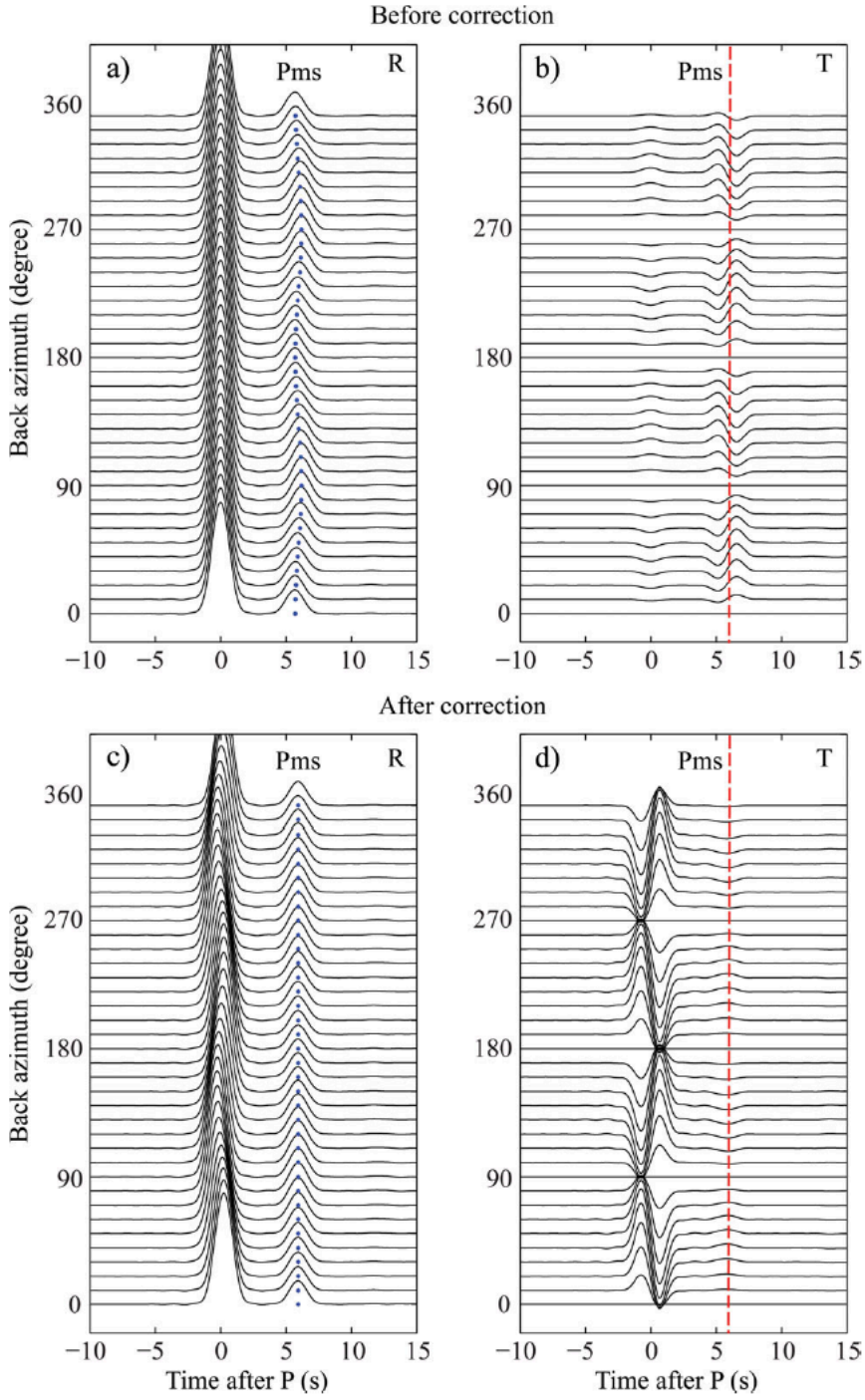

Figure 2.1. Synthetic receiver functions computed from a one-layered anisotropy model (M1 in Table 2.1) are plotted as a function of back azimuth. The T receiver functions shown in (b) and (d) are magnified by a factor of 2. The R and T components before correction of anisotropy are

shown in (a) and (b), respectively. Dots in (a) indicate the arrival time of the peak amplitude of the Moho Ps converted phase. Note its cosine variation along the back-azimuthal direction. Dashed line in (b) indicates the Ps arrival time. Note that the polarity of the Ps phase changes periodically with a period of 180°. The R and T receiver functions after the removals of anisotropy are shown in (c) and (d), respectively. Again, dots in (c) indicate the peak of the Moho Ps wave. Note the excellent alignment of the Ps after the correction. The dashed line in (d) also indicates the Ps arrival time, around where little to no energy is remained after the removal of seismic anisotropy.

Model		H(km)	α(km s^{-1})	β(kms^{-1})	ρ(gcm^{-3})	Fast direction	S-wave anisotropy	Strike	Dipping
#	Description								
M1	1-layer flat_aniso.	50.0	6.50	3.75	2.9	0°	4%	-	-
M2	1-layer flat_iso.	50.0	6.50	3.75	2.9	-	-	-	-
M3	1-layer dip_iso	50.0	6.50	3.75	2.9	-	-	0°	10°
M4	1-layer het._iso	50.0	6.50	3.60 3.75	2.9	-	-	-	-
M5	2-layer flat_aniso.	20.0	5.80	3.36	2.7	60°	2%	-	-
		30.0	6.50	3.75	2.9	0°	4%	-	-
M6	1-layer flat_iso.	50.0	6.50	3.75	2.9	-	-	-	-
	aniso. mantle	50.0	8.04	4.50	3.3	0°	4%	-	-

Table 2.1: Crust models used for synthetic tests

In this study, we developed a splitting measurement technique specifically for receiver function data. It utilizes the features that are uniquely possessed by anisotropic models observed on the synthetic receiver function data (Figure 2.1). As mentioned before, the Moho Ps conversion usually has low signal-to-noise ratio (SNR) in individual receiver function data. We thus decided to solve one pair of φ and δt that best explain all the receiver functions recorded at a single station, instead of using the approach employed by the previous studies (McNamara and Owens, 1993; McNamara et al., 1994 Nagaya et al., 2008), which measures individual (φ, δt) sequentially from receiver functions and selects the most frequent occurring pair as the station

estimate. We further verify our estimates with a statistical analysis based on SNR improvement of the Ps arrival as a signal/noise on the radial/transverse component after the estimated seismic anisotropy being corrected. We conducted extensive tests with synthetic receiver functions and found that the technique was able to recover the input anisotropy in the presence of high level of noise in the data and certain complexities in crustal structure, such as a dipping crust-mantle boundary and azimuthal variations in velocity structure. We further applied this technique to two permanent stations in western China and found that our measurements are consistent with previous studies, suggesting that the method could be used to systematically map crustal anisotropy at regional or global scale.

2.2. Method

2.2.1. Receiver function generation and moveout corrections

We used the "water-level" deconvolution technique to generate R and T receiver functions (Clayton and Wiggins, 1976; Ammon, 1991), a modified division in the frequency domain:

$$F_r(\omega) = R(\omega)Z^*(\omega)e^{-(\frac{\omega}{2a})^2} \Big/ \max\{Z(\omega)Z^*(\omega), k\,|\,Z_{max}(\omega_0)|^2\}$$
$$F_t(\omega) = T(\omega)Z^*(\omega)e^{-(\frac{w}{2a})^2} \Big/ \max\{Z(\omega)Z^*(\omega), k\,|\,Z_{max}(\omega_0)|^2\} \quad (2.1)$$

Here k and a are two constants that define the "water level" and the corner frequency of the Gaussian low pass filter, respectively. k was set to be 0.01 and a was set to be 4.0, which is equivalent to a corner frequency of ~1 Hz. Z(w) and R(w) are the spectra of the radial and transverse components of the seismic recordings, and $Z^*(w)$ is the complex conjugate of Z(w). Once they were generated, we normalized the R and T receiver functions by a division of the total energy computed from the two components in the time window between -10 and 40 s.

Since the Moho Ps conversion phase has a slightly smaller ray parameter than the direct P wave does, the relative arrival time of the Ps phase with respect to the P wave has a negative moveout. We used a revised IASP91 model (Kennett and Engdahl, 1991) with a modified crust to compute this moveout and made corrections so that all the Ps phases have a relative arrival time equivalent to the epicentral distance of 60° with a source depth of 0 km. After normalization and moveout correction, the R and T receiver functions were plotted as a function of back azimuth to show whether there are systematic variations in the peak Ps arrival time and polarity changes in the R and T receiver functions, respectively.

2.2.2. Estimating shear wave splitting with individual receiver function

Most previous crustal anisotropy studies with receiver function data (e.g., McNamara and Owens, 1993; McNamara et al., 1994; Iidaka and Niu, 2001; Nagaya et al., 2008) employed more or less the same techniques developed for SKS splitting analysis (e.g., Bowman and Ando, 1987; Silver and Chan, 1991). The analysis involves a grid search of φ and δt, and can be divided roughly into four major steps: 1) projecting each receiver function pair ($F_r(t)$ and $F_t(t)$) to the assumed fast and slow polarization directions $F_f(t, \varphi)$ and $F_s(t, \varphi)$;

$$\begin{aligned} F_f(t,\varphi) &= F_r(t)\cdot\cos(\varphi-\theta) + F_t(t)\cdot\sin(\varphi-\theta) \\ F_s(t,\varphi) &= -F_r(t)\cdot\sin(\varphi-\theta) + F_t(t)\cdot\cos(\varphi-\theta) \end{aligned}, \qquad (2.2)$$

where θ is the back azimuth of the individual receiver function; 2) time shifting the fast component ($F_f(t, \varphi)$) forward, and the slow component ($F_s(t, \varphi)$) backward by half of the assumed splitting time (δt) to form the corrected fast and slow components ($F_f^c(t, \varphi, \delta t)$ and $F_s^c(t, \varphi, \delta t)$):

$$F_f^c(t,\varphi,\delta t) = F_f(t+\delta t/2,\varphi)$$
$$F_s^c(t,\varphi,\delta t) = F_s(t-\delta t/2,\varphi) \quad (2.3)$$

; 3) projecting the time-corrected receiver-function pair ($F_f^c(\varphi,\delta t,t)$ and $F_s^c(\varphi,\delta t,t)$) back to the R and T directions ($F_r^c(\varphi,\delta t,t)$ and $F_t^c(\varphi,\delta t,t)$, Figures 2.1c and 2.1d):

$$F_r^c(t,\varphi,\delta t) = F_f^c(t,\varphi,\delta t)\cdot\cos(\varphi-\theta) - F_s^c(t,\varphi,\delta t)\cdot\sin(\varphi-\theta)$$
$$F_t^c(t,\varphi,\delta t) = F_f^c(t,\varphi,\delta t)\cdot\sin(\varphi-\theta) + F_s^c(t,\varphi,\delta t)\cdot\cos(\varphi-\theta) \quad (2.4)$$

; 4) searching for a pair of ($\varphi,\delta t$) that either minimizes the T component energy or maximizes the cross-correlation ($c(\varphi,\delta t)$) between the time-corrected fast and slow components:

$$c(\varphi,\delta t) = \int_{t_b}^{t_e} F_f^c(t,\varphi,\delta t)\cdot F_s^c(t,\varphi,\delta t)\,dt \quad (2.5)$$

here $[t_b,t_e]$ defines the arrival time window of the Moho Ps converted phase.

The above procedure is usually applied to each receiver function pair which yields multiple estimates of ($\varphi,\delta t$) at each seismic station. The most frequently observed φ is usually taken as the measurement at the station and the delay time is computed from the average of the δt estimates (Nagaya et al., 2008). We have applied this single-event based method to several synthetic datasets, and found that it provides reliable splitting estimates only when noise level in the data is low (Figure 2.2a). Even a small amount of noise (30%) could bias the estimate of fast polarization direction by as much as 30° (Figure 2.2b). Moreover, at high noise level, the measured fast directions are highly scattered and appear to be insensitive to the input model (Figure 2.2c, d).

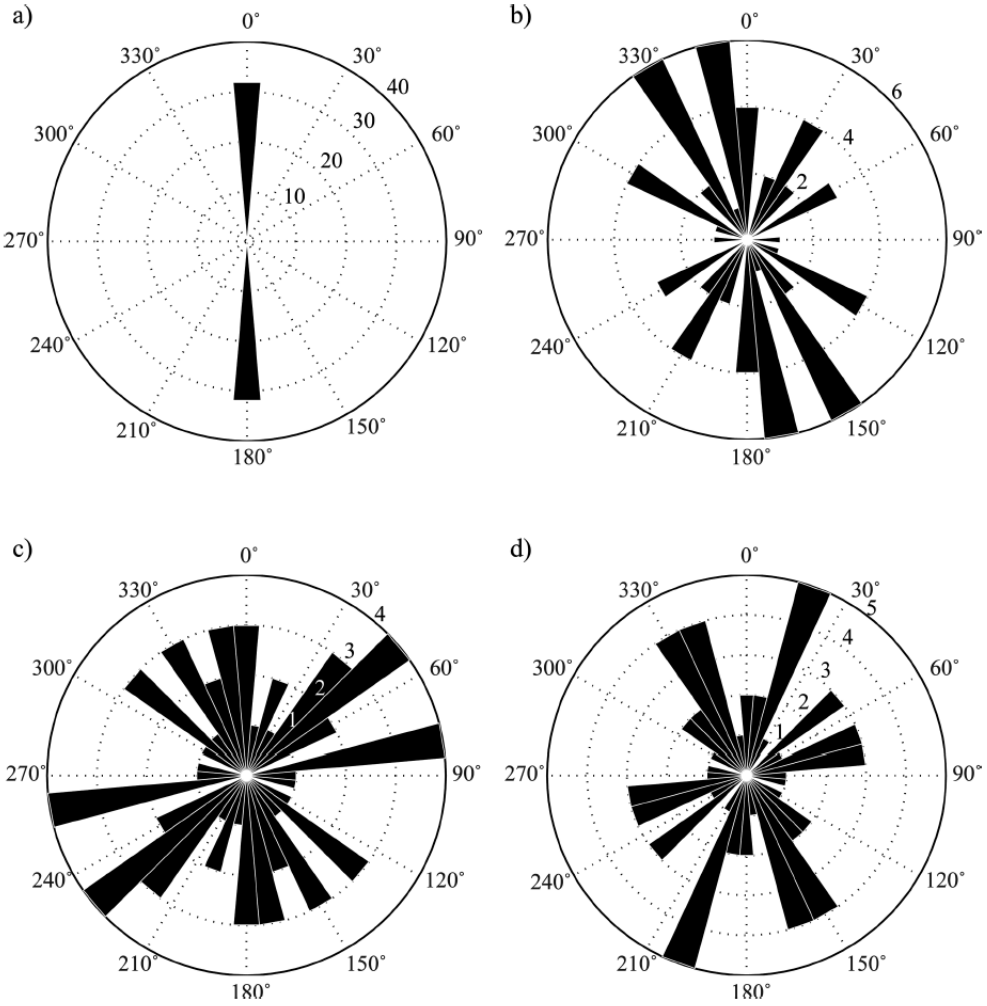

Figure 2.2. Rose diagrams showing fast polarization directions estimated from individual synthetic receiver functions computed with the anisotropic model M1 and noise levels of 0% a), 30% (b) and 60% (c). We used a 10° bin in plotting the measurements. Numbers near the circular grid indicate the total numbers of measurement within a particular bin. Note the significant difference in the estimates of the fast direction when noise is present in the data (b and c). The estimated fast directions are spread in the full back-azimuthal range when the noise level is high (c). We also calculated synthetic receiver functions using a one-layer isotropic

model (M2 in Table 2.1) and included 30% white noise. The estimated apparent fast direction is shown in (d), which also exhibits substantial variations.

2.2.3. Imaging shear wave splitting with a joint analysis of receiver function gathers

As shown above, in the presence of noise, measuring splitting parameters from individual receiver function data could introduce large errors. We chose to solve for one pair of (φ,δt) that fits all the receiver functions collected at a station. We further combined the results from three different methods to seek a robust estimate of crustal anisotropy with receiver function data.

2.2.3.1. Radial energy maximization with cosine moveout correction.

Figure 2.1a shows a four-lobed variation in the peak Ps arrival time, which can be evaluated by a cosine function. The fast direction and delay time can be estimated from the phase and amplitude of the cosine function. Our first means of estimating (φ, δt) is thus based on the ratio of peak energy computed by stacking all the R receiver functions after and before the time correction of the cosine moveout:

$$I_{r\cos}(\varphi,\delta t)=\left\{\sum_{j=1}^{N}F_r^j(t-\frac{\delta t}{2}\cdot\cos 2(\varphi-\theta_j))\right\}_{\max}^{2}\Bigg/\left\{\sum_{j=1}^{N}F_r^j(t)\right\}_{\max}^{2},\qquad t\in[t_b,t_e] \tag{2.6}$$

The superscript j here represents the j-th receiver function with a back azimuth θ_j. N is the total number of receiver functions. The subscript max indicates the largest amplitude within the Ps arrival time window defined by $[t_b,t_e]$. An example of the peak energy ratio as a function of (φ, δt) is shown in Figure 2.3a. We varied φ in the range of 0° to 360° with an increment of 1°, and δt from 0.0 to 1.5 s in increments of 0.02 s. The ratio reaches its maximum at the input anisotropic parameters (φ=0°, δt=0.5s) (Figure 2.3a).

2.2.3.2. Radial cc maximization.

We further used the cross correlation of the R receiver functions to estimate the splitting parameters φ and δt. This is done first by following the equations 2.2-2.4 to compute the anisotropy-removed R and T receiver functions. The summed cross correlation coefficient (cc), normalized by its original value,

$$I_{rcc}(\varphi,\delta t) = \int_{t_b}^{t_e}\left\{\left[\sum_{j=1}^{N} F_{r,j}^{c}(\varphi,\delta t,t)\right]^2 - \sum_{j=1}^{N}\left[F_{r,j}^{c}(\varphi,\delta t,t)\right]^2\right\}dt \Big/ \int_{t_b}^{t_e}\left\{\left[\sum_{j=1}^{N} F_{r,j}(t)\right]^2 - \sum_{j=1}^{N}\left[F_{r,j}(t)\right]^2\right\}dt \qquad (2.7)$$

is used in evaluating the best fit for the crustal anisotropy. With synthetic receiver function data, this approach also recovered the input splitting parameters (φ=0°, δt=0.5s) (Figure 2.3b).

2.2.3.3. Transverse energy minimization.

This is an implementation of Silver and Chan (1991) applied to data from multiple events (Wolfe and Silver, 1998; Li and Niu, 2010; Masy et al., 2011). Normally, the Moho Ps converted phase is radially polarized; therefore, the presence of T energy is indicative for inhomogeneous structure in the crust. For an assumed pair of (φ, δt), we first followed the equations 2.2-2.4 to compute the T energy after the time correction, and then used its ratio with the original T energy to estimate the crustal anisotropy:

$$I_t(\varphi,\delta t) = \sum_{j=1}^{N}\int_{t_b}^{t_e}\left[F_{t,j}^{c}(\varphi,\delta t,t)\right]^2 dt \Big/ \sum_{j=1}^{N}\int_{t_b}^{t_e}\left[F_{t,j}(t)\right]^2 dt \qquad (2.8)$$

Here the subscript j and superscript c indicate the j-th receiver function after time correction. N is the total number of receiver functions, and the Ps arrival time window is defined by $[t_b,t_e]$. As shown in Figure 2.3c, the method recovers the anisotropy (φ=0°, δt=0.5s) used for computing synthetic receiver functions.

2.2.3.4. Joint solution.

The above three methods utilize different characteristics of crustal anisotropy on receiver function data. In principle, they are expected to yield more or less the same estimate (Figures 2.3a-2.3c). However, they could give slightly different or even inconsistent estimates when noise and other inhomogeneous structure are present. In order to make the full usage of the fingerprint of anisotropy on receiver functions, we combined the three objective functions into a joint objective function (JOF):

$$\mathrm{I}(\varphi,\delta t) = \frac{\left[I_{r\cos}(\varphi,\delta t)\right]^{w1}\left[I_{rcc}(\varphi,\delta t)\right]^{w2}}{\left[I_{t}(\varphi,\delta t)\right]^{w3}}, \tag{2.9a}$$

which can be rewritten as:

$$\ln \mathrm{I}(\varphi,\delta t) = w_1 \ln I_{r\cos}(\varphi,\delta t) + w_2 \ln I_{rcc}(\varphi,\delta t) - w_3 \ln I_{t}(\varphi,\delta t)\,. \tag{2.9b}$$

Here w1, w2 and w3 are the relative weights among the three measurements, which can be determined based on the relative confidence level of the three measurements. We have set them to one in this study for simplicity. An example of the JOF is shown in Figure 2.3d, which exhibits a maximum at the input fast direction and delay time (φ=0°, δt=0.5s), as each individual measurement does. Based on equation 2.3, the corrected fast and slow components do not change when δt=0s. Consequently there are no changes in the corrected R and T receiver functions, and the ratios defined in the equations 2.6-2.8 have a unit value. The JOF thus has a unit value at δt=0s, and is expected to have a maximum amplitude greater than one once anisotropy induced waveform splitting is corrected. It can be shown that the significance of maximums (the difference between maximums and unit value) of the three IOFs and the subsequent JOF are approximately proportional to δt^2 (see Appendix A). The maximum

amplitude of the JOF, thus, is an important indicator of crustal anisotropy imprinted on receiver function data.

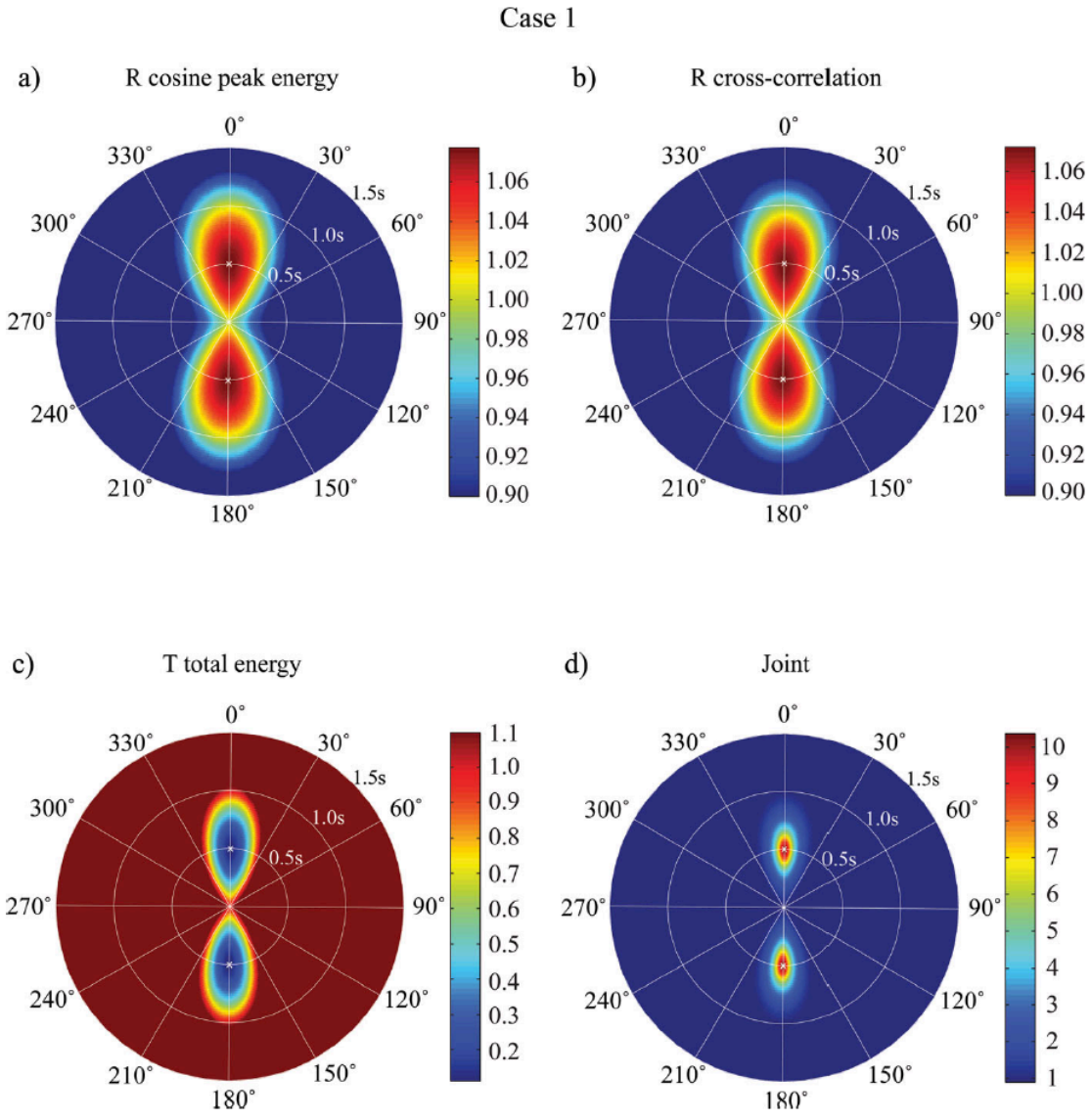

Figure 2.3. Results from test case 1. The three IOFs defined by the equations 2.6, 2.7, and 2.8 are shown in (a), (b) and (c), respectively. Synthetic receiver functions were calculated using the anisotropic model, M1 (Table 2.1), with 0% noise. The objective functions were computed in a 2D plane of (φ, δt) in the range of (0°-360°, 0.0-1.5s) with an increment of (1°, 0.02s). (a), (b)

and (c) correspond to three different ways for estimating seismic anisotropy: (1) R energy maximization with cosine moveout correction; (2) Radial cc maximization; and (c) T energy minimization. Color scales showing variations of the objective functions are plotted right to the functions. The JOF is shown in (d). The input fast polarization direction and the splitting time are marked by a white "x".

2.2.3.5. SNR test (SNRT).

We further designed a statistical analysis to evaluate whether the estimated anisotropy is a robust feature of data or not. The analysis is based on an algorithm for signal/noise diagnosis. The anisotropy-corrected R receiver functions are expected to record a coherent Ps converted signal, while the T receiver functions should consist mainly of random noise after the removal of anisotropy. For a coherent signal, a classical way to enhance SNR is stacking, which can improve the SNR by a factor of $N^{1/2}$ when the noise among traces is uncorrelated. We used this criterion to diagnose whether the data in certain time window consists mainly of coherent signals or random noise. We first randomly selected a sub-sample of N receiver functions from a total of M receiver functions gathered at a seismic station. These receiver functions were stacked linearly and the SNR was calculated from the stacked receiver function. We repeated this procedure for a total of m times (here m=100) and took the geometric mean of the m measurements of SNR:

$$\sigma_N = \prod_{k=1}^{m} \left\{ \int_{signal} \left[\sum_{j=1}^{N} F_j^k(t,\varphi,\delta t) \right]^2 dt \Big/ \int_{noise} \left[\sum_{j=1}^{N} F_j^k(t,\varphi,\delta t) \right]^2 dt \right\}^{1/m} \tag{2.10}$$

Here σ_N represents SNR measured after stacking N receiver functions. $F_j^k(t,\varphi,\delta t)$ indicates the j-th receiver function (either R or T, before (δt=0s) or after delay time correction) in the k-th sub-

sample. The signal and noise time windows are taken as the Ps arrival time and a time interval before P. We varied N from 1 to M. For a signal, σ_N is expected to linearly increase with $N^{1/2}$, while for noise σ_N should stay at the same level regardless of an increase of N.

For comparison, we analyzed the relationship of σ_N versus $N^{1/2}$ for 6 types of data: 1) original T receiver function, $F_t(t)$; 2) polarity-corrected T receiver function with no correction of anisotropy, $F_t^p(t)$; 3) anisotropy-corrected T receiver function with no polarity changes, $F_t^c(t,\varphi,\delta t)$; 4) anisotropy-corrected T receiver function with polarity changes, $F_t^{cp}(t,\varphi,\delta t)$; 5) original R receiver function, $F_r(t)$; 6) anisotropy-corrected R receiver function, $F_r^c(t,\varphi,\delta t)$. In an anisotropic media, the Ps signals on T component have a four-lobed change in waveform polarity. We thus would not expect any increase of σ_{N1} for a plain stack of the original T receiver functions without considering the polarity changes across back azimuth. On the other hand, σ_{N2} is expected to increase steadily once the polarity changes are taken account. In other words, we expect σ_{N1} to stay flat and σ_{N2} to increase linearly with $N^{1/2}$. Once crustal anisotropy is corrected, the T receiver functions consist mainly of random noise, so the stacked amplitude will remain roughly similar regardless whether the waveform polarity was switched properly before the stacking. Thus σ_{N3} and σ_{N4} should be independent of N. Meanwhile, the stacked amplitude of anisotropy-corrected R receiver functions is expected to have higher SNR than the stack of the original ones, i.e., $\sigma_{N6} > \sigma_{N5}$.

2.3. Synthetic tests

We have conducted extensive synthetic tests to examine the reliability and robustness of the joint estimate. In particular, we want to learn: 1) how well the method recovers the input

anisotropy including two-layered anisotropic model; 2) how robust the measurement is under the presence of noise, lack of a full coverage in back azimuth, and other inhomogeneous structures such as a dipping Moho, azimuthal variation in velocity structure and mantle anisotropy; and 3) how significant anisotropy is required from data.

We computed synthetic seismograms with an epicentral distance of 60° and source depth of 0 km using the ray summation method developed by Frederiksen and Bostock (2000). The velocity models used in the synthetic tests are listed in Table 2.1, which includes: 1) a one-layered anisotropic crust model; 2) a one-layered isotropic crust model; 3) a one-layered isotropic crust with a dipping Moho model; 4) a one-layered heterogeneous crust model with a four-quadrant azimuthal variation in velocity; 5) a two-layered anisotropic crust model; and 6) a one-layer isotropic crust model with anisotropic mantle.

Receiver functions were computed using equation 2.1 with one of the following back azimuthal coverages: 1) a full coverage in back azimuth (from 0° to 350° in every 10° interval); 2) one-side coverage in back azimuth (from 0° to 175° in every 5° interval); or 3) the back azimuth distribution recorded at station XJ.YCH (239 receiver functions, with a good coverage in the back-azimuthal ranges of 0°-200° and 270°-360°). In order to test the robustness of the joint estimator, we added two levels (30% and 60%) of white noise to the synthetic data. We tested a total of 10 cases, which are listed in Table 2.2. In the following paragraphs, we show the results from the individual and joint estimators and discuss how well they were able to recover the input models. In all the cases, the joint estimator provided more accurate estimates of the input seismic anisotropy than the individual measurement does. In test case 1, synthetic receiver

functions were computed with a one-layered anisotropic crust model (M1 in Table 2.1) without adding any noise and, thus, each of the individual measurements was able to accurately recover the input crustal anisotropy (φ=0°, δt=0.50s) (Figures 2.3a-2.3c). The maximum amplitude of the JOF is 10.372, which is a strong evidence for the presence of seismic anisotropy in the data.

Case #	Velocity model	Back-azimuth distribution	Noise level	φ	δt (s)	I_{max}	SNRT analysis
1*	M1	full	0%	0°	0.50	10.372*	Positive*
2*	M1	full	30%	3°	0.48	1.866*	Positive*
3*	M1	full	60%	-4°	0.50	1.353*	Positive*
4*	M1	real	30%	3°	0.48	1.781*	Positive*
5	M2	full	30%	-40°	0.10	1.034	Negative
6	M3	full	30%	-27°	0.04	1.003	Negative
7	M3	one-side	30%	9°	0.18	1.084	Negative
8	M4	full	30%	12°	0.10	1.043	Negative
9*	M5	full	30%	16°	0.30	1.280*	Positive*
10	M6	full	30%	70°	0.06	1.002	Negative

*Anisotropic crust cases

Table 2.2: List of cases tested with synthetic data

At 30% noise level (case 2 in Table 2.2), the three individual objective functions (IOFs) are shown in Figures 2.4a, 2.4b and 2.4c, and the measured splitting parameters are (φ=1°, δt=0.64s) for cosine moveout correction, (φ=2°, δt=0.54s) for R cc maximization and (φ=3°, δt=0.44s) for T energy minimization, respectively. The JOF is shown in Figure 2.4d, which shows a maximum at (φ=3°, δt=0.48s). The delay time here is slightly closer to the input value. The maximum amplitude of the joint measurement is 1.866, suggesting that the observed anisotropy is significant. The SNRT with the T receiver functions indicates that σ_{N2} (stacked after a correction of waveform polarity) increases linearly with $N^{1/2}$ (open circle in Figure 2.4e) while σ_{N1} (stacked without a correction of waveform polarity) remains nearly flat across the whole range of $N^{1/2}$ (open squares in Figure 2.4e). On the other hand, once anisotropy is

removed, the T receiver functions are composed mainly of random noise, leading to a flat distribution of σ_{N3} (with a polarity correction, filled circles in Figure 2.4e) and σ_{N4} (without a polarity correction, filled squares in Figure 2.4e). The SNRT with the R receiver function data are shown in Figure 2.4f. A correction of crustal anisotropy also seems to result in a more constructive stacking, leading to a higher SNR ($\sigma_{N6}>\sigma_{N5}$). The results from the SNRT analysis here, together with the relative large maximum amplitude shown in the joint image, indicate a clear influence of seismic anisotropy on the receiver function data.

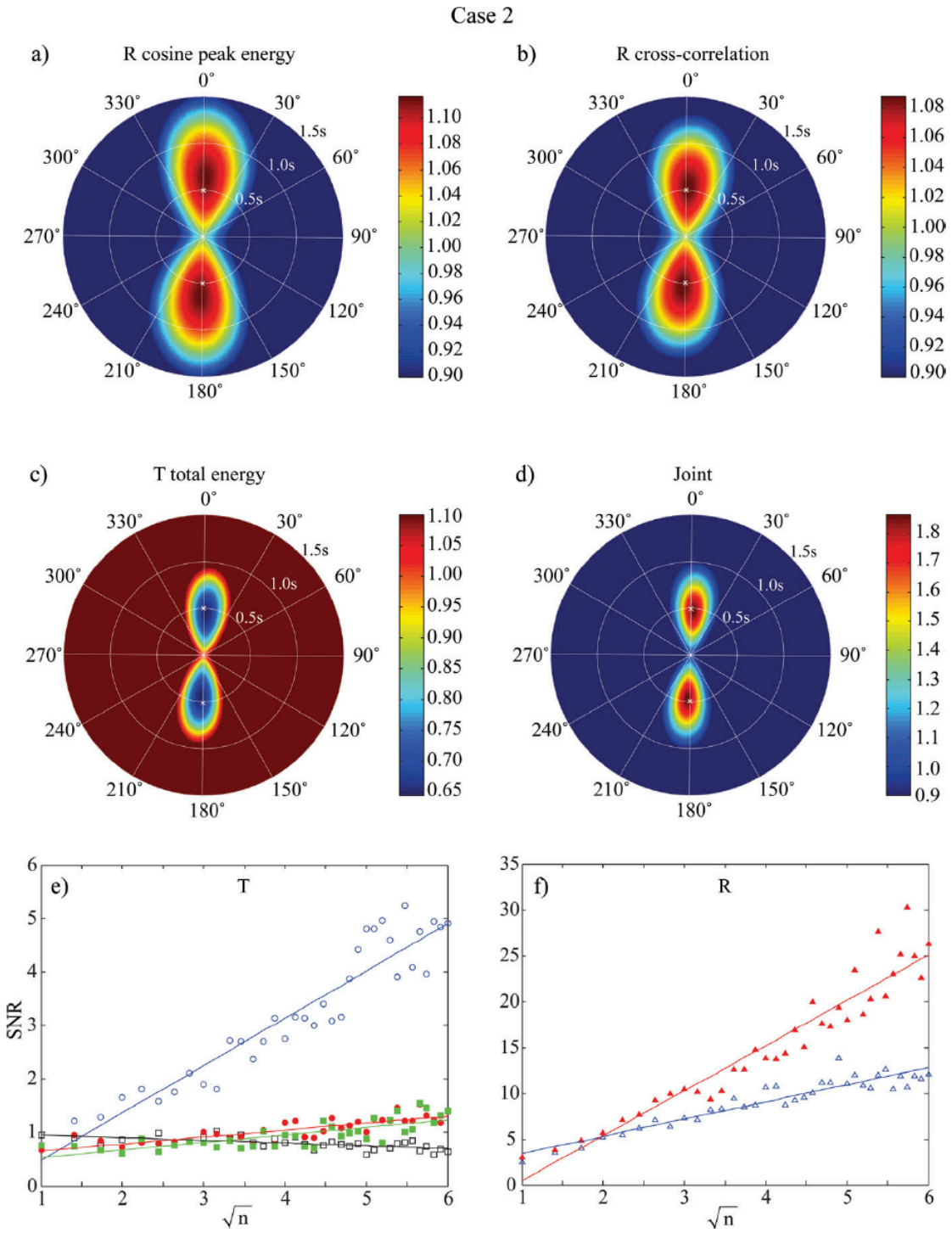

Figure 2.4. Results from test case 2. (a-d) here are similar to (a-d) shown in Figure 2.3, except that the synthetic receiver functions were computed using the anisotropic model, M1 (Table

2.1), with 30% white noise. Results of the SNRT analysis with the T and R receiver function data are shown in (e) and (f), respectively. Open and filled symbols represent SNRs calculated from stacks of receiver functions before and after the removal of seismic anisotropy determined by the JOF. Results from stacks of the T receiver functions with an appropriate change in waveform polarity are shown in circles, while those from stacks of T and R receiver function without sign changes are indicated by squares and triangles, respectively. Solid lines indicate results from linear regressions of each group. Note the steady increase of circles (stack with a sign correction) with increasing $N^{1/2}$ in (e) and that the filled triangles are always above the open ones in (f).

At 60% noise level (case 3 in Table 2.2), the three individual measurements are (φ=-10°, δt=0.46s), (φ=-11°, δt=0.46s), and (φ=0°, δt=0.58s) (Figure 2.5a-2.5c); the first two had a larger deviation from the input fast direction (φ=0°). The joint solution of the splitting parameters is φ =-4° and δt=0.50s, closer to the true values (Figure 2.5d). The maximum amplitude of the joint measurement is 1.353, indicating that the anisotropy-induced signature in the data is significant. The SNRT analyses with T and R receiver functions are shown in Figure 2.5e and Figure 2.5f, respectively. Both show the diagnostic features of crustal anisotropy, as discussed in the test case 2.

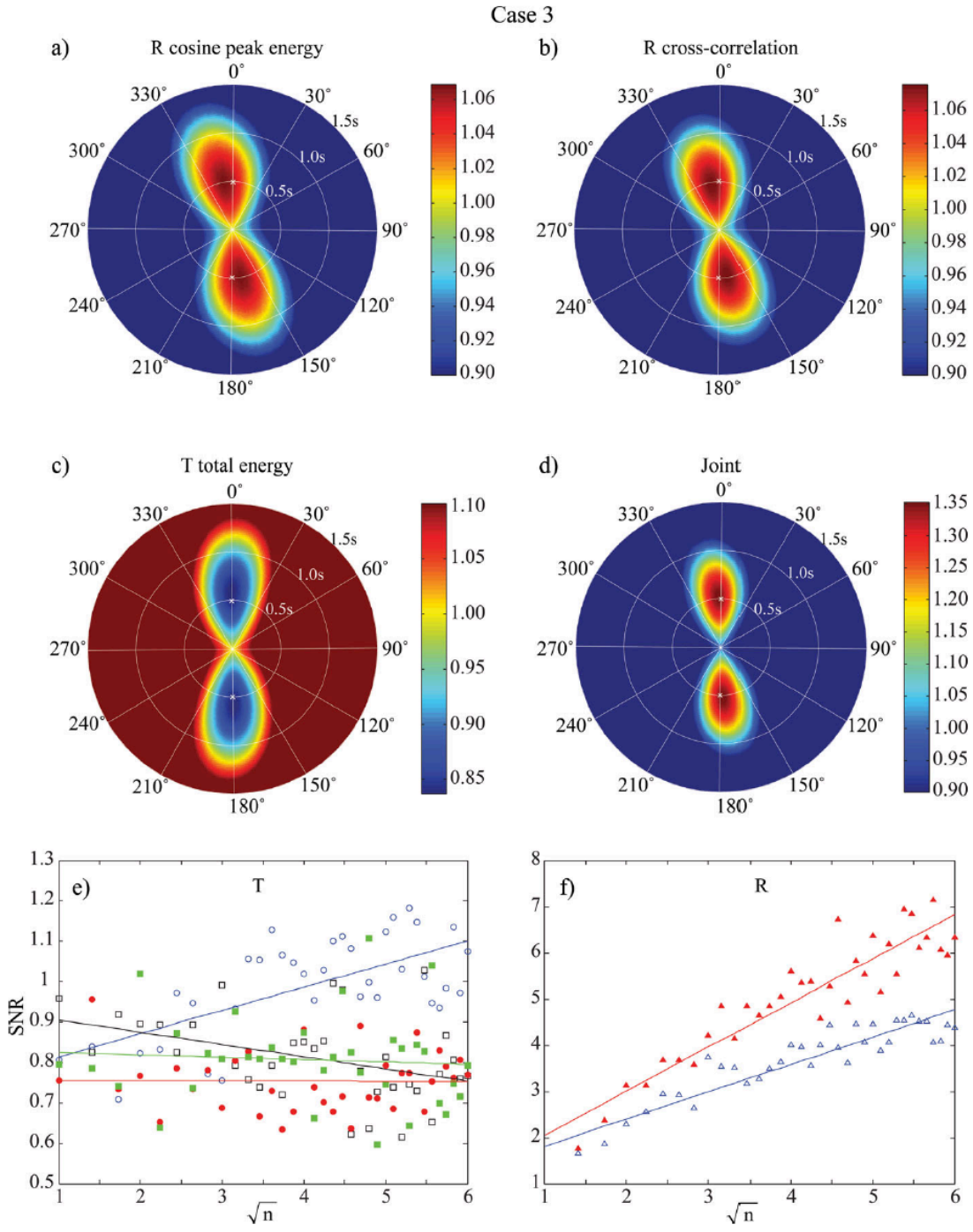

Figure 2.5. Results from test case 3. Same as Figure 2.4 except that the synthetic receiver functions were computed with the same M1 model but a higher noise level (60%). The SNRT analysis shows similar features to those in Figure 2.4.

In test case 4, we generated synthetic receiver functions with a more realistic back azimuthal coverage (here we use the same one as observed at a permanent seismic station, XJ.YCH, in Xinjiang province, China) and a noise level of 30%. The analyzed results are shown in Figure 2.6, which are (φ=0°, δt=0.50s), (φ=1°, δt=0.50s), (φ=3°, δt=0.48s) and (φ=3°, δt=0.48s). The maximum value of JOF, the indicator of seismic anisotropy, is also at high level, 1.781. The SNRT analysis also performed reasonably well. SNR measured from stacked receiver functions with a polarity correction, σ_{N2}, shows a steady increase with $N^{1/2}$ (open circle in Figure 2.6e). Note that we used 200 receiver function pairs in this test case, thus we can confirmed the linear growth of σ_{N2} up to $N^{1/2}$=14, while in the previous three tests with a full back-azimuthal coverage, we used only 36 receiver functions, yielding a maximum of $N^{1/2}$=6. We also noticed that the SNR computed from the original T receiver functions without a polarity correction, σ_{N1}, showing a slight increase with $N^{1/2}$ (open squares in Figure 2.6e). This probably can be attributed to the uneven distribution in back azimuth of the data. The uneven distribution caused an unbalanced stacking. On the other hand, σ_{N3} computed from stacking of anisotropy-removed receiver functions with a polarity correction slightly increases. We speculate that corrections with seismic anisotropy and waveform polarity might have introduced coherent noise to the T receiver functions, for example, a projection of signals onto the R components.

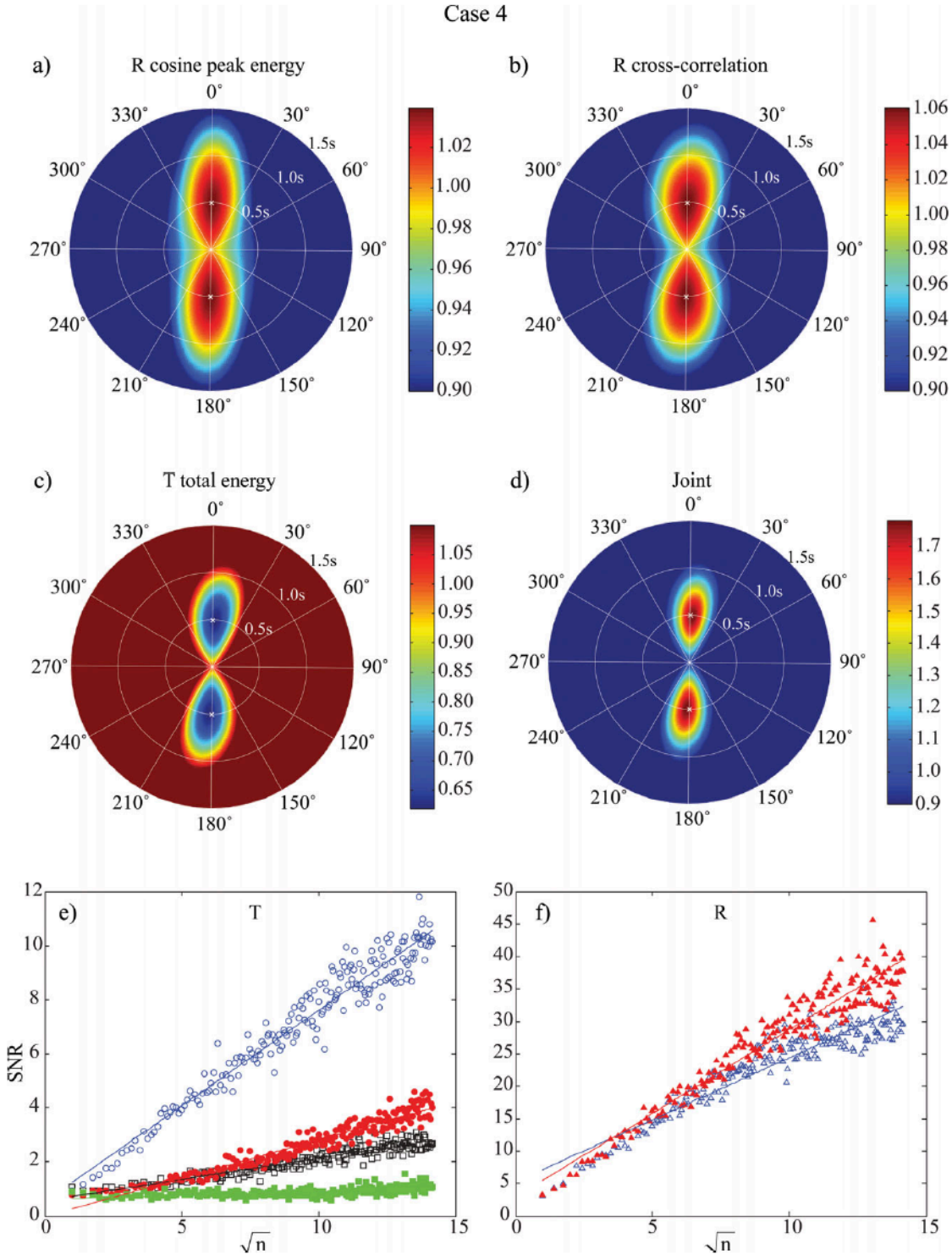

Figure 2.6. Results from test case 4. Same as Figure 2.4 except that the synthetic receiver functions have a different coverage in back azimuth. The back azimuthal distribution of 200

events recorded at station XJ.YCH was used here. Both the SNRT analysis and the high maximum value of the JOF indicate the existence of seismic anisotropy in the data.

We also test the performance of the joint analysis on an isotropic medium (test case 5 in Table 2.2). Results from individual measurement are shown in Figures 2.7a-2.7c. The estimated fast direction and splitting times are (φ=-10°, δt=0.06s), (φ=-15°, δt=0.08s), and (φ=-42°, δt=0.12s). The joint estimate is (φ=-40°, δt=0.10s), which appears to rely heavily on the T energy estimator. The maximum amplitude of joint measurement, which we used as an indicator of anisotropy, is only 1.034, suggesting that there is little or no evidence of seismic anisotropy in the data. This is also consistent with the SNRT results. We observed no significant increase of σ_{N2} with $N^{1/2}$ from the stacking of the T receiver functions (open squares in Figure 2.7e), and no substantial difference between σ_{N6} and σ_{N5} with the stacks of the R receiver functions (Figure 2.7f).

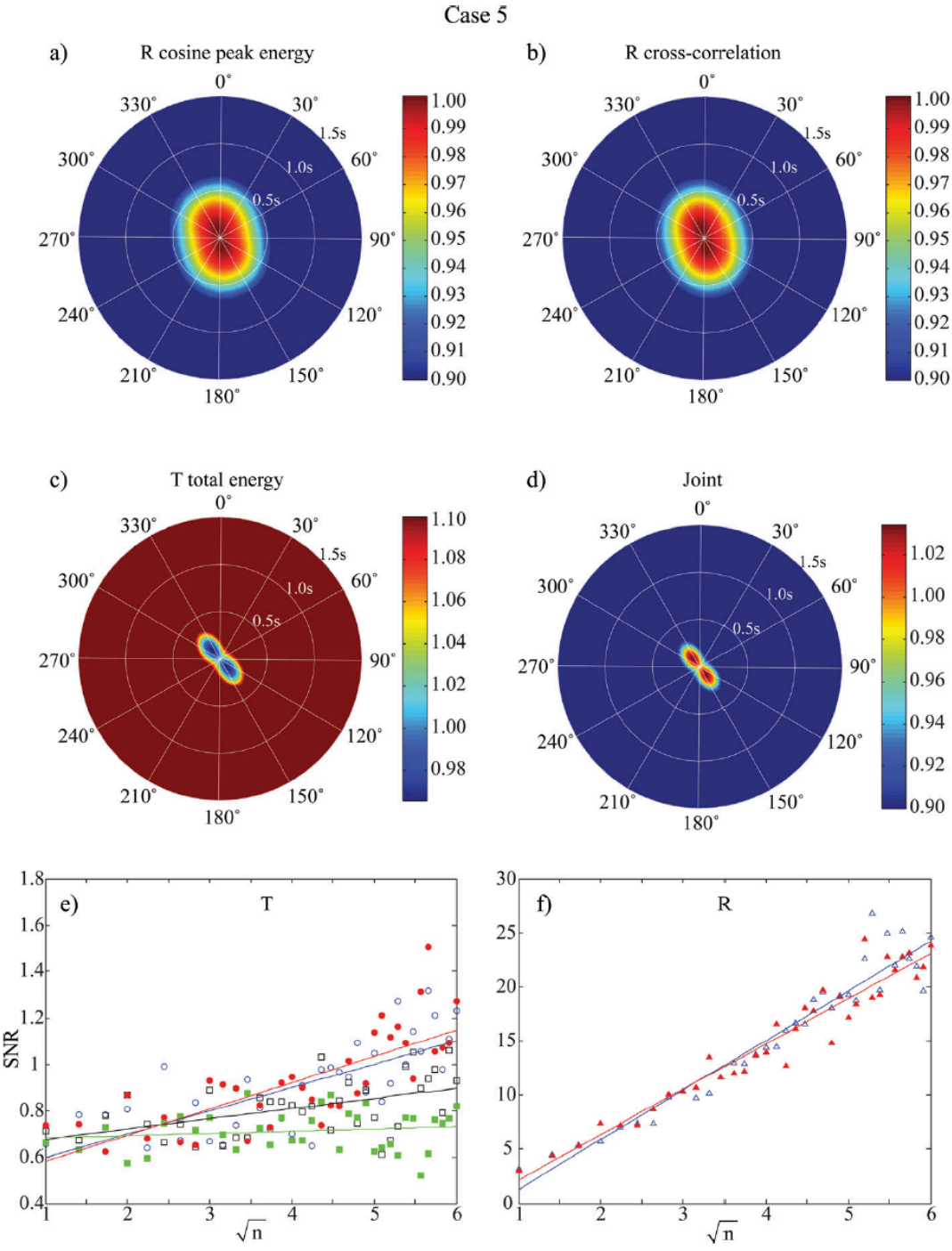

Figure 2.7. Results from test case 5. Same as Figure 2.4 except that the synthetic receiver functions were computed with the one-layered isotropic model, M2, and 30% white noise. The

SNRT analysis didn't show any characteristic features of seismic anisotropy, which is also consistent with the low maximum value of the JOF.

Besides crustal anisotropy, a dipping Moho can also generate Ps conversion in the T component, and cause back-azimuthal variations in the R and T receiver functions (Figures 2.8a and 2.8b). The dominant variations, however, follow the cosθ pattern, where θ is the back-azimuth, in contrast to the cos2θ change seen from anisotropic data (e.g., Frederiksen and Bostock, 2000; Shiomi and Park, 2008; Bianchi et al., 2010). Shiomi and Park (2008) and Bianchi et al. (2010) noticed the above features and proposed a harmonic analysis to extract the dipping and anisotropy structure, respectively, from receiver function data. They found that it is possible to separate the two even with the amplitude variation shown on the R and T receiver functions when a full range of back azimuthal data is available. We also performed the synthetic tests with a dipping Moho (M3 in Table 2.1) to see how well the isotropic crust is constrained with different coverage in back azimuth.

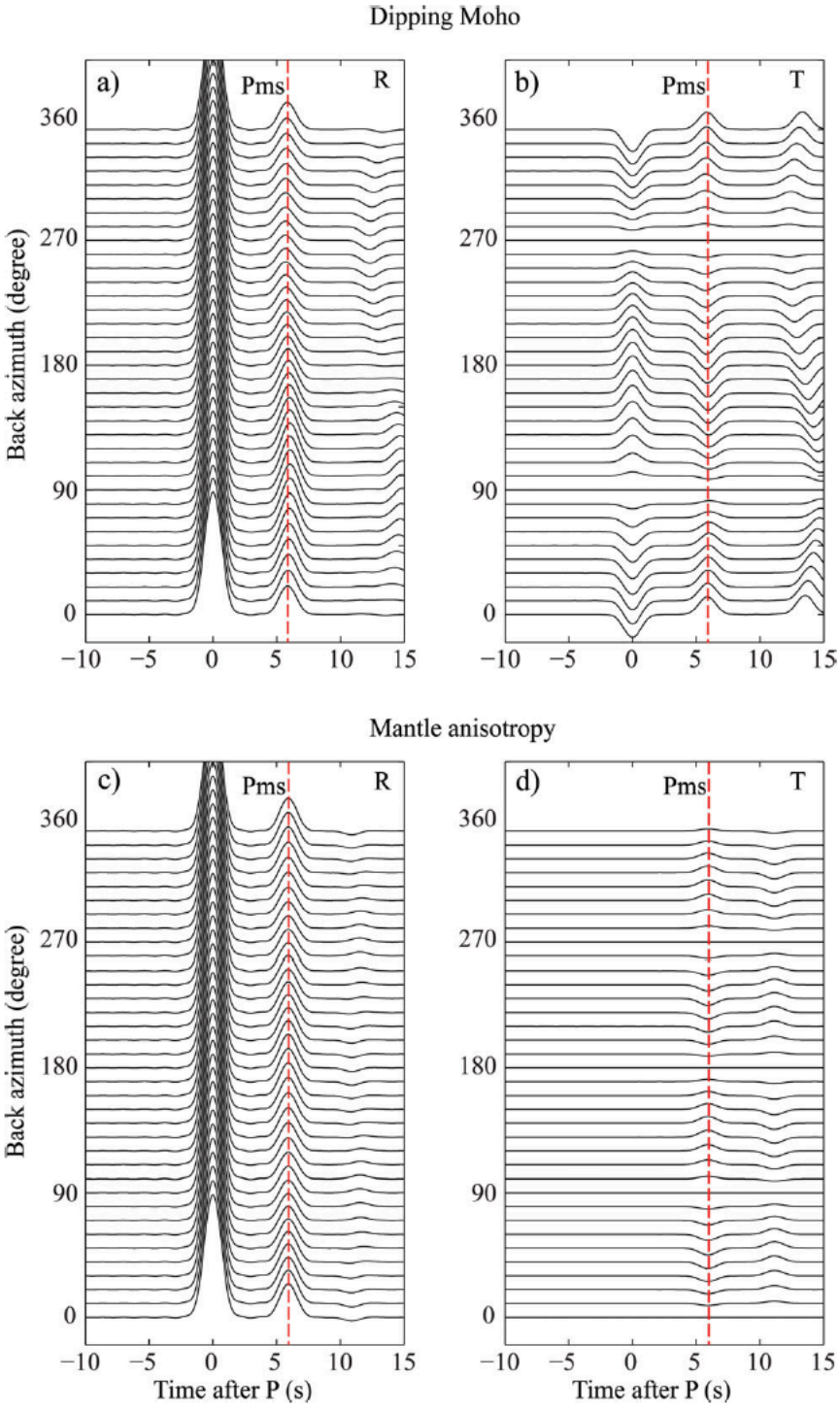

Figure 2.8. Synthetic R and T receiver functions computed from the dipping Moho model, M3 in Table 2.1, and the anisotropic mantle model, M6 in Table 2.1, are shown in (a, b) and (c, d),

respectively. All are plotted as a function of back azimuth. The T receiver functions shown in (b) and (d) are magnified by a factor of 2.

In test case 6, we first used a full back azimuth to constrain azimuthal anisotropy in the crust. We generated receiver functions with an isotropic crustal layer underlain by 10° dipping Moho. We added 30% white noise in computing synthetic receiver functions. The IOFs computed from these receiver functions are shown in Figures 2.9a to 2.9c, and the measured fast direction and splitting time are (φ=37°, δt=0.06s), (φ=12°, δt=0.08s), and (φ=-41°, δt=0.06s). The JOF is shown Figure 2.9d, and shows an apparent anisotropy of φ=-27° and δt=0.04s. The maximum amplitude of the joint image, however, is only 1.003, suggesting that anisotropy in the data is insignificant. The SNRT analysis applied to the T receiver functions shown in Figure 2.9e indicates that the SNR based on stacks with a polarity correction, σ_{N2}, did increases with $N^{1/2}$, but have no significant difference compared to the other three indices (σ_{N1}, σ_{N3}, and σ_{N4}). This suggests that the no significant anisotropic signals exist on the T component. The SNRT with R receiver function also shows no substantial difference in SNR computed from stacks before or after the correction of seismic anisotropy (Figure 2.9f).

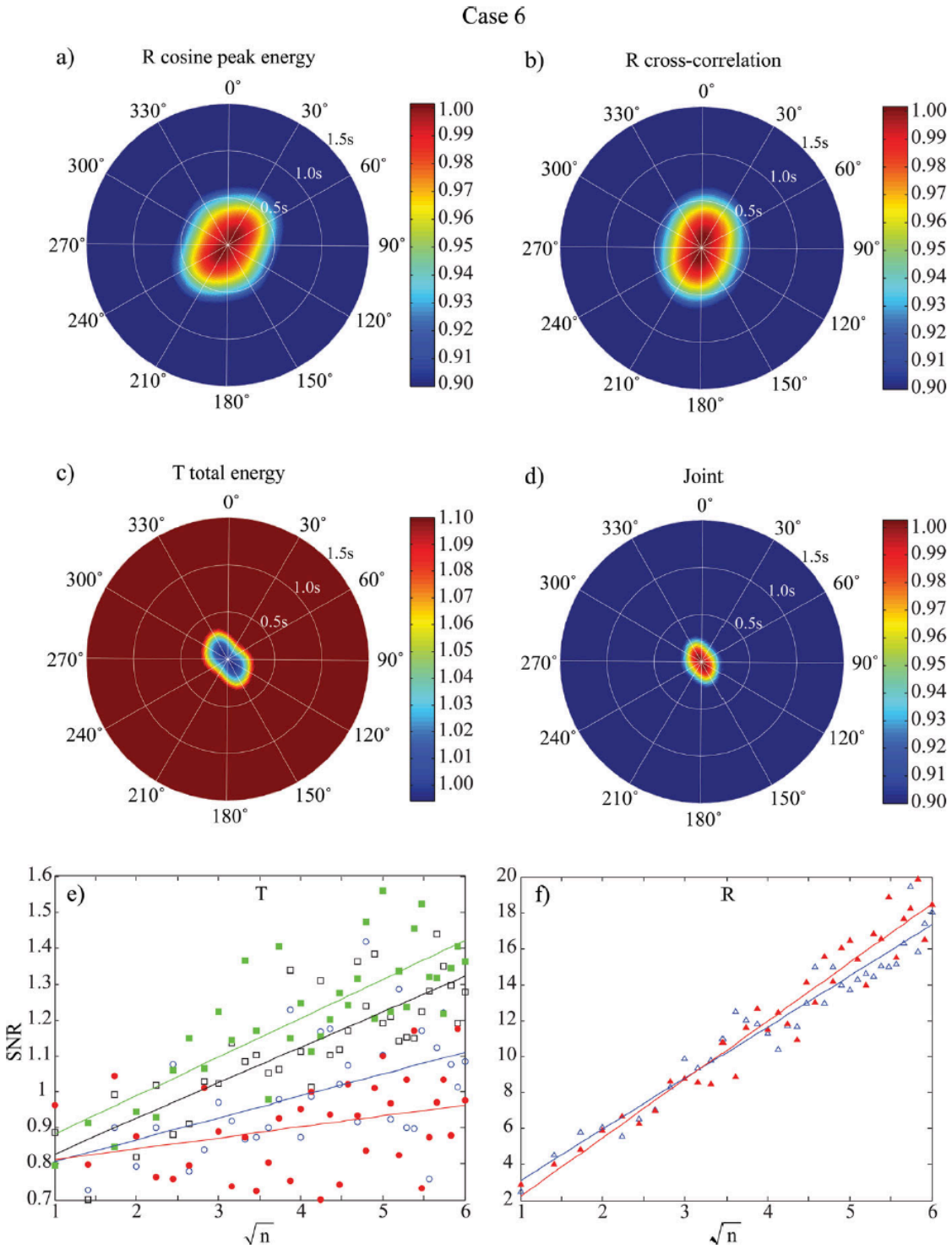

Figure 2.9. Results from test case 6. Same as Figure 2.4 except that the synthetic receiver functions were calculated using the model M3 in Table 2.1 (a one-layered isotropic crust plus a

dipping Moho). Random noise was set to the same 30% level. Note the low maximum value of the JOF shown in (d). The SNRT analysis also indicates a weak anisotropy in the data. Both results suggest that our integrated analysis can resolve seismic anisotropy from dipping interface when the back azimuthal coverage of the data is good.

While the joint analysis here appears to be able to separate anisotropy from dipping structure given a good coverage in back azimuth, we further tested whether this is true even under conditions when back-azimuth coverage of the data is limited. In test case 7, we generated synthetics with a one-side back-azimuthal distribution, and 30% white noise. All the individual measurements show a relatively large apparent splitting time of δt=0.24s, δt=0.20s, and δt=0.16s, with a fast direction of φ=8°, φ=5°, and φ=9°, respectively (Figures 2.10a-2.10c). The joint measurement also yielded an apparent anisotropy with φ=9° and δt=0.18s (Figure 2.10d). The maximum amplitude of joint measurement is, however, as low as 1.084, which is consistent with the results of the SNRT analysis. Both indicate that the observed anisotropy is not a reliable feature in the data.

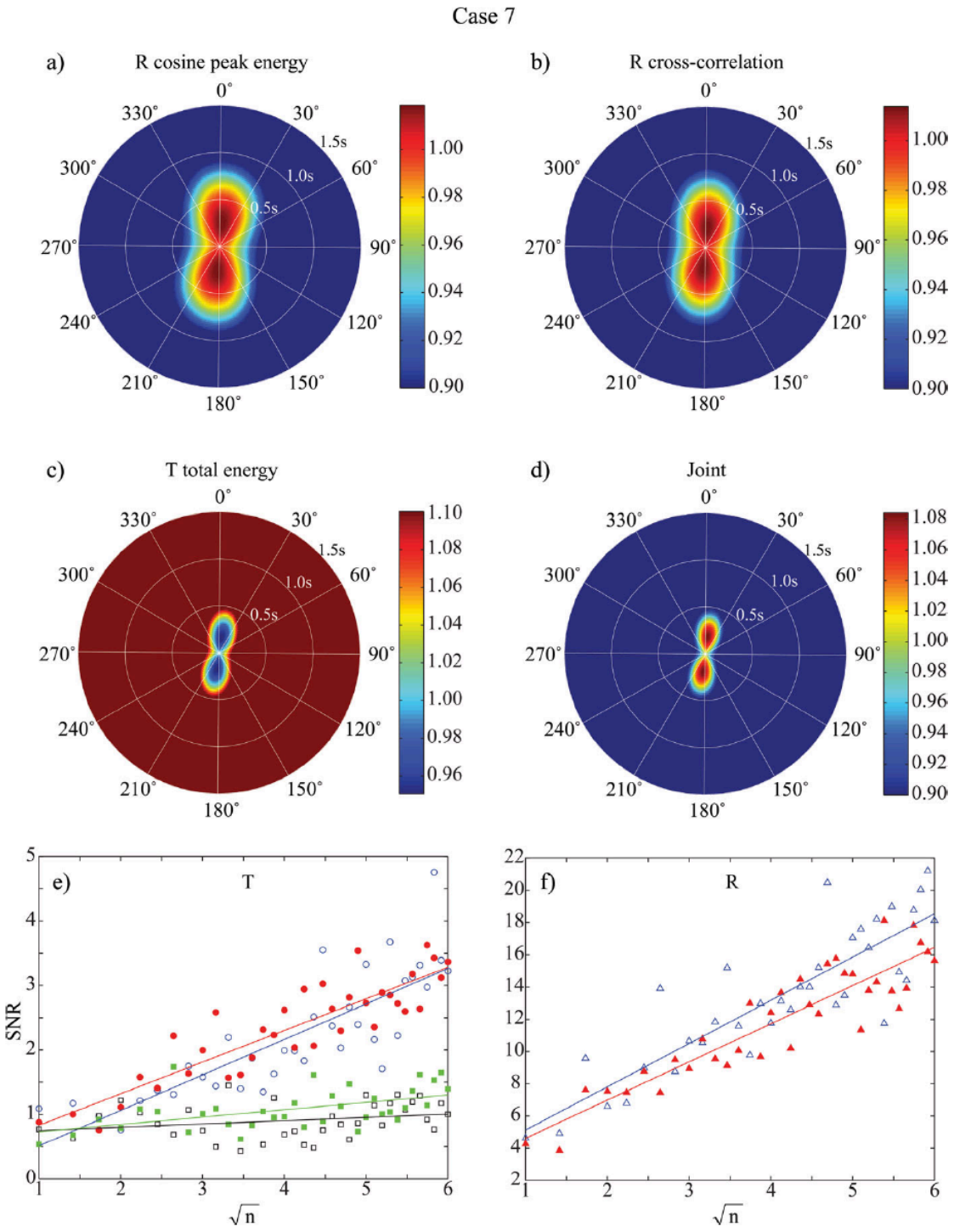

Figure 2.10. Results from test case 7. Same as Figure 2.9 except that the back azimuths of the synthetic receiver functions are limited to one side (back azimuth 0-175°). Note the relatively large apparent splitting times (~0.2s) estimated with the IOFs (a-c) and JOF (d). However, the

maximum value of the JOF is low, and the SNRT analysis also indicates a weak anisotropy in the data. Thus the estimated splitting parameters here are not considered to be reliable.

In test case 8, we tested how lateral heterogeneities in crustal velocity structure affect our anisotropy measurements. As shown in Figure 2.1, seismic anisotropy introduce a four-lobed variation in the peak Ps arrival time and Ps polarity on the R and T receiver functions, respectively. To mimic the anisotropic effect, we set up a model with two velocity values alternating from quadrant to quadrant (M4 in Table 2.1). Using this model we generated synthetic receiver function with 30% white noise. We then computed the IOFs and JOF with the corresponding R and T receiver functions, which are shown in Figure 2.11. The maximum of the individual functions occurred at (φ=0°, δt=0.52s), (φ=2°, δt=0.32s), and (φ=20°, δt=0.06s), respectively, while the joint function shows a maximum at (φ=12°, δt=0.10s). The maximum amplitude of the JOF is only 1.043, suggesting that there is little or no seismic anisotropy in the data. The SNRT analyses with T (Figure 2.11e) and R (Figure 2.11f) also show no evidence of seismic anisotropy in the data, suggesting the observed small amount of anisotropy might be an artifact.

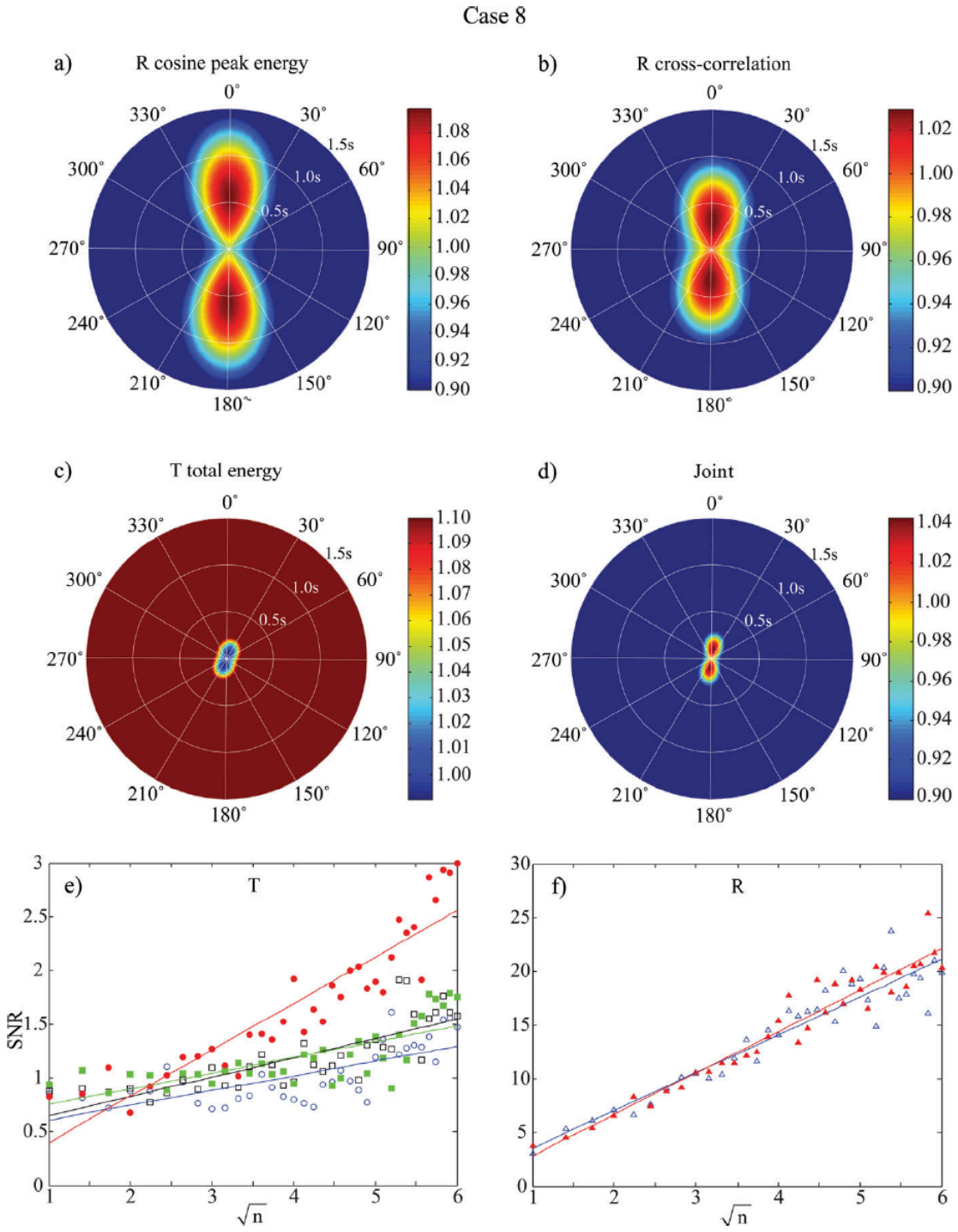

Figure 2.11. Results from test case 8. Same as Figure 2.4 except that the synthetic receiver functions were calculated using the one-layered laterally varying velocity model, M4 (Table 2.1), with 30% white noise. Note that the IOF corresponding to the cosine moveout correction

shows large splitting time. On the other hand, the JOF has a low maximum value, and the SNRT analysis also indicates no significant anisotropy in the data. Thus the proposed integrated analysis here can also resolve seismic anisotropy from heterogeneous structure.

In test case 9, we used a model consisting of two anisotropic layers with different fast polarization directions (M5 in Table 2.1). The individual measurements show an apparent anisotropy with fast direction $\varphi=11°$, $\varphi=16°$, $\varphi=16°$ and splitting time $\delta t=0.22s$, $\delta t=0.28s$, $\delta t=0.32s$ (Figures 2.12a-2.12c), respectively. The joint measurement gave more or less the same estimate with a fast direction of $\varphi=16°$ and a delay time of $\delta t=0.30s$ (Figure 2.12d). The apparent anisotropy is consistent with a vector summation of the two splitting vectors computed from the upper and lower crust. Both the maximum amplitude of the JOF (1.280) and the SNRT analysis with the T (Figure 2.12e) and R (Figure 2.12f) receiver functions indicate the presence of seismic anisotropy in the data.

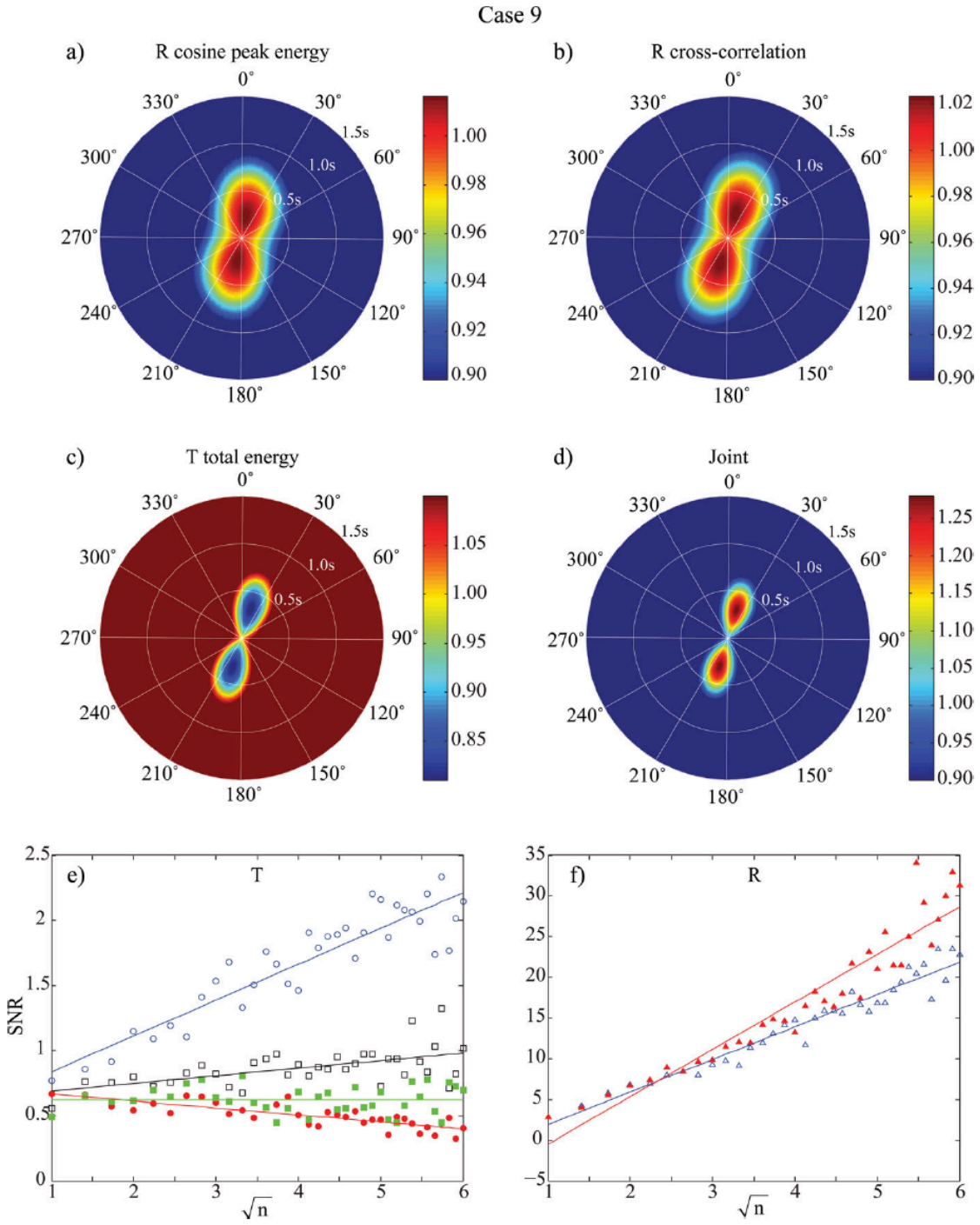

Figure 2.12. Results from test case 9. Same as Figure 2.4 except that the synthetic receiver functions were calculated using the two-layered anisotropic model, M5 (Table 2.1), with 30%

white noise. The JOF shows a large maximum value, and the SNRT also indicates the presence of seismic anisotropy in the data.

The last model we tested has a 50-km thick isotropic crust underlain by an anisotropic mantle (M6 in Table 2.1), in which case, the synthetics show clear Ps conversions in the transverse component. The corresponding R and T receiver functions also exhibit a cos2θ variation along the back-azimuthal direction, θ (Figures 2.8c and 2.8d). There is, however, no clear evidence of back-azimuthal variation in the Ps arrival time on the R component, as shown in Figure 2.1a. We also noticed that the waveforms of the Ps conversion are rather similar between the R the T receiver functions, in contrast to those computed from anisotropic models. In the latter case, the T component is approximately proportional to the time derivative of the R component (Figures 2.1a and 2.1b). The cos2θ back-azimuthal variation could be easily misinterpreted as crustal anisotropy if an analysis only relies on the amplitude of R and T receiver functions. In test case 10, we applied the joint analysis to the synthetic receiver functions computed from model M6. The individual measurements show an apparent anisotropy with fast direction φ=146°, φ=22°, φ=101° and a splitting time δt=0.08s, δt=0.02s, δt=0.04s (Figures 2.13a-2.13c), respectively. The joint measurement gave a fast direction of φ=101° and a delay time of δt=0.02s (Figure 2.13d). The maximum value of the JOF is as low as 1.002. This is consistent with the SNRT analysis (Figures 2.13e and 2.113f). Both show no evidence for crustal anisotropy.

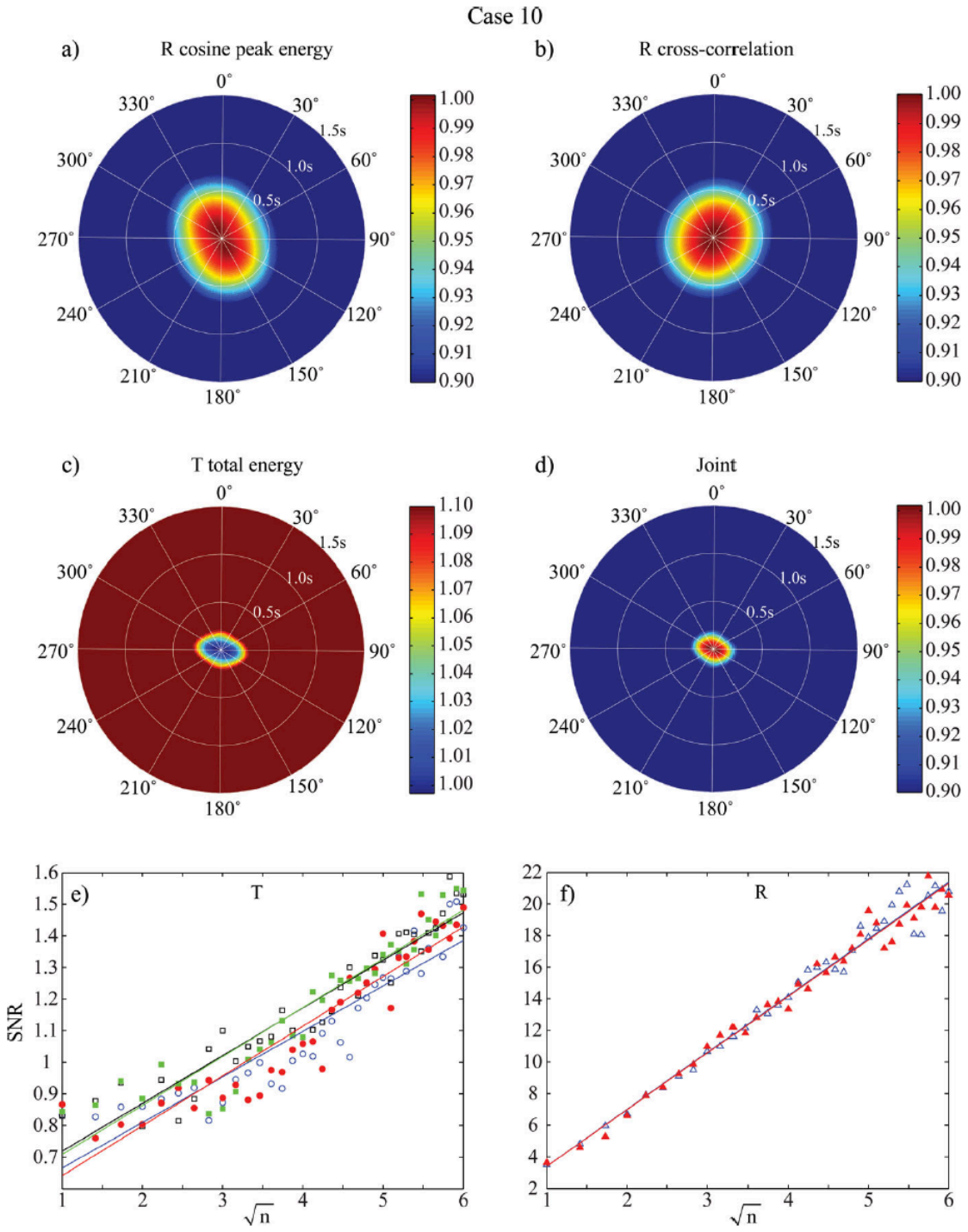

Figure 2.13. Results from test case 10. Same as Figure 2.4 except that the synthetic receiver functions were calculated using the anisotropic upper-mantle model, M6 (Table 2.1), with 30%

white noise. Note that the low maximum value of the JOF shown in (d). The SNRT analysis also indicates no presence of crustal anisotropy in the data.

Results of the joint measurement of the 10 cases are summarized in Table 2.2. In all cases, the maximum value of the JOF can be combined with the SNRT analysis to determine the existence of seismic anisotropy in the R and T receiver function data. If seismic anisotropy is required to explain the data, we can compute the three IOFs and their combination to obtain relatively robust estimate of crustal anisotropy in the data.

2.4. Data examples

We have applied this integrated technique to receiver function data recorded at two broadband stations, XJ.YCH and SC.JJS, in western China. Both stations belong to the permanent network of the China Earthquake Administration (CEA). XJ.YCH (77.361E, 37.390N) is located at the northern edge of the Tibetan plateau near the southwest corner of the Tarim basin, while SC.JJS (104.546E, 31.005N) is situated inside the Sichuan Basin east to the Tibetan plateau (Figure 2.14). We generated receiver functions from records of earthquakes that occurred at epicentral distances of 30°-90° between 07/2007 and 07/2010 with Mw≥5.8. The three-year dataset provided a good back azimuthal coverage (Figure 2.14 insets), which is essential for a robust estimate of crustal anisotropy.

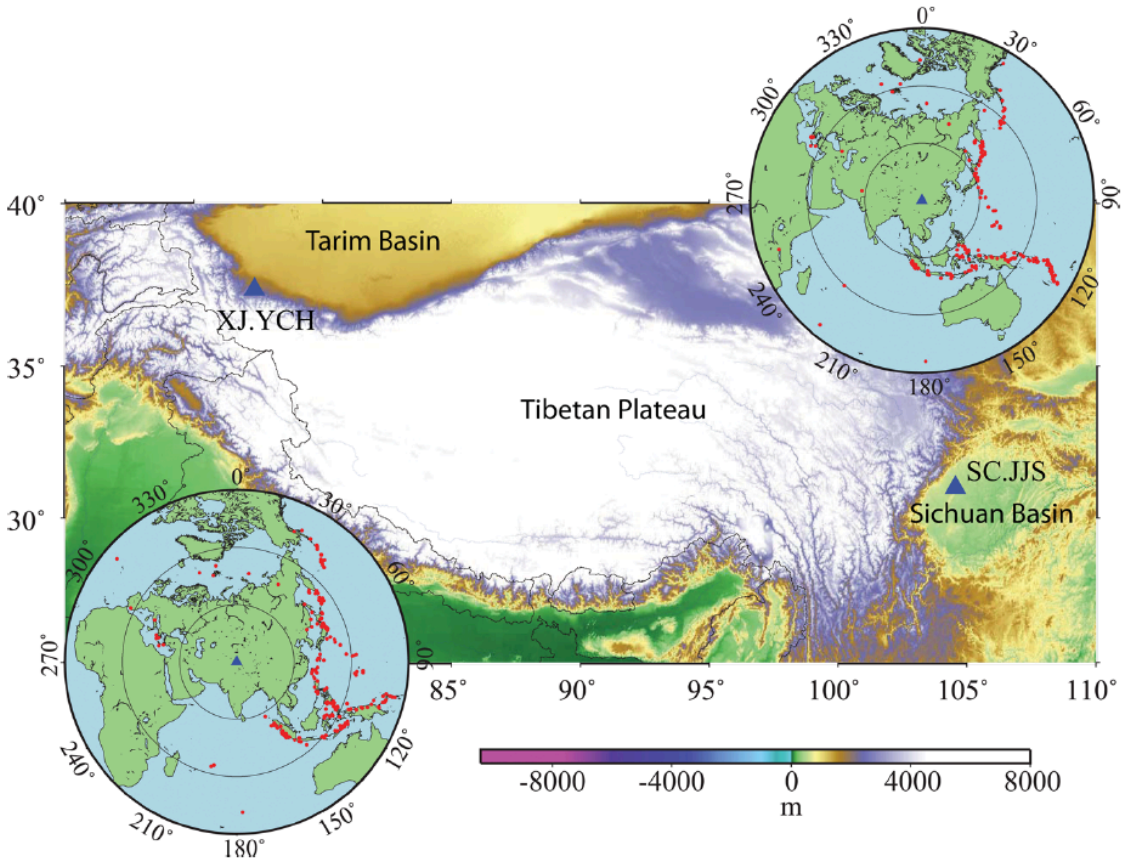

Figure 2.14. Map showing the geographic locations of two seismic stations XJ.YCH and SC.JJS used in this study. Insets show the back azimuthal distribution of the teleseismic events at epicantral distances between 30° and 90° with an Mw≥5.8.

Figure 2.15 shows the 239 selected receiver functions recorded at station XJ.YCH plotted as a function of back azimuth. The slightly negative moveout of the Moho Ps converted phase was corrected as if all the receiver functions were received at an epicentral distance of 60° and a focal depth of 0 km. The Moho converted Ps phase on the R receiver functions appears to exhibit a four-lobed variation pattern in arrival time (Figure 2.15a). It also seems that there are

polarity changes in the Ps waveform on the T receiver functions (Figure 2.15b). As mentioned above, these observed features suggest the existence of seismic anisotropy in the data.

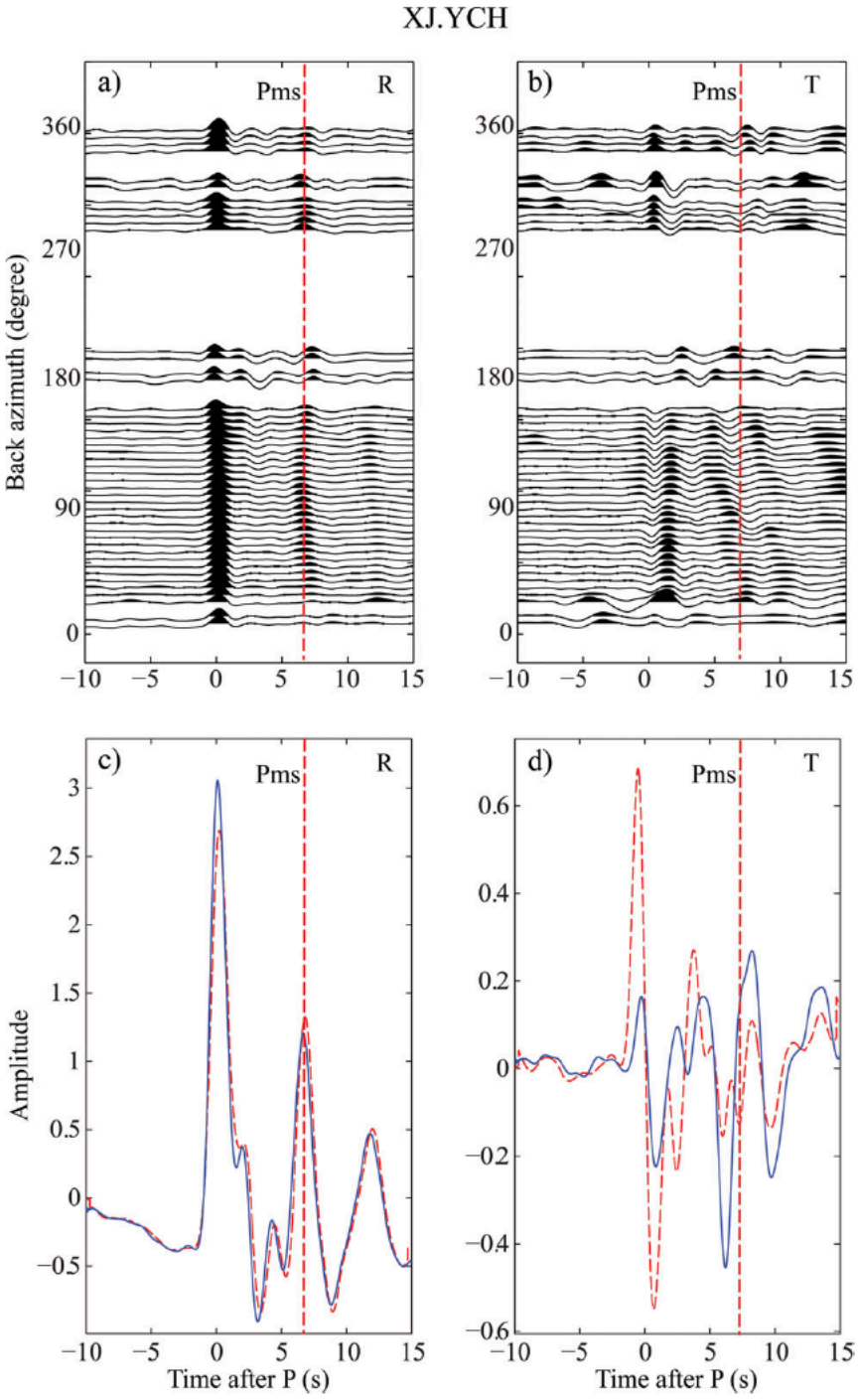

Figure 2.15. R (a) and T (b) receiver functions recorded at station XJ.YCH are plotted as a function of back azimuth (binned every 10°). The T receiver functions shown in (b) are magnified by a factor of 2. The vertical dashed line indicates the average arrival time of the Moho Ps converted phase. The stacked R receiver functions (c) and T receiver functions (d) before/after corrections of seismic anisotropy determined by the JOF are shown in solid/dashed lines respectively. Note that the Ps energy on the stacks of polarity-corrected T receiver functions is significantly reduced after the correction.

We computed the three IOFs and the JOF using the 239 receiver function data (Figure 2.16). The crustal anisotropy estimated from the first two IOFs show good agreement, with a fast direction of φ=~105° and a splitting time of δt=~0.65s. The fast direction measured with the T energy minimization is φ=125°, approximately 20° larger than the R measurements, with a delay time of δt=0.54s. The joint objective function reaches its maximum at (φ=110°, δt=0.58s) with a maximum value of 1.743 (Figure 2.16d). The SNR measured from stacked T receiver functions with a polarity correction, σ_{N2}, exhibited a steady increase with $N^{1/2}$, while those measured with other stacks (σ_{N1}, σ_{N3}, and σ_{N4}) show a very little increase with increasing N (Figure 2.16e). The SNR computed from stacks of R receiver functions after the removal of seismic anisotropy is also slightly higher than that calculated from the original R receiver functions. Both the maximum amplitude and the SNRT analysis indicate that the crust beneath this station is significantly anisotropic. Solid and dashed lines in Figures 2.15c and 2.15d represent stacked R and T (with changes in polarity) receiver functions before and after the correction. The amplitude of the Moho Ps conversion signal is enhanced on the stacked R receiver function but reduced on the stacked T receiver function after correction.

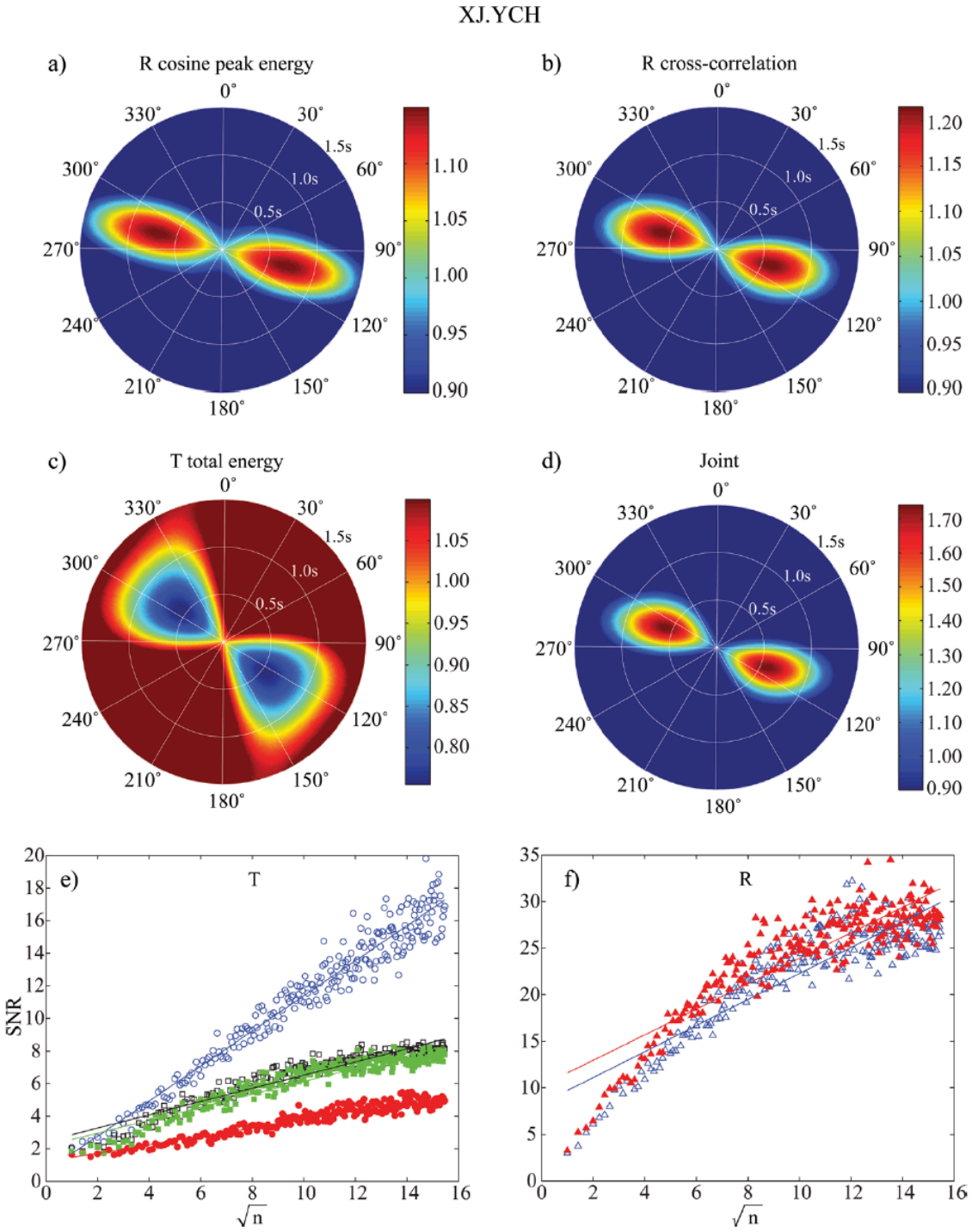

Figure 2.16. Results obtained at station XJ.YCH, which are plotted similarly to Figure 2.4. The three IOFs and the JOF are shown in (a), (b), (c) and (d), respectively. Results of the SNRT analysis based on the R and T receiver functions are shown in (e) and (d), respectively. Note

that in (e), only stacks from polarity-corrected T receiver functions (open circles) show a steady increase of SNR with increasing $N^{1/2}$, while the other stacks exhibited little to no dependence on N. Also stacks of R receiver functions after the correction of anisotropy show a slightly higher SNR than those from the original radial data.

Levin et al. (2008) analyzed SKS/PKS and receiver function data recorded by a temporary array deployed in the area near XJ.YCH for 6 months by a Sino-French group. XJ.YCH is closest to their station 108 (Figure 2 of Levin et al., 2008), where no measurement of crustal anisotropy is available. We thus compare our results with their measurements at stations 104 and 116, which are located approximately 50 km north and 110 km south of XJ.YCH, respectively. The SKS/PKS splitting data recorded at station 116 can be best explained by a one-layer anisotropic model of (φ=108°, δt=1.0s), or a 2-layer model of (φ=112-120°, δt=0.8-1.6s) and (φ=36-86°, δt=0.4-0.6s) for the upper and lower layer, respectively. The besting fitting model of receiver function data collected at station 104 has a ~10 km strong anisotropic layer above the Moho with a fast direction of 130°, which is consistent with the estimate of the third IOF and ~20° larger than the joint solution. The fast polarization direction observed here is roughly parallel to the Altyn Tagh fault in this area, along the direction of maximum horizontal tensile stress. We thus speculated that mineral alignment in the lower crust is likely responsible for the observed seismic anisotropy.

We have a total of 210 selected receiver functions recorded at the station SC.JJS inside the Sichuan basin. We first corrected the time-distance moveout of the Ps phase in the receiver functions then plotted in the order of back azimuth (Figure 2.17). We found no clear evidence of

any systematic variations in Ps waveform and arrival time with respect to back azimuth. The calculated three IOFs are shown in Figures 2.18a-2.18c and the JOF is shown in Figure 2.18d. The estimated crustal anisotropy from the two R and T measurements is (φ=149°, δt=0.08s), (φ=143°, δt=0.02s) and (φ=75°, δt=0.06s), respectively. The joint objective function reaches its maximum at (φ=79°, δt=0.06s) with a maximum value of 1.028. The SNRT analysis results with the T and R receiver functions are shown in Figures 2.18e and 2.18f, respectively. The calculated SNRs from receiver functions with different types of stacking didn't show any evidence of seismic anisotropy in the data. The insignificance of seismic anisotropy in the data can also be shown by comparing the stacked receiver functions before and after the correction of seismic anisotropy. Solid and dashed lines in Figures 2.17c and 2.17d represent the stacked R and T receiver functions before and after the correction. Waveforms within the Moho Ps arrival time window on both components show no significant changes after the removal of seismic anisotropy. The station is located within the Sichuan basin where very little deformation is observed at surface. Our observation here that the crust beneath SC.JIS has a rather isotropic velocity structure thus is consistent with surface observation and may indicate there is little crust-scale deformation inside the basin.

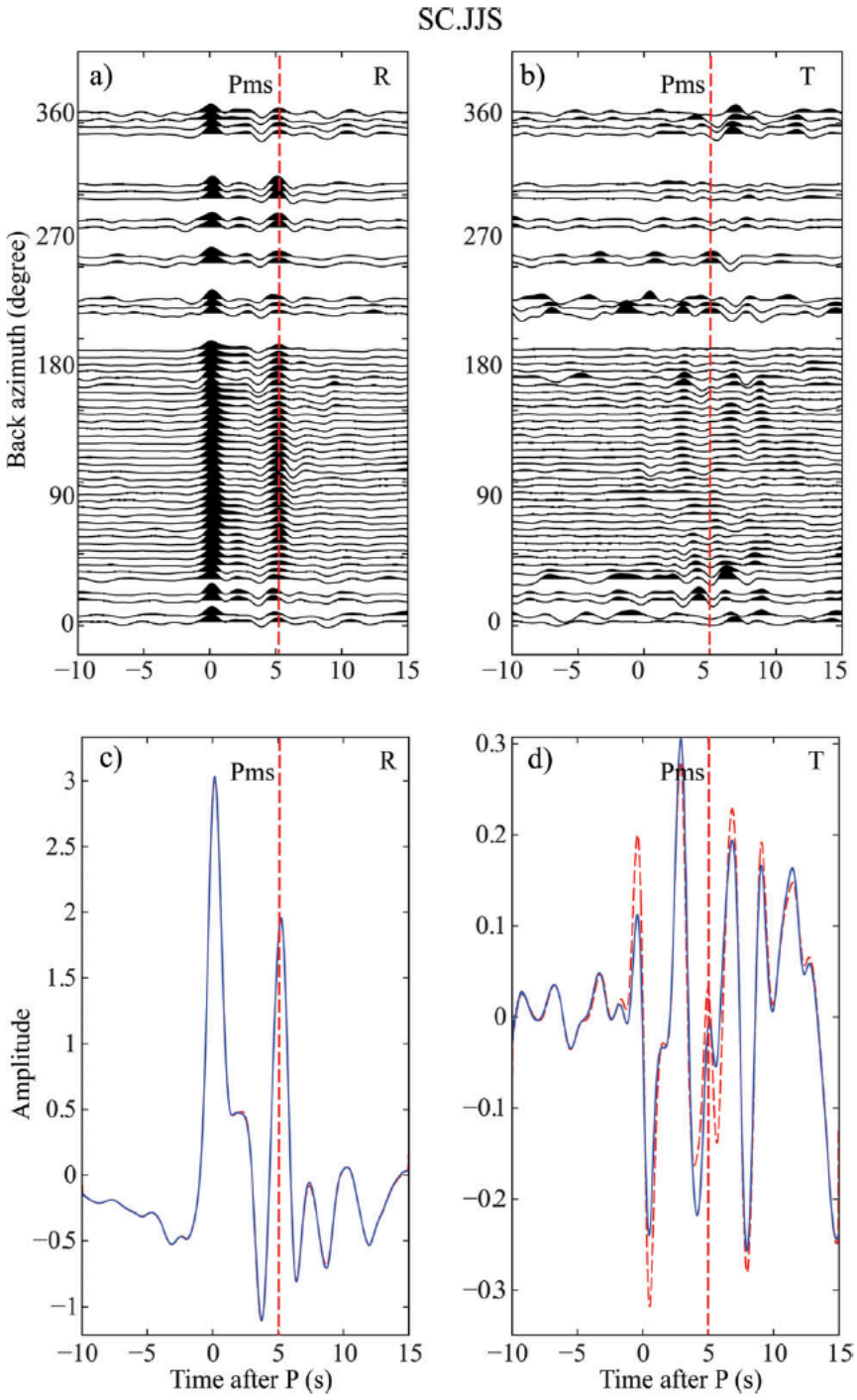

Figure 2.17. R a) and T b) receiver functions recorded at station SC.JJS are shown as a function as back azimuth (binned every 10°). The T receiver functions shown in (b) are magnified by a factor of 2. The vertical dashed line indicates the average arrival time of the Moho Ps converted

phase. The stacked R receiver functions (c) and T receiver functions (d) before/after corrections of seismic anisotropy determined by the JOF are shown in solid/dashed lines respectively. Note that the stacked Ps waveform after correction of seismic anisotropy remains almost the same on both components, suggesting crustal anisotropy is insignificant in the data.

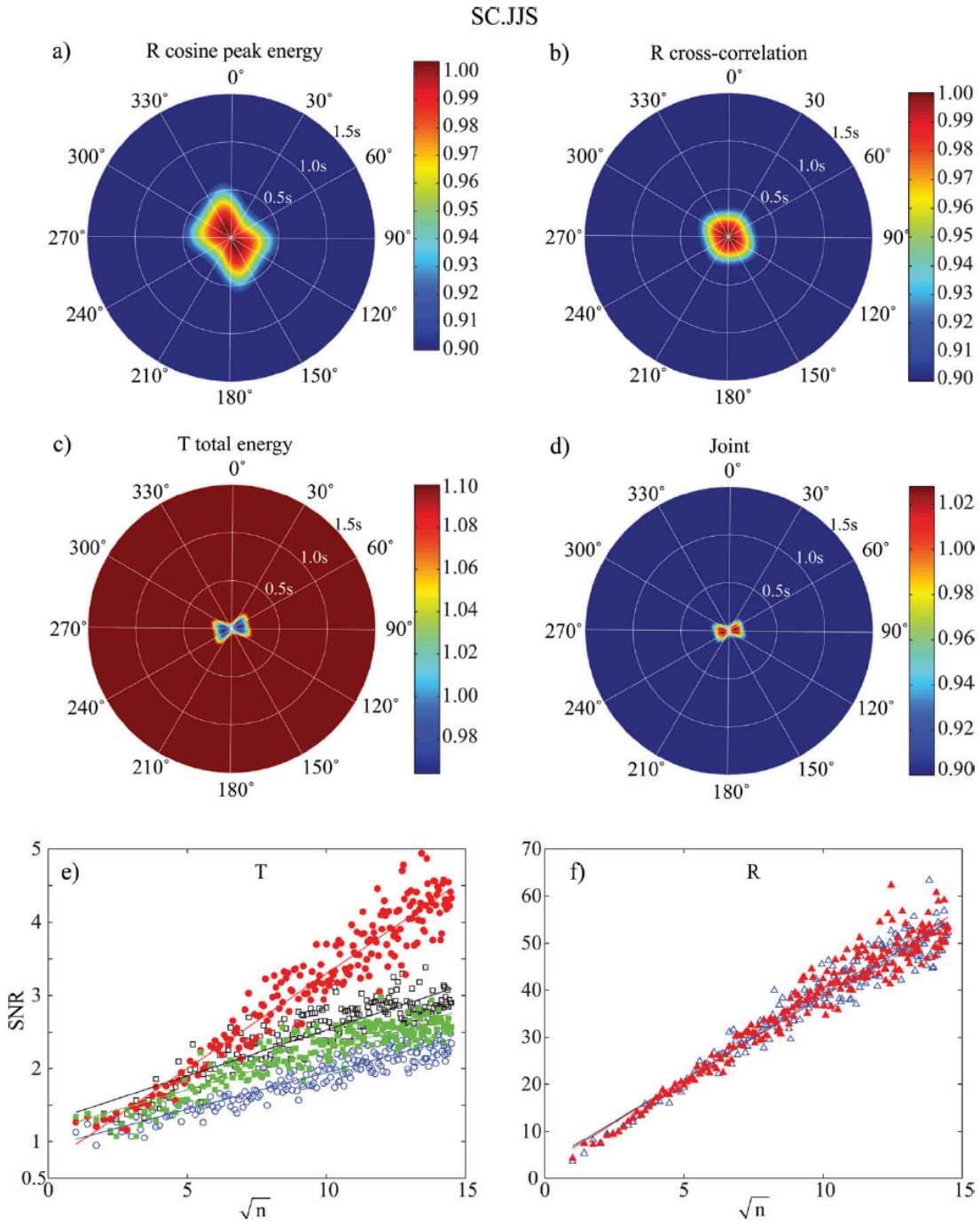

Figure 2.18. Results obtained at station SC.JJS, which are plotted similarly to Figure 2.4. The three IOFs and the JOF are shown in (a), (b), (c) and (d), respectively. Results of the SNRT analysis based on the R and T receiver functions are shown in (e) and (d), respectively. Note

that open circles in (e) show no significant increase with increasing N, and the open and filled triangles in (f) mix with each other, suggesting that there is a little to no anisotropy in the data.

2.5. Discussion and conclusions

The P to S converted phase at the Moho boundary is an ideal phase to study crustal anisotropy. Receiver functions, however, have not been extensively used in measuring seismic anisotropy in crust, since the Ps conversion is a very weak signal. Measurements with individual receiver function data can introduce large errors and even lead to wrong estimates of crustal anisotropy. We found that a joint analysis of all the receiver functions recorded at a single seismic station is a preferred approach.

We proposed three different ways to estimate seismic anisotropy in this study. As R receiver functions always have better SNRs than T receiver functions, it is conceivable to develop method to rely solely on R receiver functions to estimate crustal anisotropy. Our first method searches a pair of (φ, δt) that maximize the stacked Ps amplitude after a cosine moveout correction in the Ps arrival time. As a dipping Moho and velocity heterogeneities in crust could also cause back-azimuthal variations in Ps arrival time, we found this method has little resolution of anisotropy from the above two inhomogeneous structures, especially when the back azimuth coverage is poor (test cases 7 and 8, Figures 2.10 and 2.11). Our second and third methods make a full correction of seismic anisotropy on R and T receiver functions. They track the effects of the correction on the R cc and T energy, respectively. Between the two methods, the minimization of T energy appears to better recover the input models, although it could

misinterpret dipping Moho structure with crustal anisotropy when coverage in back azimuth is poor (case 7, Figure 2.10).

We equally weighted the three individual measurements when computing the JOF. As shown in the Appendix A, the significances of maximums of the three IOFs are proportional to δt^2, thus we have used it as the indicator of seismic anisotropy in the data. We also noticed that the maximum value of the T objective function is larger than those of the R estimators when noise level is low (comparing A7 with A2b and A4). As the JOF was computed by a geometric mean of the three objectives functions, we found that the joint estimates of seismic anisotropy tend to agree better with those of the T estimator in our tests (Figures 2.3 to 2.13). On the other hand, our synthetic tests indicated that measurements from the three methods are generally consistent with each other, thus the selection of different weights appears to have little effects on the joint estimates.

Besides the maximum value of the JOF, we also found that the SNRT analysis can be used to verify whether there is significant seismic anisotropy in the receiver function data. The SNRT analyses of the anisotropic models all show that SNR computed from stacks of T receiver functions after the waveform polarity been corrected, σ_{N2} linearly increases with $N^{1/2}$, and stacks of R receiver functions after removal of anisotropy always have higher SNR than those from original data ($\sigma_{N6}>\sigma_{N5}$). The three individual plus the joint measurements of seismic anisotropy and the SNRT analysis should be considered as one integrated technique which provides a robust and reliable way for identifying and estimating crustal anisotropy with receiver function data.

The joint analysis is designed to constrain a special type of seismic anisotropy in earth's crust, azimuthal anisotropy using receiver function data. When radially polarized S waves propagate through such an anisotropic crust, their energy splits and part of it is projected onto the transverse component. The birefringent T waveforms are proportional to the time derivative of those on the R component. In addition, the amplitude and the arrival time of the birefringent S waves exhibit a four-lobe variation pattern along the back azimuth direction. We found that these two unique features of azimuthal anisotropy provide a strong base for resolving it from other heterogeneous structures, such as velocity heterogeneities in the crust and a tilted crust-mantle boundary, which were demonstrated in our synthetic tests.

It should be noted that the anisotropic structure within Earth's crust is likely to be more complicated. In addition to azimuthal anisotropy with a horizontal symmetry axis, there are other types of anisotropic structures that are not addressed in this study. Many studies (e.g., Levin et al., 2008) have shown that an inclination of the symmetry axis leads to a mix of $\cos\theta$ and $\cos2\theta$ directional variation. If this is the case, then our measurements can be considered as the horizontal projection of the 3D anisotropic structure. Meanwhile, P-wave anisotropy in the crust can also cause directional variations in receiver function data by affecting the traveltime of the primary P wave. The induced back-azimuthal variation is, however, different from the $\cos2\theta$ change caused by azimuthal anisotropy, and thus should not be misinterpreted by the joint analysis. It should be also noted that the estimated seismic anisotropy here reflects the integrated anisotropic structure across the entire crust, as the joint analysis was only applied to the Moho Ps conversion phase. Although we have used homogenous anisotropic models in our

synthetic tests, the analysis can be used to estimate azimuthal anisotropy that has an uneven distribution with depth.

We applied the integrated analysis to two permanent stations in western China. The station located in the northern edge of the Tibetan plateau shows significant seismic anisotropy within the crust while the other one located inside the Sichuan basin exhibited little to no seismic anisotropy. The results here agree with the surface deformation and probably reflect deformation occurring within the lower crust. The relative large splitting time (δt=0.5s) observed in the Tibetan crust suggests that crustal contribution needs to be considered in interpreting SKS measurement in regions like Tibet where a thick crust is present. The same analysis can be applied to any stations with relatively good back azimuthal coverage to study crustal anisotropy and to understand crustal deformation.

Chapter 3

Effective acoustic wave extrapolation via optimum stencil

Abstract

A cost-effective waveform modeling is the key issue in reverse time migration (RTM) and full-waveform inversion (FWI). We develop an effective wave extrapolation (EWE) method to efficiently model wave propagation in acoustic media with high temporal accuracy. We start from the acoustic wave equation and obtain a 2^{nd} order time marching scheme in wavenumber domain. Then we formulate an explicit wave extrapolation scheme by approximating the cosine function in the Fourier integral. The errors in wave extrapolation are minimized by a set of optimum stencil with least-square coefficients. Benefiting from the accurate temporal extrapolation, the EWE method can achieve high accuracy with large time steps allowed by the Von Neumann stability condition. Our synthetic tests show that the EWE method possesses accuracy much higher than the 2^{nd} order temporal finite-difference (FD) method with the same time steps. The allowance of using large time steps makes the EWE method more efficient than the conventional FD method in order to achieve the same numerical accuracy. In our 2D homogenous case, the EWE method requires only ~25% of the computations used in the FD modeling. We implement the EWE method in RTM and obtain a high fidelity image of the input BP 2004 model, suggesting that EWE can be widely used in reverse time migration and full-wave inversion.

3.1. Introduction

Reverse time migration (RTM) (Baysal et al., 1983, McMechan, 1983, Whitmore, 1983) cross-correlates forward and backward wavefields to image complex seismic structures. Full-

waveform inversion (FWI) (Tarantola, 1984) is used to build high-resolution velocity models by fitting waveform data. Both RTM and FWI take advantage of the full wave in constraining seismic image and velocity model, respectively. Although these waveform-based approaches seem to be the ultimate solutions of seismic imaging problems, the required high computational cost prevents them from being pervasively used nowadays.

To model full-wave propagation in heterogeneous media, numerical methods such as finite-difference, pseudo-spectral and finite-element methods are often used (Carcione et al., 2002). The finite-difference (FD) approach is perhaps the most common modeling method employed in the current implementations of RTM and FWI. The FD method approximates spatial and temporal derivatives in the wave equation by Taylor series expansions. Although the temporal derivative can be approximated with high order terms (Etgen, 1986, Dablain, 1986), second order scheme is often favored since including higher order terms in time can significantly increase memory cost. As a result, the FD method often suffers from low temporal accuracy, and needs time steps much smaller than the von Neumann stability requirement. Spectral methods (Tal-Ezer et al, 1987, Etgen, 1989) are developed to increase temporal accuracy. Nevertheless, the computational cost of the Fourier transforms in each time step is expensive.

In principle, modeling the spatiotemporal evolution of a wavefield can be considered as an extrapolation in the time direction. In acoustic media, the temporal extrapolation can be formulated analytically by an integral of the product of the current wavefield and a cosine function in wavenumber domain, known as the Fourier integral (e.g., Soubaras and Zhang, 2008; Song and Fomel, 2011). Various techniques have been proposed to solve the Fourier

integral numerically. Soubaras and Zhang (2008) first proposed to approximate the cosine function in the Fourier integral by a polynomial, resulting in a two-step explicit marching scheme that allows large extrapolation steps. Zhang and Zhang (2009) further introduced a complex wavefield and suggested a one-step extrapolation by using multiple times of fast Fourier transforms (FFT). Song and Fomel (2011) developed a Fourier finite-difference method to better handle variable velocity with one FFT pair in each time step. Fomel et al. (2012) proposed a more inclusive seismic lowrank wave extrapolation method that uses a small set of representative spatial locations and wavenumbers to approximate the integral with a small number of FFT.

Here, we develop an effective wave extrapolation (EWE) method to achieve high temporal accuracy in acoustic media without Fourier transform. We formulate an explicit wave extrapolation scheme by approximating the cosine function in the Fourier integral with a weighted summation of base functions taken at a compact set of grids. The shape and the weighting coefficients are determined by minimizing the misfit between the cosine function and the summation. It allows us to achieve high accuracy and efficiency with no expensive FFT calculations. We will first present the theory, and then discuss its efficiency using a comparison with a regular finite-frequency method. The effectiveness of the proposed EWE method is further demonstrated by examples of synthetic modeling and an RTM implementation.

3.2. Method

3.2.1. Formulation of the problem

We start from the acoustic-wave equation in the time-space domain:

$$\frac{\partial^2 p(\mathbf{x},t)}{\partial t^2} = v(\mathbf{x})^2 \nabla^2 p(\mathbf{x},t), \tag{3.1}$$

where $p(\boldsymbol{x},t)$ is the pressure field and $v(\boldsymbol{x})$ is seismic velocity. Assuming a constant velocity v, the acoustic-wave equation (3.1) can be written in wavenumber domain:

$$\frac{d^2 \tilde{p}(\mathbf{k},t)}{dt^2} = v^2 |\mathbf{k}|^2 \tilde{p}(\mathbf{k},t), \tag{3.2}$$

with a spatial Fourier transform:

$$\tilde{p}(\mathbf{k},t) = \int_{-\infty}^{+\infty} p(\mathbf{x},t) e^{i\mathbf{k}\cdot\mathbf{x}} d\mathbf{x}. \tag{3.3}$$

Equation (3.2) has analytical solutions at an arbitrary time:

$$\tilde{p}(\mathbf{k},t) = e^{\pm i|k|vt}. \tag{3.4}$$

Therefore, the temporal extrapolation in wavenumber domain is accurate:

$$\tilde{p}(\mathbf{k},t \pm \Delta t) = e^{\pm i|\mathbf{k}|v(t\pm\Delta t)} = e^{\pm i|\mathbf{k}|v(\pm\Delta t)} \tilde{p}(\mathbf{k},t). \tag{3.5}$$

We combine the wave extrapolation from t-Δt to t and from t to t+Δt:

$$\tilde{p}(\mathbf{k},t+\Delta t) + \tilde{p}(\mathbf{k},t-\Delta t) = 2\cos(|\mathbf{k}|v\Delta t)\tilde{p}(\mathbf{k},t). \tag{3.6}$$

After applying an inverse spatial Fourier transform, the wavefield at $t+\Delta t$ can be expressed as:

$$p(\mathbf{x},t+\Delta t) = -p(\mathbf{x},t-\Delta t) + 2\int_{-\infty}^{+\infty} \cos(|\mathbf{k}|v\Delta t)\tilde{p}(\mathbf{k},t) e^{-i\mathbf{k}\cdot\mathbf{x}} d\mathbf{k}. \tag{3.7}$$

If the velocity is not constant, the wavefield can be approximated by replacing the constant velocity v with local velocity $v(\boldsymbol{x})$:

$$p(\mathbf{x},t+\Delta t) = -p(\mathbf{x},t-\Delta t) + 2\int_{-\infty}^{+\infty} \cos(|\mathbf{k}|v(\mathbf{x})\Delta t)\tilde{p}(\mathbf{k},t) e^{-i\mathbf{k}\cdot\mathbf{x}} d\mathbf{k}. \tag{3.8}$$

It should be emphasized here that although equation (3.8) appears as a 2nd order explicit extrapolation similar to a regular FD method, there is no differential approximation in time as

FD does so that the accuracy of the temporal extrapolation is not necessarily subjected to the choice of time step. Etgen (1989) first pointed out that it is not necessary to implement the Fourier integral using a finite-difference approximation and one can achieve better accuracy with an accurate-time-update pseudospectrum approach. Such an approach, however, has very high computational cost, making it difficult to be implemented in practical term. As mentioned above all the other approaches (Soubaras and Zhang, 2008; Zhang and Zhang, 2009; Song and Fomel, 2011; Fomel et al., 2011) so far involve Fourier transforms, which are not intended in this study. We want to re-formulate equation (3.8) into an explicit wave extrapolation scheme using values at a set of grid points (stencil):

$$p(\mathbf{x},t+\Delta t) = -p(\mathbf{x},t-\Delta t) + \sum_{m=1}^{N_s} C(\mathbf{x},\Delta\mathbf{x}_m)\, p(\mathbf{x}+\Delta\mathbf{x}_m,t) + E(\mathbf{x},t), \tag{3.9}$$

where m is the grid index, $\Delta\boldsymbol{x}_m$ is the location difference between grid m and the target location $\boldsymbol{x}$, $C(\boldsymbol{x},\Delta\boldsymbol{x}_m)$ is the weighting coefficient at each stencil point, N_s is the total number of points in stencil and $E(\boldsymbol{x},t)$ is the error in the approximation of the Fourier integral with a stencil grid summation. If we choose an origin symmetric stencil around $\boldsymbol{x}$, and use the property of Fourier transform, equation (3.9) becomes:

$$\begin{aligned} p(\mathbf{x},t+\Delta t) &= -p(\mathbf{x},t-\Delta t) + \sum_{m=1}^{M} C(\mathbf{x},\Delta\mathbf{x}_m) \int (e^{-i\mathbf{k}\cdot(\mathbf{x}+\Delta\mathbf{x}_m)} + e^{-i\mathbf{k}\cdot(\mathbf{x}-\Delta\mathbf{x}_m)})\tilde{p}(\mathbf{k},t)d\mathbf{k} + E(\mathbf{x},t) \\ &= -p(\mathbf{x},t-\Delta t) + \sum_{m=1}^{M} C(\mathbf{x},\Delta\mathbf{x}_m) \int 2\cos(\mathbf{k}\cdot\Delta\mathbf{x}_m)\tilde{p}(\mathbf{k},t)e^{-i\mathbf{k}\cdot\mathbf{x}}d\mathbf{k} + E(\mathbf{x},t) \\ &= -p(\mathbf{x},t-\Delta t) + \int \left(\sum_{m=1}^{M} 2\cdot C(\mathbf{x},\Delta\mathbf{x}_m)\cdot\cos(\mathbf{k}\cdot\Delta\mathbf{x}_m) \right) \tilde{p}(\mathbf{k},t)e^{-i\mathbf{k}\cdot\mathbf{x}}d\mathbf{k} + E(\mathbf{x},t). \end{aligned} \tag{3.10}$$

Here, $M=(Ns+1)/2$ is the number of independent grids in an origin symmetric stencil. If we further represent the error term as a spatial convolution of $p(\boldsymbol{x},t)$ and $E(\boldsymbol{x})$:

$$E(\mathbf{x},t) = 2p(\mathbf{x},t) * E(\mathbf{x}) = \int 2\tilde{p}(\mathbf{k},t)E(\mathbf{k})e^{-i\mathbf{k}\cdot\mathbf{x}}d\mathbf{k}, \tag{3.11}$$

where $E(\boldsymbol{k})$ is the misfit at wavenumber $\boldsymbol{k}$. Comparing equation (3.8) with equations (3.10) and (3.11), we find that the cosine function in equation (3.8) can be written as:

$$\cos(|\mathbf{k}|v(\mathbf{x})\Delta t) = \sum_{m=1}^{M} C(\mathbf{x},\Delta\mathbf{x}_m)\cdot\cos(\mathbf{k}\cdot\Delta\mathbf{x}_m) + E(\mathbf{k}). \tag{3.12}$$

We have re-formulated the accurate temporal extrapolation equation (3.8) into an explicit wave extrapolation scheme equation (3.9), in which the cosine function is approximated by a weighted summation of cosine functions evaluated at stencil grids, as shown in equation (3.12). The extrapolation error at each time step, $E(\boldsymbol{x},t)$, is explicitly related to the error in fitting the cosine-function at all wavenumbers, $E(\boldsymbol{k})$. Thus, the accuracy of the temporal extrapolation is solely determined by the fitting of the cosine function at each wavenumber. For a given velocity field and spatial discretization, the cosine function fitting is controlled by the selection of grid distribution (stencil shape), $\Delta\boldsymbol{x}_m$, and the corresponding coefficients, $C(\boldsymbol{x},\Delta\boldsymbol{x}_m)$, at each spatial location.

3.2.2. Optimum stencil and coefficients

For any given stencils, we seek for coefficients that minimize the error in wavenumber domain, $E(\boldsymbol{k})$. This is a typical optimization problem that can be achieved by minimizing the L2 norm of the error:

$$\min(\|E(\mathbf{k})\|_2) = \min(\left\|\cos(|\mathbf{k}|v(\mathbf{x})\Delta t) - \sum_{m=1}^{M} C(\mathbf{x},\Delta\mathbf{x}_\mathbf{m})\cdot\cos(\mathbf{k}\cdot\Delta\mathbf{x}_\mathbf{m})\right\|_2). \tag{3.13}$$

More specifically speaking, the coefficients at each spatial location $\boldsymbol{x}_0$ can be obtained by a vector-matrix inverse problem:

$$\begin{bmatrix} C(\mathbf{x}_0,\Delta\mathbf{x}_1) \\ C(\mathbf{x}_0,\Delta\mathbf{x}_1) \\ \cdots \\ C(\mathbf{x}_0,\Delta\mathbf{x}_M) \end{bmatrix} = inv\Bigg(\begin{bmatrix} \cos(\mathbf{k}_1\cdot\Delta\mathbf{x}_1) & \cos(\mathbf{k}_1\cdot\Delta\mathbf{x}_2) & \cdots & \cos(\mathbf{k}_1\cdot\Delta\mathbf{x}_M) \\ \cos(\mathbf{k}_2\cdot\Delta\mathbf{x}_1) & \cos(\mathbf{k}_2\cdot\Delta\mathbf{x}_2) & \cdots & \cos(\mathbf{k}_1\cdot\Delta\mathbf{x}_M) \\ \cdots & \cdots & \cdots & \cdots \\ \cos(\mathbf{k}_{N_k}\cdot\Delta\mathbf{x}_1) & \cos(\mathbf{k}_{N_k}\cdot\Delta\mathbf{x}_2) & \cdots & \cos(\mathbf{k}_{N_x}\cdot\Delta\mathbf{x}_M) \end{bmatrix} \Bigg) \begin{bmatrix} \cos(|\mathbf{k}_1|v(\mathbf{x}_0)\Delta t \\ \cos(|\mathbf{k}_2|v(\mathbf{x}_0)\Delta t \\ \cdots \\ \cos(|\mathbf{k}_{N_k}|v(\mathbf{x}_0)\Delta t \end{bmatrix}, \quad (3.14)$$

where the "inv" represents pseudo-inverse that can be solved by QR factorization and N_k is the number of wavenumbers that typically equals N_x.

On the other hand, we seek for a stencil that balances the accuracy and efficiency. Let the grid spacing to be h, and define $\gamma=(v\Delta t)/h$, the cosine-fitting problem (3.12) can be characterized by a scalar problem:

$$\cos(\gamma h|\mathbf{k}|) \approx c_0 + \sum_{i=i}^{N_a} c_i \cos(n_i h|\mathbf{k}|) + \sum_{j=1}^{N_o} c_j \cos(r_j h|\mathbf{k}|), \quad (3.15)$$

where n_i and r_j are integers and real numbers (>1) associated with the axial and off-axial stencil points, respectively; c_i and c_j are the corresponding coefficients (c_0 is the coefficient of the central point); N_a and N_o are the half total numbers of the axial (except for the central point) and off-axial points, respectively.

The conventional FD method is a special case of wave extrapolation, which has only axial stencil points (N_o=0) and uses finite-difference approximation to solve the coefficients. The L^{th} order FD has L stencil points in each spatial dimension besides the central point, which makes $N_s=nL+1$ (Figure 3.1a), where n is the medium dimension. Dai et al. (2012) computed the least-square coefficients of the FD stencil, which we refer as the "optimized finite-difference" (OFD)

method. We first compare the OFD method with the conventional FD method. We set N_a=8 and N_o=*0* and compare the misfits in fitting the cosine function (Figure 3.2a and 3.2b) using the same base functions but different coefficients corresponding to OFD and FD method, respectively. Overall, the OFD shows a better fitting to the cosine function than the FD does. However, for small wavenumbers, the OFD exhibits large oscillations that are not desirable. As mentioned above, the off-axial stencil points usually have a central distance being non-integer multiple (r_j) of h. For instance, we set N_a=8, N_o=2, $r_1 = r_2 = \sqrt{2}$ and solve the corresponding least-square coefficients. The corresponding cosine function curve (Figure 3.2a) and misfits (Figure 3.2b) are compared with those of the FD and OFD. Obviously, the additional base function significantly reduces the misfit of the cosine function. Next, we optimize the choice of the additional base functions by analyzing the dependence of misfit on distance number, r. It appears that the misfit at all wavenumbers shows an increase with increasing r (Figure 3.2c). As mentioned above the distance number, r, of the off-axial points is always great than 1. On the other hand, the Von Neumann stability condition for explicit wave extrapolation is:

$$\Delta t < \frac{\min(\Delta \mathbf{x}_m)}{\sqrt{n} \cdot \max(v(\mathbf{x}))}, \tag{3.16}$$

which ensures $\gamma < \frac{1}{\sqrt{n}} \le 1$. As a result, it is never possible to choose a distance number r_j=γ. A stencil that includes off-axial points being closest to its center thus appears to be the optimum selection (Figure 3.1b).

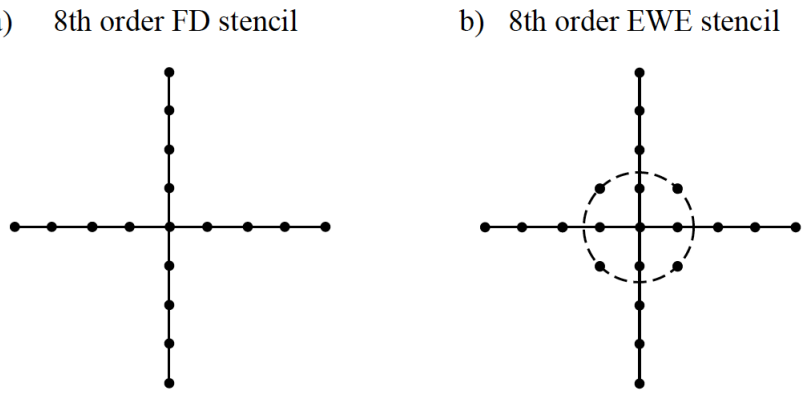

Figure 3.1. 8th order a) finite difference and b) optimum stencils in 2D. The 2D optimum stencil has a crosshair shape with off-axial points.

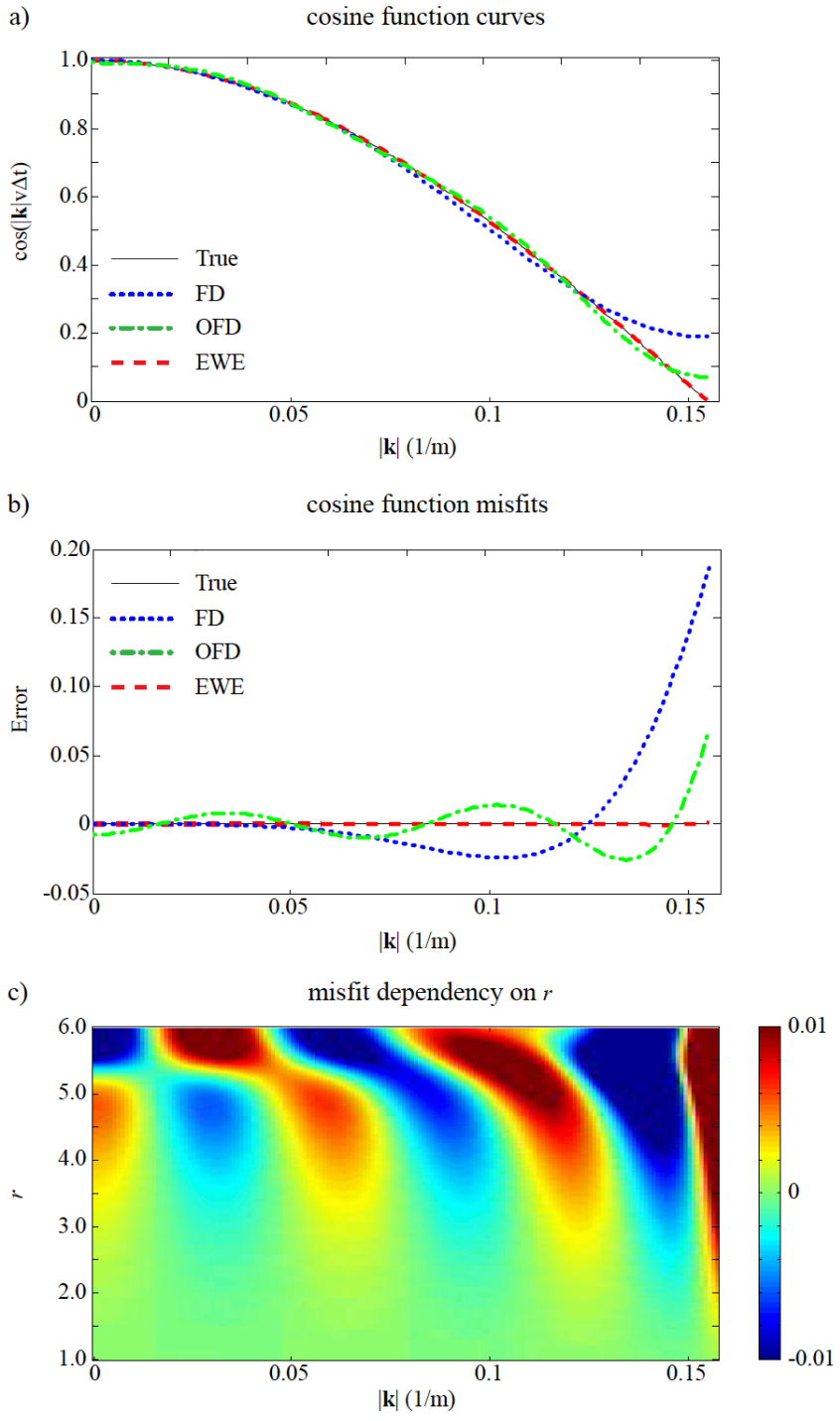

Figure 3.2. a) Fittings of the cosine function in equation (3.13) using base functions corresponding to finite-difference (FD), optimized finite-difference (OFD) and effective wave extrapolation (EWE) methods and b) misfits of them (true: black solid line, FD: blue dotted

line, OFD: green dash-dot line, EWE: red dashed line). The parameters are: v=2000 m/s, Δt=5 ms, h=20 m and N_a=8, N_o=2. c) The misfit dependency on r.

To summarize, in fitting the cosine function in equation (3.15), we have shown that 1) adding non-integer r can significantly reduce the misfit and 2) smaller r is more effective in reducing fitting error. In 2D and 3D problems, including off-axial stencil points with minimal distances to the center (Figure 3.1b) can effectively reduce the fitting error in equation (3.12) (see NUMERICAL EXAMPLES). We refer the method with optimized stencil and corresponding least-square coefficients as the "effective wave extrapolation" (EWE) method.

3.2.3. Improvement of efficiency in computing the EWE coefficients

All the EWE coefficients can be computed by solving the inverse problem (3.14) across the space. The computational complexity of QR decomposition in solving the least-square problem is $O(N_s^2 \cdot N_x)$, where N_s and N_x are the number of stencil points and the number of grid points in space, respectively. As a result, the total cost becomes $O(N_s^2 \cdot N_x^2)$, which is expensive in large 2D and 3D problems. We find an efficient approach to reduce the cost in computing the EWE coefficients.

First, we degenerate the inverse problem (3.14) by using only a few of representative wavenumbers. In equation (3.14), the target function and the base functions are a cosine dome (Figure 3.3a) and cosine cylinders (Figure 3.3b-d), respectively. Due to the smoothness of the cosine functions, it is not efficient to do the fit at every wavenumber. If we resample the wavenumber using N_{k_i} representative wavenumbers in each dimension, the total wavenumbers

are reduced to $N_{k_i}{}^n$. As a result, the computational cost is reduced to $O(N_s{}^2 \cdot N_{k_i}{}^n)$, and it also becomes independent of spatial discretization. In an L^{th} order EWE scheme, the definition range of the target and base cosine functions is bounded by:

$$|\mathbf{k}|v\Delta t < |\mathbf{k}\|\Delta\mathbf{x}_m| <= \left|\max(\mathbf{k}) \cdot (\frac{L}{2}h)\right| < \frac{L}{4} \tag{17}$$

Therefore, the maximum re-sampling interval is upper-bounded by $\frac{\frac{L}{2}+1}{N_{k_i}}$ in each dimension. For instance, if we set the sampling interval of dimensionless variable $|\mathbf{k}\|\Delta\mathbf{x}_m|$ in the cosine function as 0.1 in a 2D problem and use 8th order scheme, the amount of representative wavenumbers is $N_{k_i}{}^2 = 50^2 = 2500$.

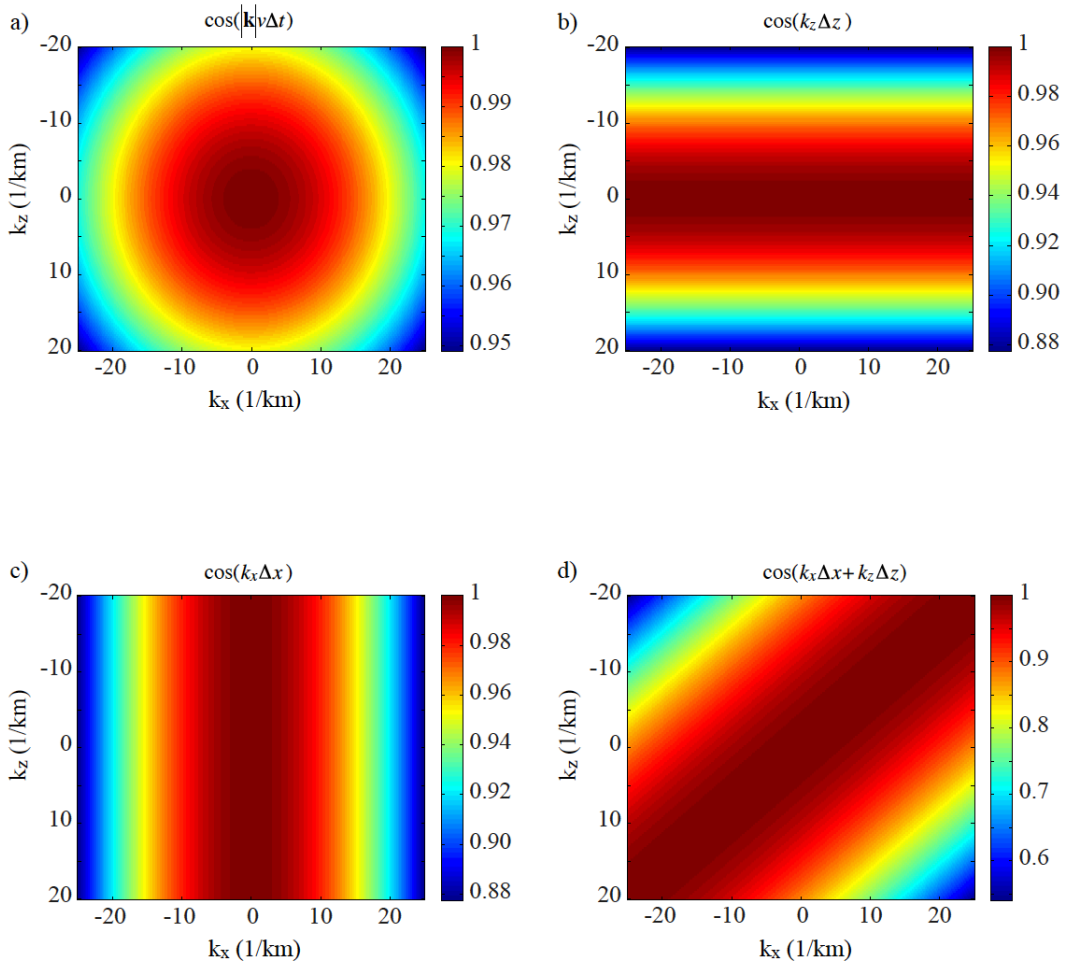

Figure 3.3. Shape of the cosine functions in equation (3.11): a) the target function, b) a base function corresponding to a stencil point on z axis, c) a base function corresponding to a stencil point on x axis and d) a base function corresponding to an off-axial stencil point. The parameters are: v=2000 m/s, Δt=5 ms, Δx=20 m and Δz=25 m.

Second, we reduce the number of times in solving the inverse problem (3.14). In an isotropic heterogeneous medium, the locations with the same velocity have the same coefficients. Thus, it is only necessary to solve (3.14) for N_v times, where N_v is the number of distinct velocities. Practically, the number of distinct velocities can be further reduced by discretizing the velocities

based on a specified velocity increment that can be related to uncertainties in the velocity model. If we intend to control the inaccuracy under the uncertainty level in a velocity model, it only requires computing EWE coefficients on velocities with an interval twice of the uncertainty. For instance, if the uncertainty is 2 m/s in a velocity model that has a minimum velocity of 1500 m/s and a maximum velocity of 5500 m/s, it only requires computing EWE coefficients at every 4m/s. In such a case, N_v is reduced to 10^3 while the inaccuracy in velocity is <0.2%.

By choosing representative wavenumbers and computing EWE coefficients at distinct velocities, the total computational cost in solving the EWE coefficients is reduced to $O(N_s^2 \cdot N_{ki}^n \cdot N_v)$. Notably, it is usually negligible compared to the propagation cost $O(N_s \cdot N_x \cdot N_t)$, where N_t is the number of time steps.

3.2.4. Cost in wave extrapolation

In explicit wave extrapolation, the computational cost for one time step is approximately proportional to the number of stencil points. With minimal distance points, the EWE stencil has $N_s = n(L+2n-2)+1$ for 2D and 3D problems. The extra cost of EWE is $\sim\frac{2(n-1)}{L}$ (e.g. ~25% for 8th order 2D problem) of that of FD.

Although the EWE method is slightly more expensive than the FD method for each time step, its overall computational cost is less if compared with a FD method with same accuracy. In the second order temporal FD method, a time step much smaller than the stability limitation is often

used to preserve waveform accuracy after iterating large number of time steps. On the other hand, the EWE method tolerates larger time step due to its high temporal accuracy. In the following numerical examples, we show the accuracy of the EWE method is comparable to the FD method with a much finer time step.

3.3. Numerical examples

3.3.1. Performance of the EWE method

We first demonstrate the advantages of the EWE method in a 2D homogenous velocity model. The velocity model and the source-receiver geometry are shown in Figure 3.4. A Ricker wavelet with a central frequency of 10 Hz (with max frequency of 35 Hz) is used as a pressure source. The grid spacing in x and z directions are 20 m and 25 m, respectively. An 8^{th} order scheme is applied to suppress spatial dispersion. We use an absorbing boundary (Clayton and Engquist, 1977) to suppress the reflections from the boundaries.

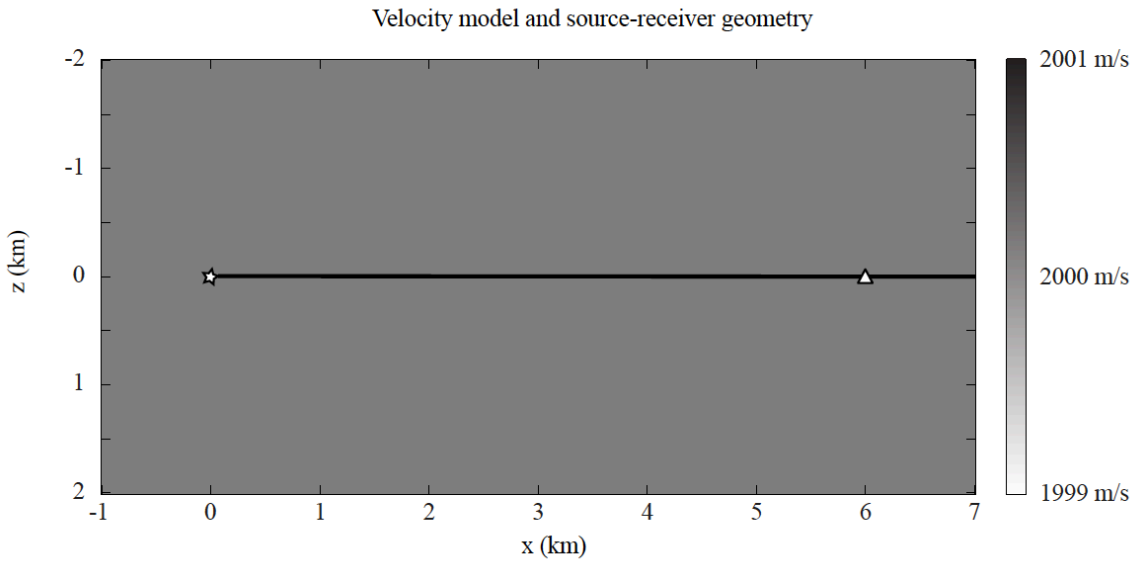

Figure 3.4. Velocity model and source-receiver geometry. The source (star) is located at x=0 m, z=0 m and the receivers are located along the x direction (black line) with a spacing of 20 m. A near-offset receiver is located and x=20 m and a far-offset receiver (triangle) is located at x=6000 m.

In waveform modeling, we are interested in the accuracy of synthetic waveforms. To obtain a reference waveform, we assume the waveform is fairly accurate when the time sampling rate is small enough. We modeled FD and EWE waveforms with a fairly small time step of 0.5 ms. The errors in the cosine functions for FD method (Figure 3.5a) and EWE method (Figure 3.5b) are small ($<10^{-7}$) and their waveform differences (Figure 3.5c) are negligible. The negligible differences confirm that both methods are accurate enough when time step is small. We choose FD waveforms with Δt=0.5 ms as the reference waveforms.

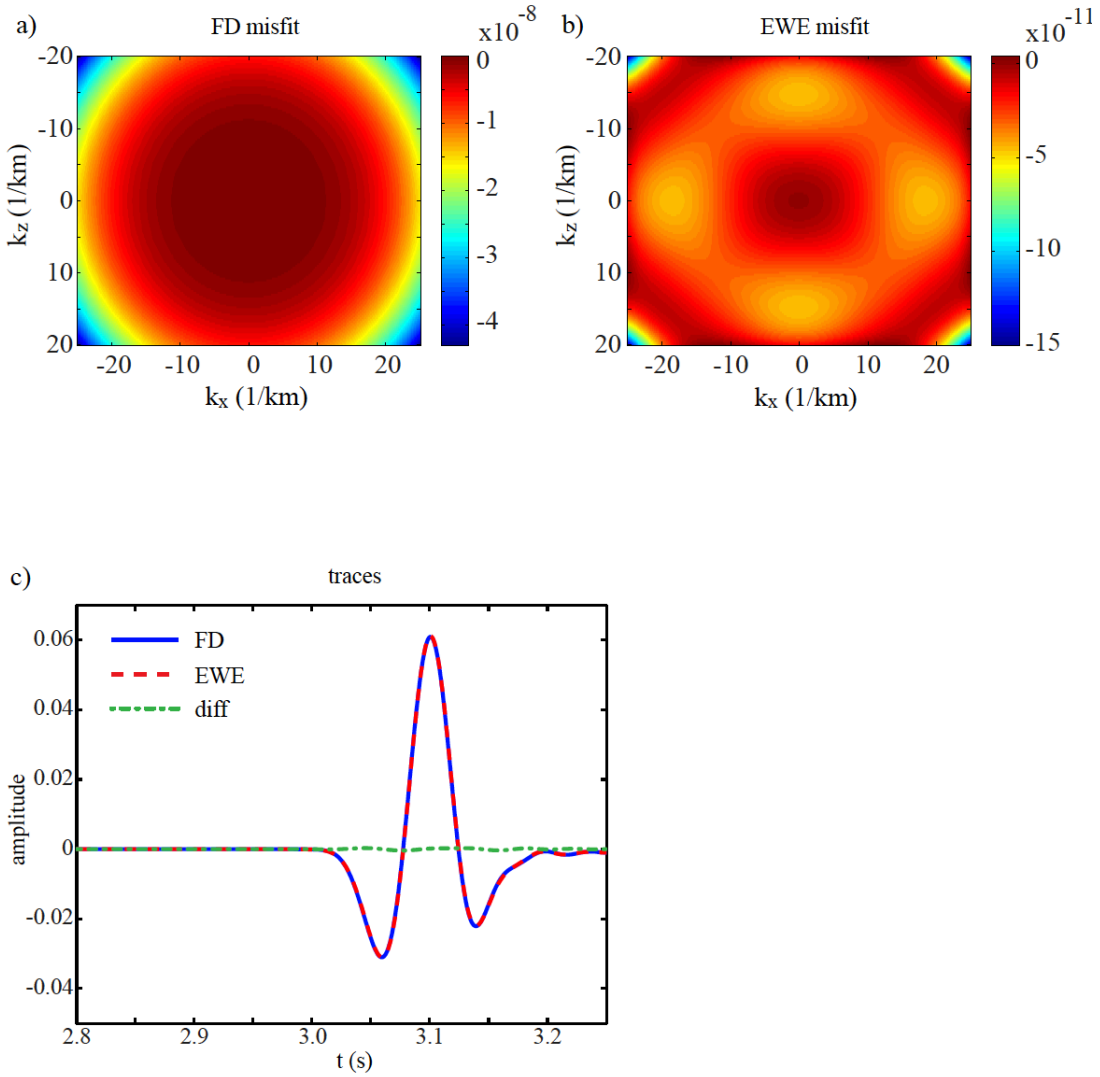

Figure 3.5. a) Misfits in the cosine function approximation using FD and b) EWE with small Δt=0.5 ms. c) Reference waveforms of FD (blue solid line), EWE (red dashed line) and their differences (green dash-dot line).

The misfit in approximating the cosine function is the key factor that controls the accuracy of the wave extrapolation. Because the FD method can be treated as a special case of wave extrapolation, the errors in its cosine function can be used as an indicator of its accuracy as well.

We compute the errors in of the cosine function of both the FD method (Figure 3.6a) and the EWE method (Figure 3.6b) with Δt=5 ms. Errors of the FD method are generally more than 100 times larger than those of the EWE method. As we mentioned in the METHODS, we can efficiently compute the EWE coefficients by selecting representative wavenumbers. Here, with $N_{k_x} = N_{k_z} = 41$ in computing the coefficients, the errors in the cosine function fitting (Figure 3.6d) are comparable to those computed with full wavenumbers (Figure 3.6b). We model FD and EWE waveforms and compare them with the reference waveform. Although the shot gathers using the FD and the EWE methods appear to be similar (Figure 3.7a and 3.7b), the errors of the EWE method are much less than those of the FD method (Figure 3.7c and 3.7d). Notably, the inaccuracy of the FD synthetics increases significantly through time (Figure 3.7c), which is not seen in the EWE synthetics (Figure 3.7d). At the near offset (Figure 3.8a), both the FD and EWE synthetics are close to the reference. Their peak traveltime deviations from the reference are less than a tenth of the sampling interval. At the far offset (Figure 3.8b), the waveform of the FD method is significantly distorted but the EWE waveform remains fairly accurate. The peak traveltime deviations of the FD and the EWE waveforms are -18.8 ms and 0.5 ms, respectively.

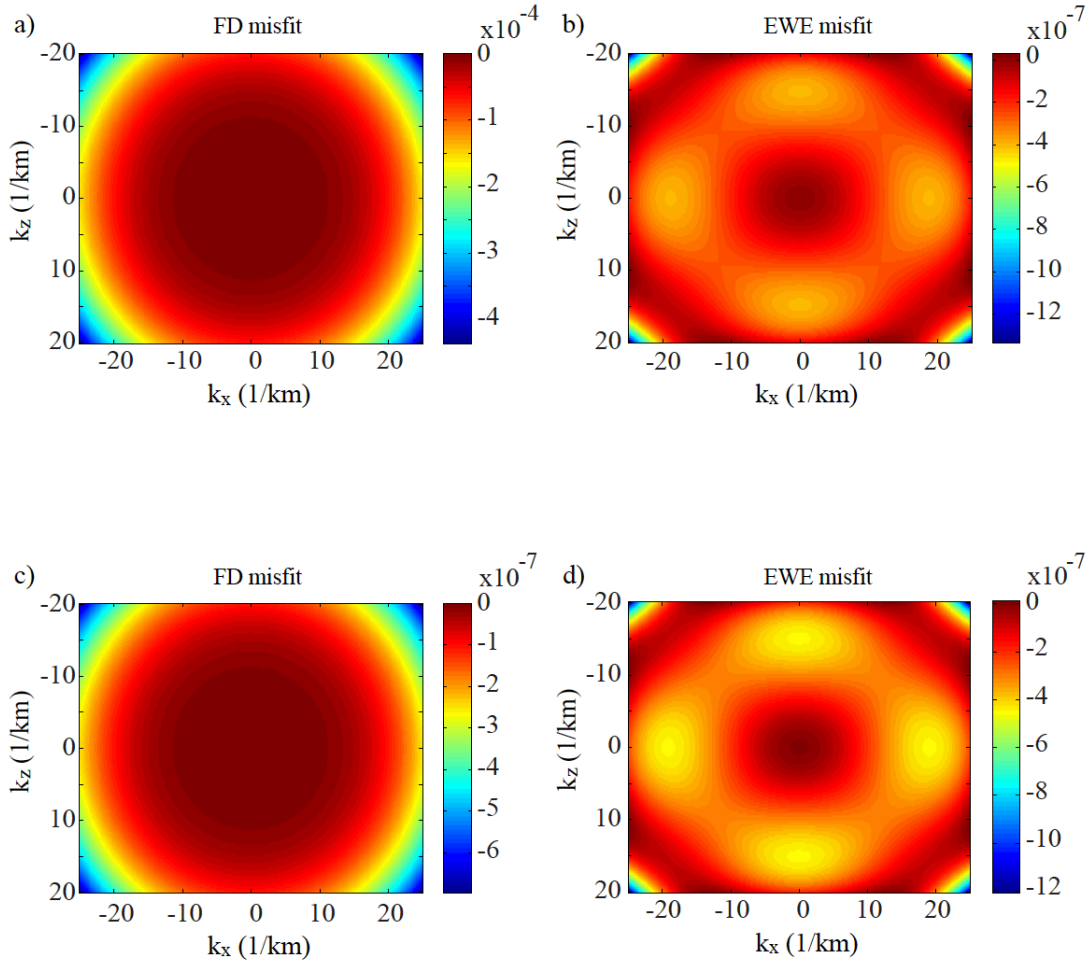

Figure 3.6. Misfits in the cosine function approximation using a) FD with Δt =5 ms, b) EWE with Δt=5 ms and all wavenumbers, c) FD with Δt =1 ms and d) the EWE with Δt =5 ms and only representative wavenumbers.

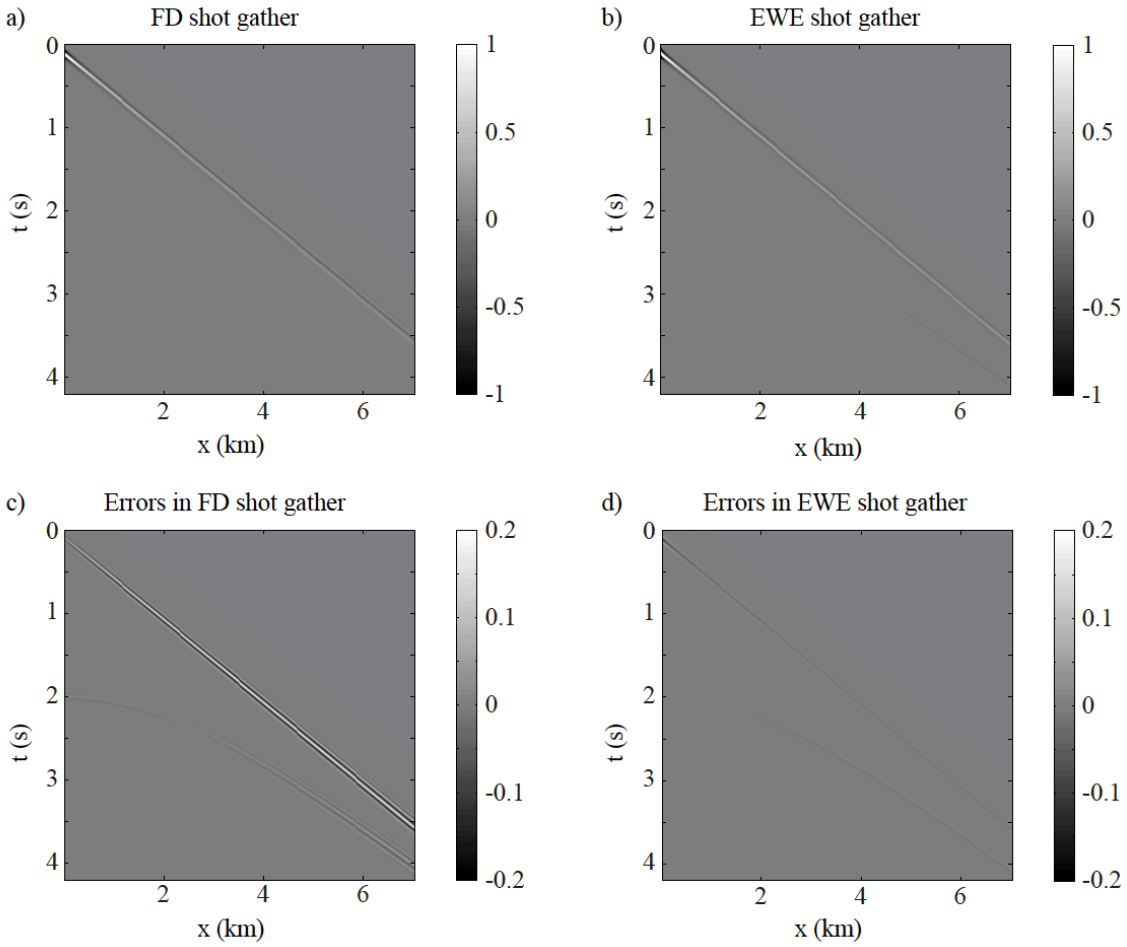

Figure 3.7. Shot gathers using a) FD and b) EWE methods with Δt =5 ms. c) The amplified differences between FD shot gather and the reference shot gather. d) The amplified differences between EWE shot gather and the reference shot gather. Note the errors increase with time for the FD method but remain small for the EWE method.

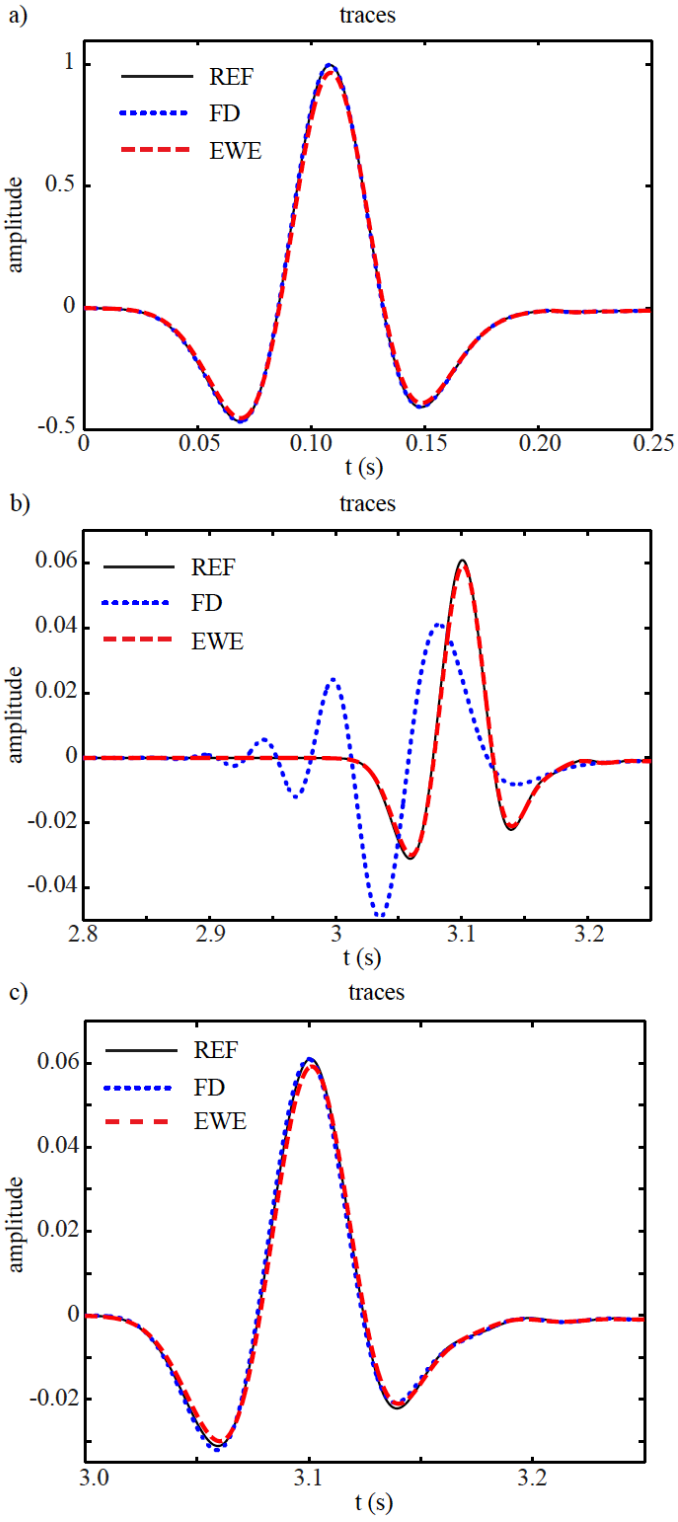

Figure 3.8. a) Comparison of waveforms at a near offset (x=20 m) and b) a far offset (x=6000 m). The reference waveform (black solid line) is computed by FD method with Δt =0.5 ms. The

FD waveform (blue dotted line) and EWE waveform (red dashed line) are computed with Δt =5 ms. c) FD waveform with Δt =1 ms (blue dotted line) and EWE waveform with Δt =5 ms (red dashed line).

In FD modeling, better fitting of the cosine function and higher accuracy of synthetics can be achieved by reducing the time step. We find that the cosine function can be fitted equally well using a time step Δt=1 ms in FD (Figure 3.6c), and Δt =5 ms (Figure 3.6d) in EWE, respectively. Their waveforms at the far offset are also comparable (Figure 3.8c) with peak traveltime deviations of -0.9 ms and 0.5 ms, respectively. In this case, the EWE needs only 20% of number of temporal extrapolations used in FD, although the EWE stencil requires ~23% more grid points than that of FD. Overall, the EWE requires only ~25% of the FD cost under similar accuracy.

3.3.2. The Marmousi model example

We select the Marmousi velocity model (Figure 3.9a) to test the accuracy of EWE waveforms in complex velocity model with sharp velocity discontinuities. The Marmousi model is re-sampled to spatial grids with 20 m interval in both x and z direction. In EWE modeling, we discretize the true velocity model with a 4m/s interval from 1500 m/s to 5500m/s and use 51 representative wavenumbers in each dimension. We insert a Ricker source (red star in Figure 3.9a) with a central frequency of 10 Hz (with a maximum frequency ~35 Hz) and select 8^{th} order EWE scheme to suppress spatial dispersion. We use Δt=2 ms that is smaller than the stability limitation of ~2.5 ms and propagate the EWE wave (Figure 3.9b) and FD wave. The reference waveform is computed using FD method with Δt=0.2 ms. The differences between EWE

waveform and the reference waveform are almost negligible (Figure 3.9c). On the other hand, the FD with Δt=2 ms has significant inaccuracy in waveform (Figure 3.9c). We further compare the misfit of the two methods in matching the true cosine function (Figure 3.10a). The misfits in the FD and EWE method are shown in Figure 3.10b and 3.10d, respectively. A comparison of the misfits on the same scale shows that the EWE misfits (Figure 3.10d) are always much smaller than the FD ones (Figure 3.10c).

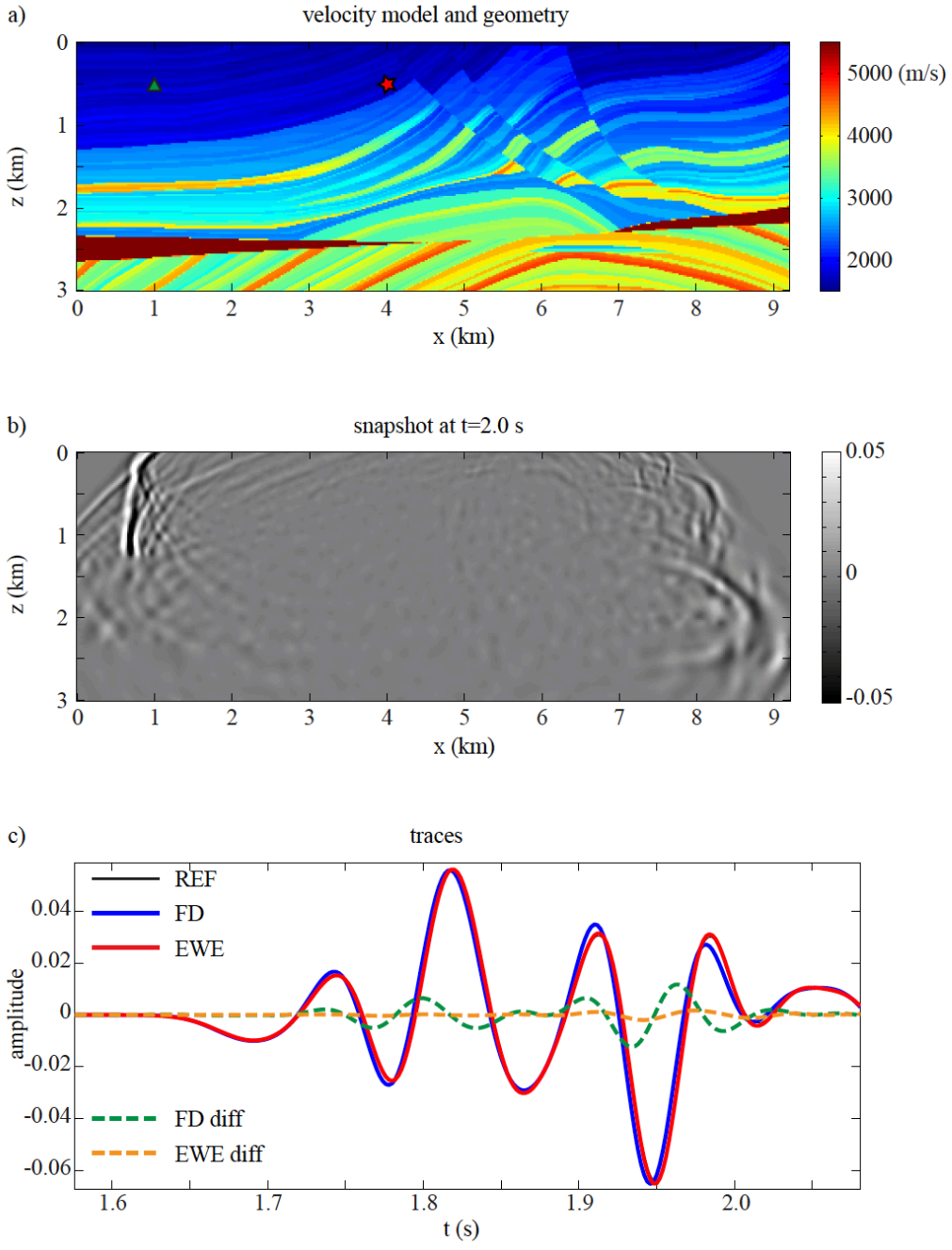

Figure 3.9. a) The Marmousi velocity model and source-receiver geometry. The source (red star) is located at x=4000 m and z=500 m and a receiver is located at x=1000 m and z=500 m. b) Snapshot of EWE wavefield at 2.0 s. c) Waveforms computed using the FD method, the EWE

method and their differences from the reference waveform at the receiver. Note that the EWE method has much smaller errors than the FD method.

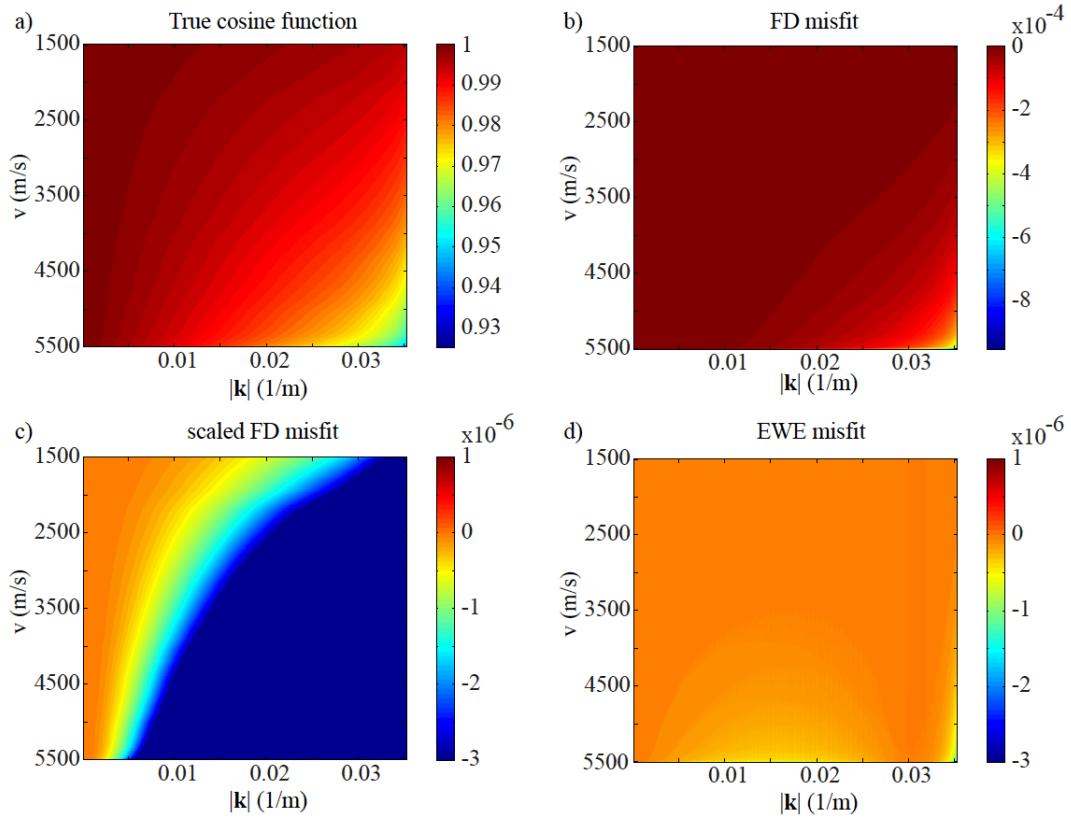

Figure 3.10. a) The true cosine function as a function of velocity and wavenumber. b) The misfit in the cosine function using FD method. c) The same as b) but scaled to compare with d) the misfit using EWE method. Note that the EWE method is more accurate than the FD method at all velocities and wavenumbers.

3.3.3. RTM image of the BP 2004 model using EWE

We implement the EWE method in reverse time migration and select BP 2004 model (Billette and Brandsberg-Dahl, 2005) to test its performance in RTM imaging. The BP dataset is a high quality synthetic dataset generated by FD method with shot and receiver spacing of 50 m and

12.5 m, respectively. In the migration, we use grid spacing of 6.25 m in both x and z direction and set a maximum frequency of 35 Hz. We choose an 8^{th} order EWE scheme to suppress the spatial dispersion and a time step of 0.652 ms that is slight below the stability limitation of ~0.92 ms. In EWE modeling, we discretize the velocity model to a 2 m/s interval and choose 403 and 201 representative wavenumbers in x and z direction, respectively. We use the true velocity model (Figure 3.11a) to reverse-time migrate the synthetic data and obtain a fairly well image (Figure 3.11b). The top and base salt reflectors are located correctly and the deep salt legs ~10 km in depth are imaged clearly. It suggests that EWE method is able to model waveforms at long traveltime correctly.

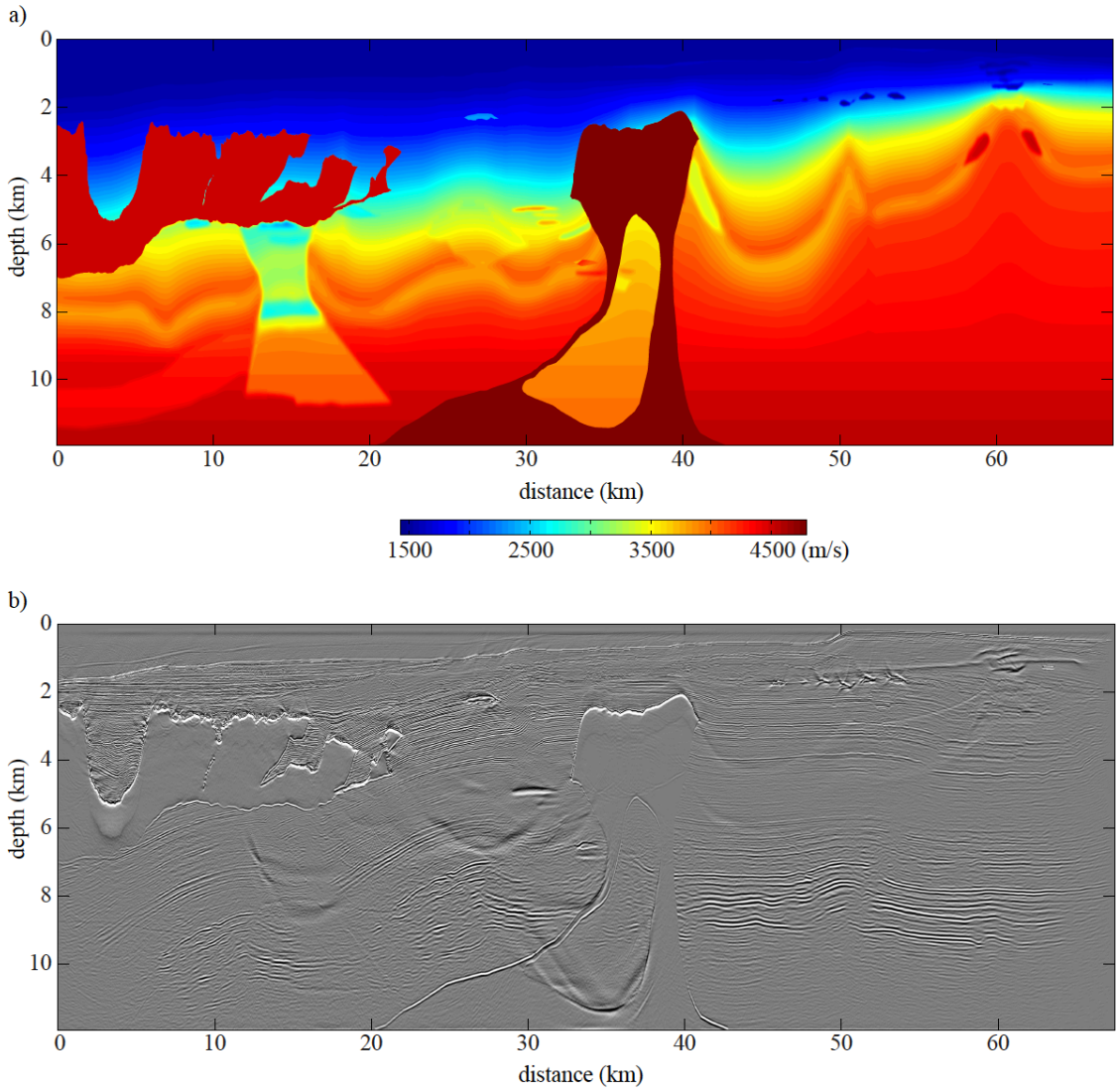

Figure 3.11. a) BP 2004 velocity model. B) The image of the velocity model in a) obtained by EWE reverse-time migration.

3.4. Discussion

In waveform modeling, large spatial sampling interval is always computationally appealing because it reduces the size of a given problem. Unfortunately, large spatial sampling interval may cause spatial dispersion for the same frequency content. Previous studies have shown that

the spatial dispersion can be suppressed by using 1) higher order finite-difference scheme (Dablain, 1986) or 2) full-size stencil in low-rank approximation (Fomel et al., 2012). In favor of minimal number of grid points in stencil, we choose to use stencils with extra axial points similar to the finite-difference scheme to handle spatial dispersion problem.

In principle, violation of the constant velocity assumption in deriving the Fourier integral may affect the accuracy of wave extrapolation. Zhang and Zhang (2009) found that wave oscillation might occur at sharp velocity boundaries using the one-step extrapolation. However, the EWE method does not require a constant velocity because its coefficients are obtained by a localized expansion (equation 3.14) similar to the FD method. The location dependent velocity, $v(\mathbf{x})$, is assumed constant only in deriving the extrapolation error (equation 3.11). As a result, we do not observe any oscillation at sharp velocity boundaries in our synthetic tests (Figure 3.9) and RTM images (Figure 3.11). Our tests have shown that the EWE method can handle large velocity contrast as well as the FD method.

The EWE method can be extended to transversely isotropic (TI) media by including the directional velocity (Alkhalifah, 1998). Under such an expression, the velocity and the wavenumbers can be substituted by isotropic velocity with anisotropic parameters ε and η (Thomsen, 1986) and wavenumbers in the principal directions of ansiotropy (Song and Fomel, 2011). In TI media, we expect that the EWE method can be conducted similarly by introducing extra parameters to the corresponding cosine-function fitting problem.

3.5. Conclusions

We presented an effective wave extrapolation method to model wave propagation in acoustic media. The EWE method effectively solves the accurate temporal extrapolation via optimum stencil and least-square coefficients. The compact shape of stencil ensures that the high temporal accuracy is achieved with minimal cost. The EWE method remains stable through time under the Von Neumann stability condition. Our synthetic examples show that 1) the EWE method is more accurate than the conventional FD method if similar time steps are employed, 2) the computational cost of the EWE method is much less than that of the conventional FD method under similar accuracy, and 3) high fidelity image can be obtained by implementing EWE method in reverse time migration. We suggest implementing the effective wave extrapolation method in reverse time migration and full-waveform inversion to maximize cost effectiveness.

Appendix A: Relationship between the maximum of the IOFs and delay time

In this appendix, we would like to show that the maximum of the three IOFs ($I_{r\cos}(\varphi,\delta t)$, $I_{rcc}(\varphi,\delta t)$, and $I_t^{-1}(\varphi,\delta t)$) can be expressed as 1+cδt^2, where c is a constant, i.e.,

$$I_{r\cos}(\varphi,\delta t) = 1 + c_1\delta t^2; \quad I_{rcc}(\varphi,\delta t) = 1 + c_2\delta t^2; \quad I_t(\varphi,\delta t) = 1/(1 + c_3\delta t^2). \tag{A.1}$$

To simplify the derivation of (A.1), here we assume that the Moho Ps conversion wave can be approximated by a half cosine function $\cos\omega_0(t - t_0)$, where ω_0 is dominant frequency and t_0 is the isotropic arrival time of the Moho converted phase. The R receiver function at back azimuth θ can be expressed as $\cos\omega_0(t - t_0 + \frac{\delta t}{2}\cos 2(\theta - \varphi))$, where φ is the fast polarization direction. The maximum stacking amplitude occurs at t= t_0, and is expected to be 1 after correction. Thus the first IOF can be computed from:

$$\begin{aligned}\max\{I_{r\cos}(\varphi,\delta t)\} &= 1\Big/\left(\frac{1}{2\pi}\int_0^{2\pi}\cos(\omega_0\tfrac{\delta t}{2}\cdot\cos 2(\theta-\varphi))\,d\theta\right)^2 \\ &\approx 1\Big/\left(\frac{1}{2\pi}\int_0^{2\pi}\{1-\tfrac{1}{2}\cdot[\tfrac{\omega_0\delta t}{2}\cdot\cos 2(\theta-\varphi)]^2\}\,d\theta\right)^2,\end{aligned} \tag{A.2a}$$

which is:

$$\max\{I_{r\cos}(\varphi,\delta t)\} \approx 1 + \frac{\omega_0^2}{8}\delta t^2. \tag{A.2b}$$

For a pair of R receiver functions with a time shift δt_i, the cross correlation ratio after and before anisotropic correction is:

$$
\begin{aligned}
I_{ricc} &= \int_{t_0-T_0/4}^{t_0+T_0/4} \cos^2\omega_0(t-t_0)dt \Big/ \int_{t_0-T_0/4}^{t_0+T_0/4} \cos\omega_0(t-t_0-\delta t_i)\cdot\cos\omega_0(t-t_0-\delta t_j)dt \\
&\approx \int_{-T_0/4}^{T_0/4} \cos^2\omega_0 t dt \Big/ \int_{-T_0/4}^{T_0/4} \cos^2\omega_0 t\cdot(1-\frac{\omega_0^2}{2}\cdot\delta t_i^2)\cdot(1-\frac{\omega_0^2}{2}\cdot\delta t_j^2)dt \\
&\approx 1+\frac{\omega_0^2}{2}\cdot\delta t_i^2+\frac{\omega_0^2}{2}\cdot\delta t_j^2
\end{aligned}
\tag{A.3}
$$

Since $\delta t_i = \frac{\delta t}{2}\cos 2(\theta-\varphi)$, so the second IOF can be calculated by the averaging δt_i^2 over the entire range of the back azimuth:

$$
\begin{aligned}
\max\{I_{rcc}(\varphi,\delta t)\} &= \frac{1}{2\pi}\int_0^{2\pi}\{1+\frac{\omega_0^2}{2}\cdot\frac{\delta t^2}{4}[\cos^2 2(\theta_i-\varphi)+\cos^2 2(\theta_j-\varphi)]\}d\theta \\
&\approx 1+\tfrac{\omega_0^2}{8}\delta t^2
\end{aligned}
\tag{A.4}
$$

For an incoming S wave with a source time function *s(t)* and a radial polarization direction θ, the T component generated by azimuthal anisotropy is

$$
\begin{aligned}
T(t) &= \tfrac{1}{2}\{s(t-t_0+\tfrac{\delta t}{2})-s(t-t_0+\tfrac{\delta t}{2})\}\sin(\theta-\varphi)\cos(\theta-\varphi)+n(t) \\
&= \tfrac{1}{2}s'(t-t_0)\cdot\delta t\cdot\sin 2(\theta-\varphi)+n(t)
\end{aligned}
\tag{A.5}
$$

where, *n(t)* is random noise. If we assume $s(t)=\cos(\omega_0 t)$, then $s'(t)=-\omega_0\sin(\omega_0 t)$. Then the T energy ratio before and after anisotropic correction is:

$$
\begin{aligned}
I_t^{-1}(\theta) &= \int_{t_0-T_0/4}^{t_0+T_0/4}\{-\tfrac{\omega_0}{2}\sin\omega_0(t-t_0)\cdot\delta t\cdot\sin 2(\theta-\varphi)+n(t)\}^2 dt \Big/ \int_{t_0-T_0/4}^{t_0+T_0/4} n^2(t)dt \\
&= 1+\tfrac{\omega_0^2}{8}\delta t^2\sin^2 2(\theta-\varphi)/\bar{E}_n
\end{aligned}
\tag{A.6}
$$

where $\bar{E}_n = \frac{2}{T_0}\cdot\int_{t_0-T_0/4}^{t_0+T_0/4} n^2(t)dt$ is the average noise energy within the Moho Ps arrival time window.

Taking the average across the entire back azimuth,

$$\max\{I_t^{-1}(\varphi,\delta t)\} = \frac{1}{2\pi}\int_0^{2\pi} 1+\tfrac{\omega_0^2}{4}\delta t^2 \sin^2 2(\theta-\varphi)/\bar{E}_n d\theta$$
$$= 1+\tfrac{\omega_0^2}{16\bar{E}_n}\delta t^2 \qquad \text{(A.7)}$$

Appendix B: Crustal structure and deformation of the SE Tibetan plateau revealed by receiver function data*

Abstract

We analyze a large amount of receiver function data recorded by regional seismic networks of the China Earthquake Administration to estimate crustal structure and deformation beneath the southeast margin of the Tibetan plateau and its surrounding areas. We develop a comprehensive analysis method that facilitates robust extraction of azimuthal seismic anisotropy from receiver function data. The method includes an estimate of fast polarization direction and splitting time by a joint analysis of radial and transverse receiver function data, and an evaluation of measurement reliability by statistical and harmonic analysis. We find significant seismic anisotropy with a splitting time of 0.5-0.9 s beneath the SE margin of the Tibetan plateau. Both the splitting time and fast polarization direction are comparable to those estimated from SKS/SKKS data, suggesting that crustal anisotropy is the main cause of shear wave splitting of the SKS/SKKS wave. This also suggests that deformation in the upper mantle is either weak or predominantly vertical, and is obviously different from the one in the crust. A vertical flow in the upper mantle, combined with the observation of a thin lithosphere beneath the study area, leads to the inference that part of the mantle lithosphere may have been removed and is descending into deep mantle. Stations located in the surrounding areas, on the other hand, exhibit very little to no crustal anisotropy. The estimated Moho depth and *Vp/Vs* ratio also show

---

* The appendix is a reformatted version of the article "Crustal structure and deformation of the SE Tibetan plateau revealed by receiver function data", Earth and Planetary Science Letters (2012), 349-350, 186-197, doi:10.1016/i.epsl.2012.07.007, http://www.sciencedirect.com/science/article/pii/S0012821X12003664.

a distinct difference between the SE Tibetan plateau and the surrounding regions. Stations on the Tibetan plateau have a *Vp/Vs* ratio of ~1.79, which is substantially higher than those measured at the Yunnan-Guizhou (Yungui) plateau (~1.69). Our observations here are consistent with the scenario that the SE Tibet has been built by lower crustal flow. They also suggest that the mantle lithosphere beneath the margin may have been mechanically decoupled from the upper crust.

B.1. Introduction

The southeastern margin of the Tibetan plateau is located between the heartland of the plateau and the South China block, and spans most of Sichuan and Yunnan provinces and a part of Guizhou in southwest China (Figure B.1a). It is characterized by complex Cenozoic structures created during the India-Asia collision since ~50 Ma (Yin and Harrison, 2000). Two major models have been proposed to explain the deformation and uplift of this part of the plateau. In the first model, lateral extrusion of crustal blocks created the major strike slip faults in the region (e.g., Tapponnier et al., 1982), and in the second model lower crustal flow inflated the crust, causing the thickening of the crust and uplift of the plateau (e.g., Royden et al., 1997). From the block extrusion model, major deformation is expected to be localized along major shear zones. The latter model, on the other hand, predicts a diffuse deformation that can be observed widely across the margin. Both types of deformation have been observed with geological data, for example, Tapponnier et al. (1990) found that the Indochina block was displaced by at least 500 km southeastwards relative to the South China block along the Red River fault during the Oligo-Miocene. Incision data of the major rivers in the area, on the other hand, suggested an uplift occurring at regional scale after ~13 Ma (Clark et al., 2005). This

broad deformtion was interpreted as evidence for lower crustal materials flowing from the center to the SE margin of the plateau (Schoenbohm et al., 2006).

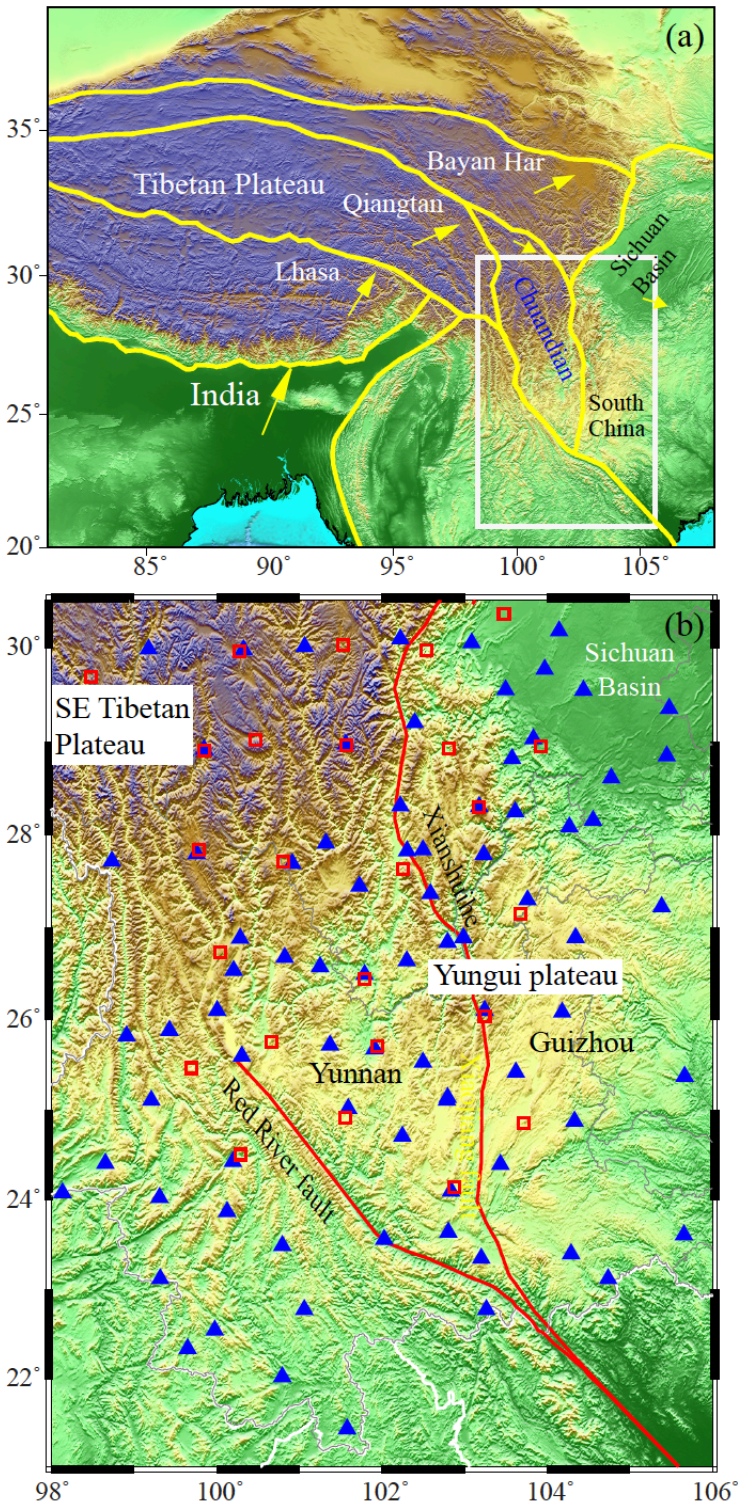

Figure B.1: (a) Map showing the surface motions of the India plate and different blocks within the Tibetan plateau relative to the stable Siberian craton. White box indicates the study region. (b) Topographic map showing the CEA broadband stations (solid blue triangle) and the PASSCAL stations (open red squares). Red lines indicate major faults in the area.

Similarly, geophysical data are also elusive. Seismic tomography showed that the distribution of low velocity anomalies (LVAs) in the lower crust is very heterogenous (Wang et al., 2003). Although it seems that the observed LVAs somehow correlate with the major fault systems in the area, the association between the LVAs and the proposed lower crustal flow is not so obvious. Magnetotelluric data, on the other hand, showed a wide distribution of channels with high electrical conductiviy at lower crustal depths across the margin (Bai et al., 2010). Thus the nature of deformation at depth beneath the region is still not well understood.

Questions also arise regarding the role that the lithospheric mantle plays during the crust thickening and surface uplift. Whether the mantle lithosphere deforms coherently with the crust or not is likely to have a very strong effect on crust dynamics. If surface uplift was caused mainly by inflation of the crust due to an active channel flow in the lower crust, then the mantle lithosphere and crust can deform differently as no substantial stress transfer can occur between them due to the low viscosity of the channel. On the other hand, if surface uplift and crustal thickening observed in the area are results of whole crustal shortening or block extrusion, then we would expect vertically coherent deformation across the entire lithosphere. Determing the depth distribution of deformation within the lithosphere thus becomes of great importance to understand the dominant orogenic process here.

Pervasive deformation can produce anisotropy on the scale of seismic wavelengths (e.g., Nicolas and Christensen, 1987; Mainprice and Nicolas, 1989). Measurements of seismic anisotropy thus can offer insight into the deformation kinematics within the Earth. Seismic anisotropy in earth's upper crust is generally believed to be caused by stress-induced alignment of cracks. The cause of seismic aniostropy in the lower crust and mantle, on the other hand, is usually attributed to strain-induced lattice-preferred-orientation (LPO) of crustal and upper mantle minerals, such as mica, amphibole, and olivine. Because of its close relationship with the stress/strain field, seismic anisotropy has been widely used to quantify subsurface deformation associated with a wide range of tectonic processes (Crampin and Lovell, 1991; McNamara and Owens, 1993; Silver, 1996).

Both SKS waveform splitting and surface wave dispersion have been measured in the southeastern margin of the plateau to estimate seismic anisotropy (e.g., Lev et al., 2006; Wang et al., 2008; Yao et al., 2010). Lev et al. (2006) measured shear wave splitting of the core-refracted SKS/SKKS waves recorded by a temporary array of 25 stations in the area. Overall, the observed SKS/SKKS splitting times are of low amplitude, varying between 0.28 and 0.92 except for one station (1.2 s) with an average value of 0.58 s. The fast polarization direction exhibits a distinct transition from roughly the NS direction in the Tibetan plateau to mostly the EW direction in the Yunnan-Guizhou plateau (Yungui) plateau. The deformation field in the mantle beneath the Yungui plateau apparently differs from the surface deformation field, suggesting a decoupled motion between the crust and mantle. On the other hand, the observed NS fast polarization direction agrees roughly with the surface deformation field, indicating that

deformation within the lithosphere of the SE Tibetan plateau might be vertically coherent. Lev et al. (2006) argued that the source region of the observed seismic anisotropy from SKS/SKKS splitting data is likely located in the shallow mantle at ~60 to 160 km depth, which implies that seismic anisotropy in the crust is insignificant. Due to limited coverage in back azimuth, Lev et al. (2006) explained that multiple layers of anisotropy could not be ruled out with their dataset.

The P-to-S converted wave at the Moho, which can be extracted by receiver function analysis, is now widely used in measuring seismic anisotropy in the crust. In general, this conversion wave is registerd as a very weak signal in individual receiver functions. Making robust measurement of crust anisotropy with such a weak signal can be extremely difficult and dangerous. Recently, Liu and Niu (2012) developed a splitting measurement technique specifically for receiver function data. It utilizes the features that are uniquely possessed by anisotropic models observed on the synthetic receiver function data. We further added a harmonic analysis component to the method to enhance the evaluation of measurement reliability. We applied the technique to the broadband data recorded by regional seismic networks operated by the China Earthquake Administration (CEA). We selected a total of 79 stations located on the SE Tibetan plateau and its sourrounding areas, including the Sichuan Basin, the Yunnan-Guizhou (Yungui) plateau and the fold belts further in the south. We measure crustal anisotropy, Moho depth and crustal *Vp/Vs* ratio at the 79 stations to constrain the average composition and deformation processes within the crust. The seismic measurements are then used to test the dynamic models mentioned above.

B.2. CEA Regional Network Data

The data used in this study are collected from CEA's four provincial networks: Chongqing (CQ), Sichuan (SC), Yunnan (YN), and Guizhou (GZ). To study lateral variations in crustal structure and deformation of the SE Tibetan plateau and its surrounding areas, we choose 79 stations located in the region between 98° and 106° east, and 21° to 30.5° north (Figure B.1b). Several stations are very close to the sites of the IRIS-PASSCAL temporary array deployed by MIT and the Chengdu Institute of Geology and Mineral Resources (CIGMR) between 2003 and 2004. We select a total of 413 earthquakes within an epicentral distance of 30°–90°, recorded between July of 2007 and July of 2010. These earthquakes provide very good coverage in both distance and azimuth (Figure B.2).

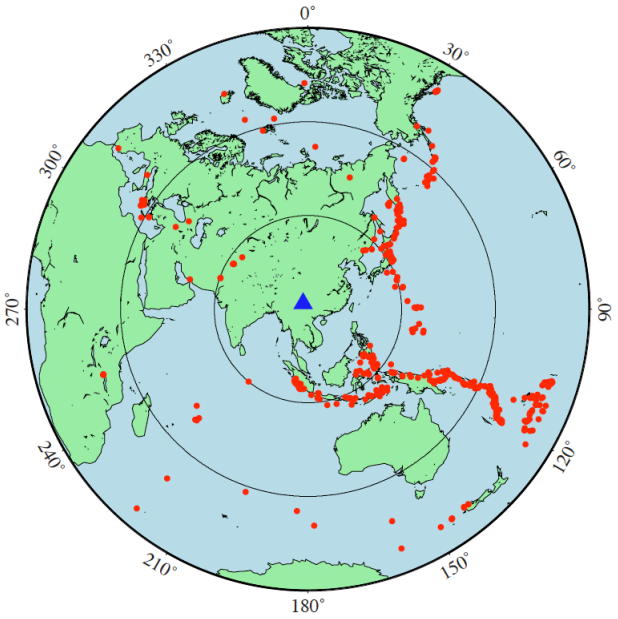

Figure B.2. Locations of the 413-teleseismic events (red solid circles) used in this study. Most of the earthquakes are located in the western and south Pacific, as well as the Indonesia subduction zones. Note that although some events fall into the 30° circle from the array center, all the seismograms we used have an epicentral distance between 30° and 90°.

B.3. Methods

B.3.1. Receiver function generation and moveout corrections

To generate receiver functions, we first rotate the two horizontal components into radial (R) and transverse (T) components. Niu and Li (2011) found that a significant portion of the CEA regional network stations have orientation problems, so we use their method to compute the sensor orientation for each station before the rotation. We further rotate the radial (R) and vertical (Z) into the P and SV coordinates (e.g., Vinnik, 1977; Niu and Kawakatsu, 1998). We employ the "water-level" deconvolution technique to generate R, T, and SV receiver functions (e.g., Ammon, 1991; Pan and Niu, 2011). The R and T receiver functions are then used in harmonic analysis and the estimation of seismic anisotropy; while the SV receiver functions are used in the *H-k* analysis. We visually inspect all the receiver functions and remove those with a low signal-to-noise ratio (SNR). At each station, we further calculate the covariance matrix of all the receiver functions and eliminate the ones that show a low cross correlation coefficient (<0.7) with other traces (Chen et al., 2010). The number of receiver functions selected at the 79 stations varies from 77 to 296, with an average of 220 (Table B.1).

Station	Lon. (°)	Lat. (°)	Ele. (km)	TB[1]	No. RFs	H[2] (km)	K[3]	t_{ps}	n[4]	φ (°)[5]	Dt (s)	SNR ana.[6]	note[7]
SC.YGD	104.1	30.2	0.800	SB	251	49.0±1.0		5.94	1	77	0.10	0	
SC.JYA	103.9	29.8	0.570	SB	234	53.2±1.4	1.761+0.007	6.72	1	160	0.34	0	
SC.HMS	***104.4***	***29.6***	***0.839***	***SB***	***296***	***45.2±0.9***	***1.792+0.015***	***5.94***	***2***	***54***	***0.32***	***1***	
CQ.ROC	***105.4***	***29.4***	***0.213***	***SB***	***295***	***41.3±0.8***	***1.708+0.019***	***4.86***	***2***	***71***	***0.24***	***1***	
SC.HWS	104.7	28.6	0.860	SB	279	40.8±0.7	1.777+0.018	5.26	4	52	0.22	1	
SC.JLI	104.5	28.2	0.480	SB	282	39.3±1.3	1.765+0.032	4.99	1	43	0.30	0	
SC.SMI	102.3	29.2	0.860	SB	247	51.2±0.7	1.829+0.016	7.05	1	146	0.40	0	
SC.EMS	***103.5***	***29.6***	***0.467***	***SB***	***250***	***50.0±0.9***	***1.722+0.014***	***6.00***	***2***	***172***	***0.70***	***1***	***MC02* 167 0.61***
SC.MDS	103.0	30.1	1.210	SB	195	48.3±0.9	1.776+0.018	6.22	1	100	1.06	1	
SC.WMP	103.8	29.1	1.260	SB	269	41.4±1.3	1.856+0.029	5.87	1	118	0.10	0	MC10 135 0.90

SC.MBI	103.5	28.8	0.640	SB	245	46.9±0.8	1.740+0.014	5.77	3	55	0.70	0	
SC.LBO	103.6	28.3	1.310	SB	242	52.5±0.9	1.689+0.012	6.02	3	73	0.52	1	
YN.YAJ	104.2	28.1	0.575	SB	254	45.1±0.8	1.746+0.014	5.59	1	157	0.30	0	
SC.BTA	99.1	30.0	2.639	TP	279	71.1±1.2	1.743±0.013	8.78	3	113	0.20	0	
SC.LTA	***100.3***	***30.0***	***3.951***	***TP***	***258***	***57.8±0.8***	***1.803+0.015***	***7.40***	***2***	***102***	***0.62***	***1***	***MC05 100 0.85***
SC.YJI	***101.0***	***30.0***	***2.670***	***TP***	***279***	***62.1±1.9***	***1.767+0.025***	***7.09***	***2***	***125***	***0.90***	***1***	
SC.GZA	102.2	30.1	1.410	TP	279	60.5±1.3	1.863+0.017	8.68	1	68	0.80	1	
SC.XCE	99.8	28.9	3.000	TP	203	62.6±0.9	1.739+0.009	7.64	2	102	0.70	0	MC06 159 0.55
SC.JLO	101.5	29.0	2.915	TP	258	61.2±0.8	1.812+0.012	8.24	3	147	0.58	1	
SC.MNI	102.2	28.3	1.657	TP	198	65.8±1.1	1.784+0.010	8.56	7	179	1.20	0	
SC.MGU	103.1	28.3	2.056	TP									MC11 149 0.67
SC.LGH	100.9	27.7	2.669	TP	225	56.4±1.3	1.786+0.016	7.36	2	8	0.40	0	MC13 81 0.46
YN.ZOD	99.7	27.8	3.248	TP	185	55.3±0.6	1.780+0.011	7.19	1	0	1.10	0	MC14 141 0.55
SC.YYU	101.7	27.5	2.596	TP	228	63.4±2.3	1.802+0.018	8.44	1	147	0.30	0	
SC.YYC	102.3	27.9	1.608	TP	236	59.8±1.1	1.762+0.012	7.55	1	90	0.80	1	
SC.XSB	102.4	27.9	2.800	TP	248	62.7±1.3	1.779+0.012	8.11	2	98	0.70	0	
SC.BYD	103.2	27.8	3.142	TP	125	48.8±1.0	1.883+0.019	7.13	1	161	0.98	1	
SC.PGE	102.5	27.4	1.427	TP	266	59.0±0.8	1.678+0.010	6.66	1	153	0.52	1	
SC.MLI	101.3	27.9	2.437	TP	188	48.8±0.7	1.701+0.015	5.69	1	115	1.20	1	
YN.GOS	98.7	27.7	1.470	TP	136	46.0±1.0		5.55	1	85	1.00	1	
YN.ZAT	103.7	27.3	1.940	TP	220	46.6±1.3	1.730+0.016	5.65	1	112	0.58	1	
YN.QIJ	102.9	26.9	1.112	TP	77	62.0±1.0		7.60	1	167	0.70	0	
YN.LIJ	***100.2***	***26.9***	***2.480***	***TP***	***180***	***62.0±1.0***		***7.40***	***2***	***4***	***0.80***	***1***	***MC15* 161 0.30***
YN.YOS	100.8	26.7	2.200	TP	213	56.0±0.7	1.704+0.012	6.56	3	145	1.50	0	
YN.HEQ	***100.2***	***26.6***	***2.210***	***TP***	***192***	***52.0±1.2***	***1.773+0.020***	***6.67***	***2***	***159***	***0.70***	***1***	***MC15* 161 0.30***
YN.HUP	***101.2***	***26.6***	***1.286***	***TP***	***237***	***56.2±0.7***	***1.737+0.019***	***6.88***	***2***	***146***	***0.50***	***1***	
SC.PZH	101.7	26.5	1.190	TP	156	55.5±3.3	1.686+0.035	6.34	1	135	0.90	0	MC17 59 0.50
SC.HLI	102.3	26.7	1.836	TP	236	48.0±0.8	1.713+0.023	5.69	1	115	1.50	0	
SC.SMK	102.8	26.9	2.385	TP	213	53.9±1.0	1.777+0.015	6.95	5	78	0.72	1	
GZ.WNT	104.3	26.9	2.334	TP	171	50.1±1.2	1.817+0.011	6.80	2	15	0.80	0	
YN.DOC	103.2	26.1	1.228	TP	131	46.9±0.7	1.926+0.018	7.09	1	139	0.78	1	MC18 95 0.61
GZ.BJT	105.4	27.2	1.462	YG	162	49.7±1.0	1.672+0.013	5.40	3	50	0.60	0	
YN.XUW	104.1	26.1	2.073	YG	253	48.8±0.9	1.647+0.016	5.26	1	147	0.30	0	
YN.LUS	98.9	25.8	0.845	YG	233	42.7±1.1	1.735+0.023	5.22	3	179	0.30	0	
YN.YUL	99.4	25.9	1.700	YG	239	46.2±0.9	1.716+0.021	5.50	2	153	0.70	0	
YN.EYA	100.0	26.1	2.072	YG	178	48.1±0.9	1.715+0.017	5.72	3	168	0.50	1	
YN.TUS	100.3	25.6	1.967	YG	176	46.0±1.2	1.670+0.021	5.13	1	100	0.56	1	
YN.DAY	101.3	25.7	1.860	YG	207	48.0±1.0	1.651+0.009	5.29	1	75	0.10	0	

YN.YUM	101.9	25.7	1.085	YG	196	45.0±1.8	1.724+0.032	5.42	2	109	0.10	0	
YN.LUQ	102.5	25.5	1.777	YG	207	45.0±5.6	1.724+0.094	5.39	1	25	0.20	0	
YN.CUX	***101.5***	***25.0***	***1.840***	***YG***	***236***	***49.4±0.8***	***1.664+0.014***	***5.46***	***2***	***173***	***0.40***	***1***	***MC23 82 0.48***
YN.HLT	102.8	25.2	1.892	YG	132	45.5±0.9	1.723+0.027	5.47	4	115	0.22	1	
YN.KMI	102.7	25.1	1.975	YG	157	46.6±1.2	1.702+0.031	5.26	2	175	0.12	0	
YN.MAL	103.6	25.4	2.010	YG	255	46.8±0.9	1.659+0.019	5.14	1	33	0.10	0	
YN.YIM	102.2	24.7	1.630	YG	244	46.0±1.1	1.665+0.026	5.10	1	43	0.70	0	
YN.LOP	104.3	24.9	1.478	YG	234	41.0±1.2	1.705+0.021	4.81	1	149	0.52	1	
YN.MIL	103.4	24.4	1.550	YG	238	42.4±0.9	1.731+0.019	5.15	2	19	0.40	0	
YN.TOH	102.8	24.1	1.870	YG	229	40.9±0.9	1.790+0.028	5.35	7	70	0.00	0	MC24 73 0.28
YN.JIS	102.8	23.7	1.380	YG	192	41.5±1.6	1.655+0.031	4.53	1	166	0.24	1	
YN.BAS	99.2	25.1	1.675	WB	193	39.0±0.8	1.733+0.019	4.75	3	176	0.60	0	
YN.WAD	***98.1***	***24.1***	***0.920***	***WB***	***252***	***36.3±0.9***	***1.697+0.019***	***4.21***	***2***	***51***	***0.34***	***1***	
YN.MAS	98.6	24.4	0.920	WB	221	34.5±0.7	1.780+0.022	4.47	3	157	0.34	1	
YN.YOD	99.3	24.0	1.690	WB	262	33.4±1.0	1.816+0.036	4.52	6	24	0.44	1	
YN.YUX	***100.1***	***24.4***	***1.110***	***WB***	***212***	***37.7±0.8***	***1.751+0.019***	***4.70***	***2***	***161***	***0.24***	***1***	***MC22 65 0.43***
YN.LIC	100.1	23.9	1.580	WB	231	37.4±2.9	1.695+0.025	4.33	2	129	0.80	0	
YN.JIG	100.7	23.5	1.030	WB	232	38.1±0.9	1.629+0.020	3.90	1	139	0.10	0	
YN.CAY	99.3	23.1	1.390	WB	237	34.2±1.1	1.728+0.022	4.14	2	71	0.18	0	
YN.SIM	101.0	22.8	1.360	WB	219	35.0±0.9	1.758+0.033	4.41	2	29	0.44	0	
YN.MEL	99.6	22.3	0.934	WB	246	32.6±0.7	1.741+0.024	4.01	3	28	0.10	0	
YN.LAC	99.9	22.6	1.222	WB	257	35.7±0.8	1.673+0.021	4.00	1	111	0.62	1	
YN.JIH	100.7	22.0	0.570	WB	257	32.8±1.0	1.701+0.028	3.90	3	18	0.00	0	
YN.MLA	101.5	21.4	0.647	WB	218	33.4±1.2	1.682+0.034	3.79	1	154	0.44	1	
YN.YUJ	***102.0***	***23.6***	***0.529***	***WB***	***222***	***37.1±4.2***	***1.710+0.073***	***4.38***	***2***	***115***	***0.58***	***1***	
YN.JIP	103.2	22.8	1.305	WB	241	38.1±0.8	1.687+0.018	4.35	1	49	0.50	0	
YN.GEJ	103.2	23.4	1.840	SF	188	38.3±1.5	1.759+0.032	5.57	3	60	0.20	0	
YN.WES	104.3	23.4	1.480	SF	266	38.3±0.8	1.705+0.021	4.49	6	3	0.10	0	
YN.MLP	104.7	23.1	1.054	SF	196	35.1±1.4	1.687+0.048	4.01	3	97	0.50	1	
GZ.ZFT	105.6	25.4	1.049	SF	96	35.1±1.3	1.733+0.040	4.28	1	21	0.01	0	
YN.FUN	105.6	23.6	0.684	SF	239	36.3±0.8	1.673+0.022	4.10	1	163	0.54	1	

1: Tectonic block, SB: Sichuan Basin; TP: Tibetan plateau; YG: Yungui plateau; WB: Western Yunnan Folds and Belts, including the Tengchong block, Changning-Menglian Belt, Lanping-Simao Fold System, Ailaoshan Belt; SF: South China Fold system.
2: Crustal thickness, if *Vp/Vs* ratio is not given, the iasp91 *Vp/Vs* ratio is used;
3: *Vp/Vs* ratio;
4: harmonic degree;
5: fast polarization direction (clockwise from north)
6: statistical test, 0: negative; 1: positive.
7: Co-sited station name of the 2003-04 MIT/CIGMR array, *: not cosited, the closest station. SKS fast polarization direction and delay time from Lev et al., 2006.

Table B.1. Measured Moho depth, V_P/V_S ratio, fast polarization direction and splitting time

The Moho Ps conversion phase has a slightly negative ray parameter relative to the direct P wave. The relative arrival time of the Ps thus has a negative distance moveout with respect to the direct P wave. We use the *H-k* results to compute this moveout and make corrections so that all the Ps phases have a relative arrival time equivalent to the one with an epicentral distance of 60° and a source depth of 0 km. We further normalize the R and T receiver functions by dividing them by the peak amplitude of the P wave on the R component. After the moveout correction and the normalization, the R and T receiver functions are plotted as a function of back azimuth to detect systematic variations in the peak Ps arrival time and polarity changes in the R and T receiver functions, respectively.

B.3.2. Harmonic analysis of Ps arrival time

We first stack all the R receiver functions to get the average arrival time of the Moho Ps conversion phase, t_o . We then apply harmonic analysis to a time window with a length of t_L centered on t_o to find systematic variations in the arrival time of the Ps conversion as a function of back azimuth. Assuming a harmonic degree, n, with a peak-to-peak amplitude of δt, and initial phase of φ, the harmonic moveout correction at a station with a back azimuth of θ_i, is,

$$\delta t_i = \frac{\delta \mathrm{t}}{2} \cdot \cos(\mathrm{n}\theta_i + \varphi) \cdot \tag{B.1}$$

We then stack all the R receiver functions after correcting the harmonic moveout:

$$F_r(t,\varphi,\delta \mathrm{t}) = \sum_{\mathrm{i}=1}^{N} F_{\mathrm{r}}^i(t\text{-}\delta \mathrm{t}_i), \qquad t \in [t_o - 0.5t_L, t_o + 0.5t_L] \tag{B.2}$$

The superscript *i* here represents the *i-th* receiver function, and *N* is the total number of receiver functions. We further compute the normalized maximum amplitude, maximum energy of the

stacked receiver function, and minimum total residual between each receiver function and the stacked receiver function:

$$
\begin{aligned}
A_{n,\max} &= \max\{F_r(t,\varphi,\delta\mathrm{t})\} / \max\{F_r(t,0,0)\} \\
E_{n,\max} &= \max\left\{\sum_{t=t_o-\frac{1}{2}t_L}^{t=t_o+\frac{1}{2}t_L} F_r^2(t,\varphi,\delta\mathrm{t})\right\} \Big/ \max\left\{\sum_{t=t_o-\frac{1}{2}t_L}^{t=t_o+\frac{1}{2}t_L} F_r^2(t,0,0)\right\} \\
R_{n,\min} &= \min\left\{\frac{1}{N}\sum_{i=1}^{N}\sum_{t=t_o-\frac{1}{2}t_L}^{t=t_o+\frac{1}{2}t_L}\left[F_r(t,\varphi,\delta\mathrm{t}) - F_r^i(t,\varphi,\delta\mathrm{t})\right]^2\right\} \Big/ \min\left\{\frac{1}{N}\sum_{i=1}^{N}\sum_{t=t_o-\frac{1}{2}t_L}^{t=t_o+\frac{1}{2}t_L}\left[F_r(t,0,0) - F_r^i(t,0,0)\right]^2\right\}
\end{aligned}
\tag{B.3}
$$

Here $A_{n,max}$ and $E_{n,max}$ represent the maxima of the normalized peak amplitude and total energy of the stacked receiver function. $R_{n,min}$ is the minimum of the summed residual between the stacked receiver function and the individual receiver functions. $A_{n,max}$, $E_{n,max}$, and $R_{n,min}$ are taken from the entire Ps conversion time window, and the entire *(φ, ät)* domain. We varied *n* from 1 to 8, φ in the range of 0° to 360° with an increment of 1°, and δt from 0.0 to 1.5 s in increments of 0.02 s.

An example of the harmonic analysis is shown in Figure B.3b. The maximum amplitude and energy of the stacked receiver function, as well the best fit between the stacked and individual receiver functions have a distinct peak at degree-2. As many studies (e.g., Levin and Park, 1997; Peng and Humphreys, 1997; Savage, 1998; Shiomi and Park, 2008) have shown, several types of crustal structure, such as a dipping Moho, P-wave anisotropy or azimuthal S-wave anisotropy with an inclined axis, can result in a degree-1 back azimuthal variation. On the other hand, azimuthal S-wave anisotropy with a horizontal axis can register a Ps signal that has a degree-2 back azimuthal variation in arrival time. Small-scale azimuthal variations in crustal velocity and Moho topography may result in higher order harmonic variations.

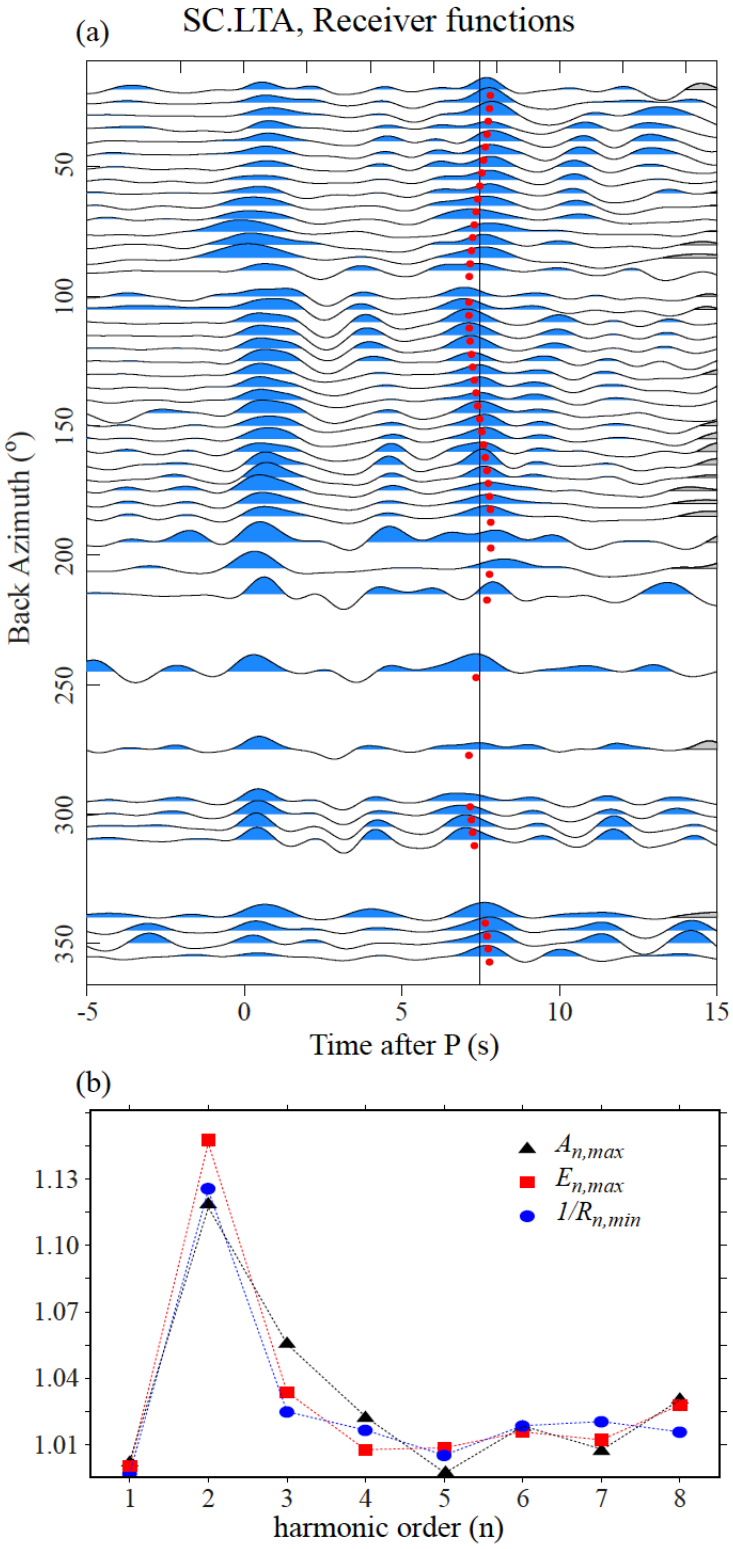
(a)
SC.LTA, Receiver functions
Back Azimuth (°)
50
100
150
200
250
300
350
-5
0
5
10
15
Time after P (s)
(b)
$A_{n,max}$
$E_{n,max}$
$1/R_{n,min}$
1.13
1.10
1.07
1.04
1.01
1
2
3
4
5
6
7
8
harmonic order (n)

Figure B.3. (a) SV receiver functions recorded at station SC.LTA are plotted as a function of back azimuth. The receiver functions here are stacked in 10° bins along the back azimuth direction. Solid line indicates the average arrival times of the primary P to S conversion phase, and red dots represent the azimuthal variation in its arrival time. (b) Results of the harmonic analysis at the same station. The maximum value of peak amplitude and total energy, as well as the reciprocal of the minimum residual are shown as a function of the harmonic degree. Note the peak at the degree-2, indicative of azimuthal seismic anisotropy with a horizontal axis in the data.

B.3.3. Estimate of crustal anisotropy

When radially polarized S waves propagate through an anisotropic crust with a horizontally symmetrical axis, their energy is split and part of it is projected onto the transverse component. The birefringent T waveforms are proportional to the time derivative of those on the R component. In addition, the arrival time and the polarity of the S wave on both the R and T components each exhibit a four-lobe (degree-2) variation pattern along the back azimuth direction. These two unique features of azimuthal anisotropy provide a strong base for resolving it from other heterogeneous structures, such as velocity heterogeneities in the crust and a tilted crust-mantle boundary.

Although we make anisotropy measurements at all the stations, we only select the results of the stations that exhibit a strong degree-2 azimuthal variation. The method used here was developed by Liu and Niu (2012). Here we briefly review the major steps they proposed to better constrain

azimuthal anisotropy with receiver function data. The method includes computing three individual and one joint objective function, and a statistical analysis of the reliability of the estimated anisotropy. The individual objective functions (IOFs) are designed to search for a pair of φ and $\ddot{a}t$ that: 1) maximize the peak energy of the stacked R receiver function after a cosine moveout correction in the Ps arrival time; or 2) maximize the cross-correlation of the radial receiver functions after a full correction of crustal anisotropy; or 3) minimize the total energy of transverse receiver functions stacked after a removal of crustal anisotropy. The joint objective function (JOF) is computed by taking the average of the three IOFs, while the statistical analysis utilizes the principle that stacking a total of N coherent signals can lead to an increase of SNR by a factor of $N^{1/2}$. Further information can be found in Liu and Niu (2012) for details on the method.

In Figure B.4, we show the results measured at station SC.LTA. The three IOFs are shown in Figures B.4a, B.4b, and B.4c, respectively. The fast polarization direction and the splitting time estimated from the three methods are in good agreement with each other. The JOF estimate is closer to the value estimated from the transverse component because of the large maximum value of the third IOF. As discussed in Liu and Niu (2012), the maxima (the difference between maxima and unit value) of the three IOFs and the subsequent JOF are proportional to splitting time. The large maximum amplitude of the JOF obtained here is thus a strong manifestation of crustal anisotropy beneath the station. Results of the statistical analysis of the measurement reliability based on the T and R receiver functions are shown in Figures B.4e and B.4f, respectively. The analysis with the T receiver functions indicates that the SNR of the data stacked after a correction of waveform polarity roughly increases linearly with $N^{1/2}$ (open

squares in Figure B.4e) while the SNR of those stacked without a correction of waveform polarity remains nearly flat across the whole range of $N^{1/2}$ (open circles in Figure B.4e). On the other hand, once anisotropy is removed, the T receiver functions are composed primarily of random noise, leading to a flat distribution of SNR no matter whether a polarity correction (filled squares in Figure B.4e) is applied or not (filled circles in Figure B.4e). If anisotropy is signficant, then the stacked R receiver functions after the correction of crustal anisotropy (filled triangles in Figure B.4f) are expected to have a larger *SNR* than those without correction (open triangles in Figure B.4f).

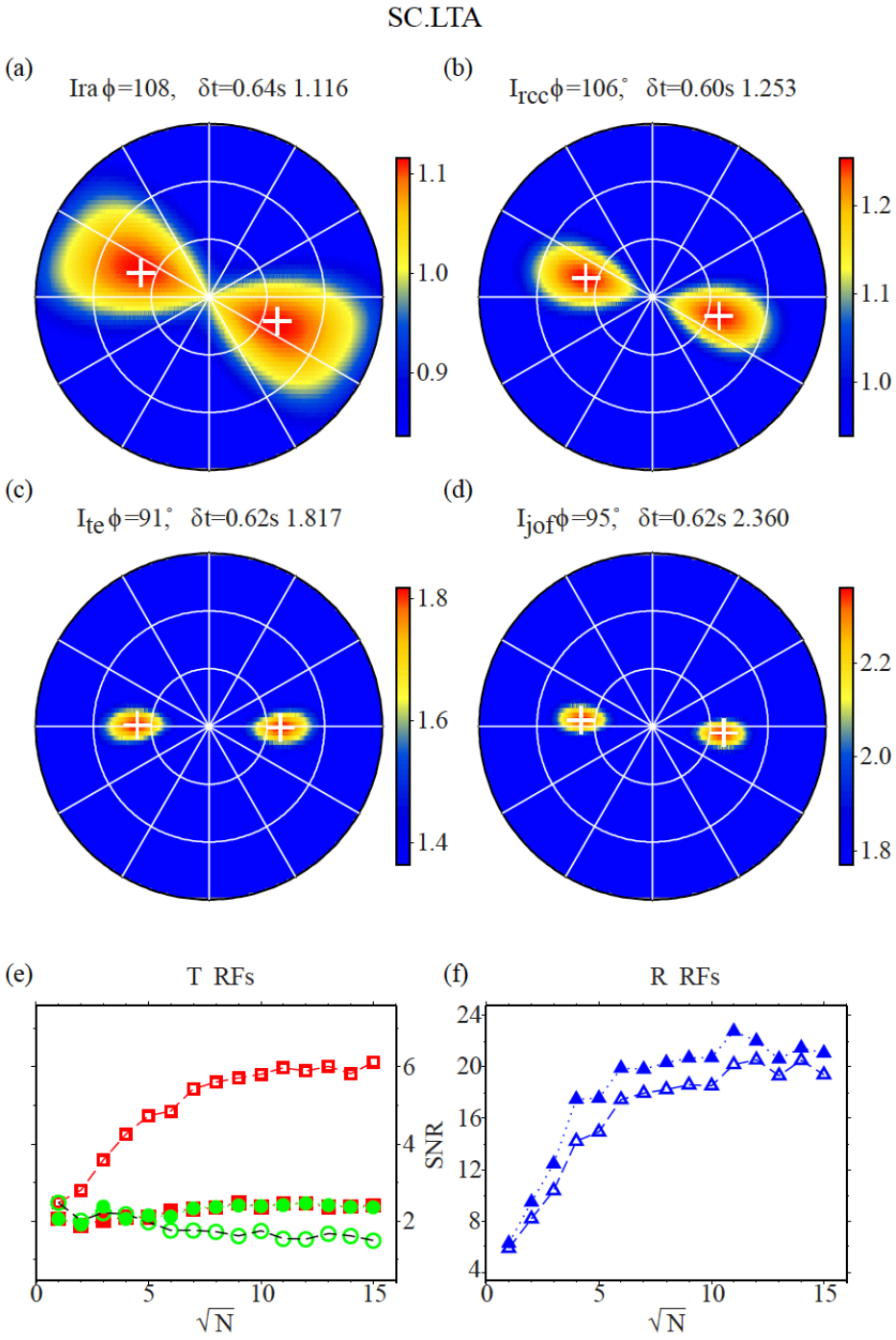

Figure B.4. Results from the joint analysis of crustal anisotropy at station SC.LTA. (a), (b), and (c) correspond to three different methods for estimating seismic anisotropy: (1) R energy maximization with a cosine moveout correction; (2) Radial cc maximization; and (c) T energy

minimization(represented by maximizing the inverse of T energy). Color scales showing variations of the objective functions are plotted to the right of the functions. The JOF is shown in (d). The objective functions were computed in a 2D plane of *(φ, ät*) in the range of (*0°-360°, 0.0-1.5s*) with an increment of (*1°, 0.02s*). (e) and (f) show the reliability analysis of the estimated anisotropy with the T and R receiver function data, respectively. Open and filled symbols in (e) and (f) represent SNR calculated from stacks of receiver functions before and after the removal of seismic anisotropy determined by the JOF. Note the steady increase of square (stack with a sign correction of back azimuth) with increasing $N^{1/2}$ in (e) and that the filled triangles are always above the open ones in (f).

In Figure B.5, we show part of the SV and T receiver functions before and after the correction of the estimated crustal anisotropy. From the original SV receiver function, we can see a clear azimuthal variation in the Ps arrival time (Figure B.5a). The Ps conversion phase can also be seen on the T receiver functions, with a clear change in waveform polarity (Figure B.5b). These features are no longer seen from the data once seismic anisotropy is corrected. More specifically, the Ps converted phase arrives roughly at the same time on the radial component, and there are no obvious Ps arrivals on the transverse component (Figures B.5c and B.5d).

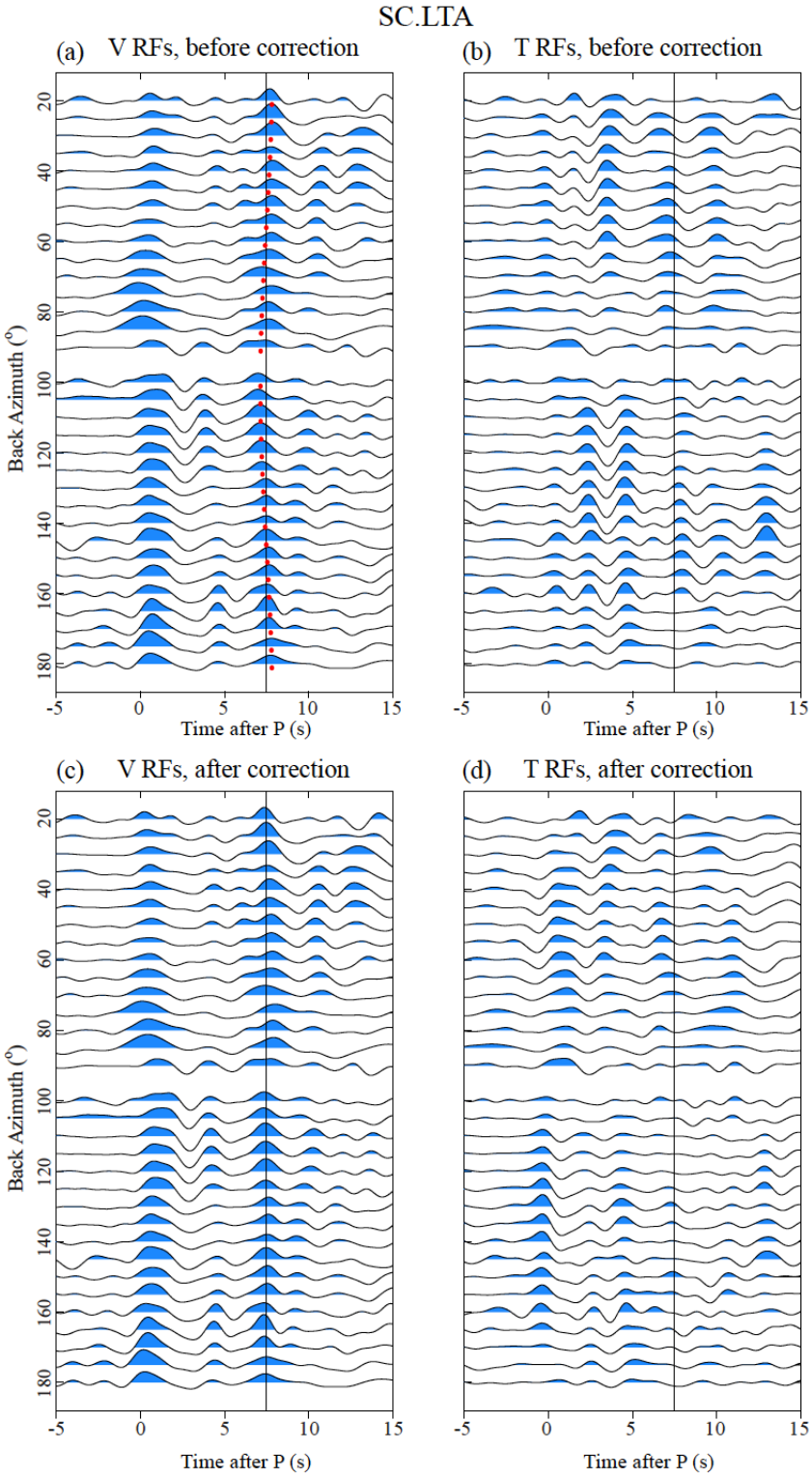
SC.LTA
(a) V RFs, before correction
(b) T RFs, before correction
(c) V RFs, after correction
(d) T RFs, after correction
Back Azimuth (°)
Time after P (s)
20
40
60
80
100
120
140
160
180
-5
0
5
10
15

Figure B.5. A comparison between receiver functions before (a, b) and after the correction (c, d) of seismic anisotropy. Receiver functions shown here are recorded at station SC.LTA and are binned in 10° azimuthal caps. The solid line indicates the average arrival time of the Moho Ps converted phase. The SV and T components before correction of anisotropy are shown in (a) and (b), respectively. Dots in (a) indicate the arrival time of the peak amplitude of the Moho Ps converted phase. Note its cosine variation along the back azimuthal direction in (a), and the polarity changes of the Ps phase in (b). The SV and T receiver functions after the removal of anisotropy are shown in (c) and (d), respectively. Note the good alignment of the Ps after the correction in (c), and the low energy along the line of the Ps arrival time window in (d) after the contribution of seismic anisotropy has been removed.

B.3.4. Depth stacking and H-*k* analysis

We also apply H-*k* stacking to all the stations to determine the Moho depth and the average *Vp/Vs* ratio (*k*) of the crust. To do so, we employ the method proposed by Niu et al. (2007). We first use a depth stacking method to determine an initial depth for the Moho beneath a station. We then employ a refined *H-k* analysis to determine the final estimates of depth and *Vp/Vs* that best match the observed P to S conversion and the reverberation phases. To obtain the initial depth, we first gather receiver functions recorded at each station and make a time to depth conversion by assuming that P to S conversions are the primary sources of energy in the P-wave coda window. For a conversion depth, *d*, we first compute the relative arrival time of the converted phase, *Pds*, with respect to the direct arrival by ray tracing the two phases using a modified 1D iasp91 velocity model (Kennett and Engdahl, 1991), which has a crust extending to depth *d*. We then sum the receiver function values averaged in a 0.1s window centered on the

arrival time of *Pds* using both linear and non-linear stacking technique (e.g., Muirhead, 1968; Kawakatsu and Niu, 1994). We vary *d* from 0 to 100 km at an increment of 1 km and use the depth with maximum amplitude as the initial Moho depth. The stacked depth profile at station SC.LTA is shown in Figure B.6a. We can see a clear P-to-S conversion peak at depth around 61 km.

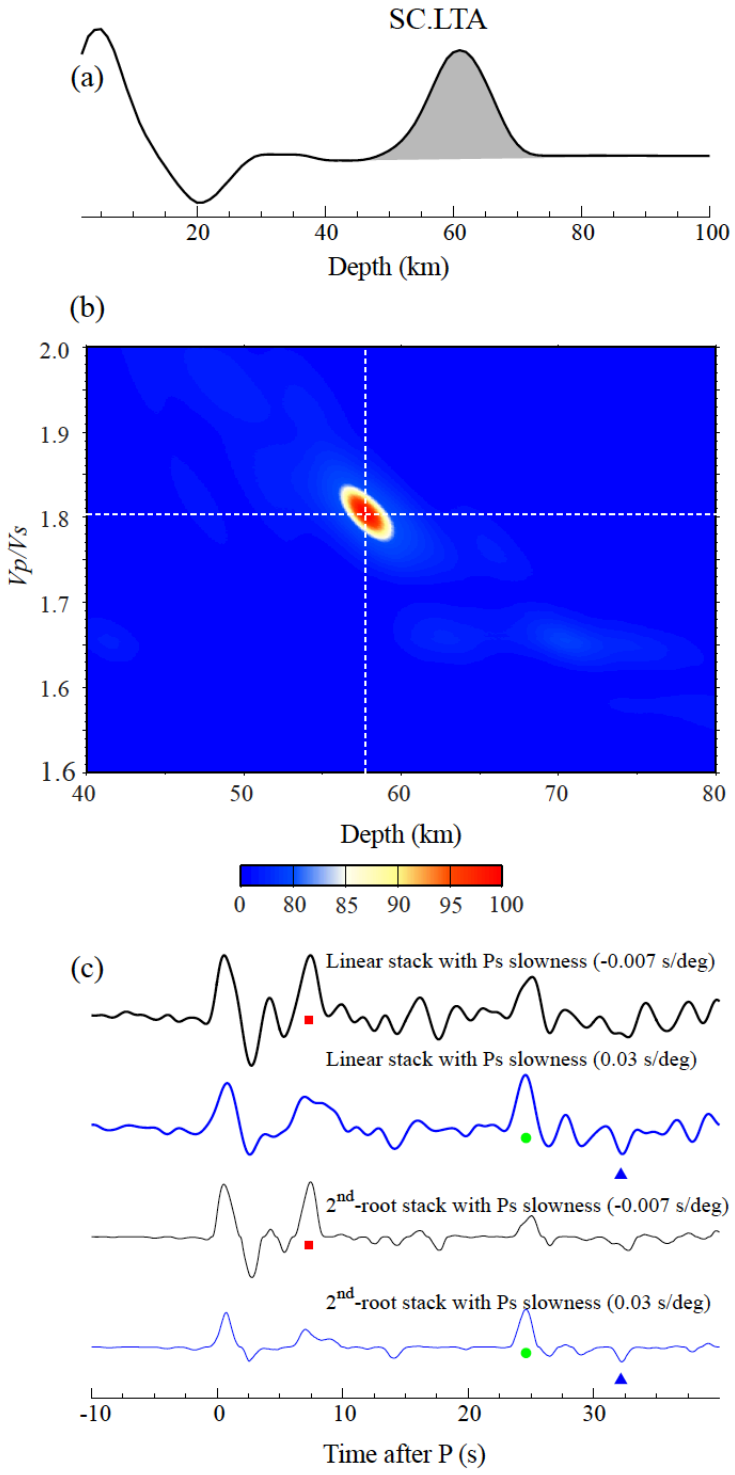

Figure B.6. (a) The stacked receiver function after the time-to-depth conversion at station SC.LTA. The peak of the Ps conversion is at 61 km. (b) Results of the *H-ê* analysis obtained

from SC.LTA. Color contours show the summed amplitude as a function of crustal thickness and *Vp/Vs* ratio. The two white lines indicate location of the amplitude peak. (c) Stacked receiver functions with the Ps slowness (the first and third traces) and the 2p1s slowness (the second and fourth traces). The top two traces are obtained by a linear stack while the bottom two are computed from a 2^{nd}-root stack. The square, circle, and triangle indicate the Ps, 2p1s and 1p2s phase, respectively. Note that amplitude of the phases is larger when they are stacked with the correct slowness.

The estimated crustal thickness, *H*, by the above depth stacking method, depends on the reference velocity model. There is a complete trade off between *H* and the *Vp/Vs* ratio, and *Vp* (Nair et al., 2006). Adding the two crustal multiples (2p1s and 1p2s, Niu and James, 2002) in the stacking can, in principle, resolve the trade off (Zhu and Kanamori, 2000). In most of studies, however, the two multiples are assigned a low weight in the stacking due to the low SNR of the two phases. This can introduce large trade off between *H* and *k*. Niu et al. (2007) introduced a coherence index of the three phases, *c(k)*, to reduce the *H-k* tradeoff:

$$s(H,\kappa) = \frac{c(\kappa)}{N}\sum_{i=1}^{N}\left\{w_1 r_i(t_1) + w_2 r_i(t_2) - w_3 r_i(t_3)\right\}. \quad \text{(B.4)}$$

Here *N* is the number of receiver functions at a given station and $r_i(t)$ represents the amplitude of the i^{th} receiver function at the predicted arrival times of the primary P-to-S converted phase *0p1s (t1)*, and the two crustal multiples, *2p1s (t2)* and *1p2s (t3*). w_1, w_2, and w_3 are the weights of the three phases and are assigned to 0.5, 0.25, and 0.25, respectively. We search for *H* within ±20 km of the initial depth determined from the depth stacking. $\hat{e}$ is varied in the range of 1.5 to 2 with an increment of 0.001. *H* and $\hat{e}$ ratio are finally determined by picking the location where

the summed amplitude, *s(H,ê)*, reaches its maximum. For each station, we use a 1D P-wave velocity model derived from a 3D traveltime tomography study (Sun and Toksoz, 2006).

The *H-k* stacking result at SC.LTA is show in Figure B.6b, which shows a well-defined peak at (H=57.8 km, *k* =1.803). We further compute the vespagram of the SV receiver functions to measure the slowness of the Ps and the multiples. To do so, we stacked the receiver functions with linear moveout corrections corresponding to a range of slownesses (e.g., Kawakatsu and Niu, 1994). The measured slowness of the Ps and multiples are negative and positive (Figure B.6c), respectively, which is expected due to the slight differences in ray paths with respect to the direct P wave.

B.4. Results and Discussion

We obtained 78 measurements of crustal thickness (*H*) and 74 measurements of *Vp/Vs* ratio (*ê)* from the 79 stations. The results are listed in Table B.1. The table is organized by grouping stations in the following tectonic/physiographic regions (Figure B.7): the Sichuan Basin (SB), the Tibetan plateau (TP); the Yungui plateau (YG); the Western Yunnan Fold Belts (WB), which include the Tengchong block, Changning-Menglian Belt, Lanping-Simao Fold System, Ailaoshan Belt; and the South China Fold System (SF). We further computed Moho depth from the sea level *(D)* by subtracting station elevations from the measured *H*. The measured Moho depth and *Vp/Vs* ratio are further interpolated into meshed 0.2°x0.2° grids of the study area between 21.0°N to 30.4°N in latitude and 98.0°E to 106.0°E in longitude. The interpolation is performed to fit a flattest Moho with an inversion method (Niu et al., 2007). There are 41 and 48 grid points in the longitudinal and latitudinal directions, respectively, within the study area.

This gives a total of 1968 unknown parameters of *D* and *k*, which are inverted from the 78 and 74 observations, respectively. A regularization that minimizes the first derivative of the model is added to regularize the underdetermined inversion. The results are shown in Figure B.7. Since there are essentially no stations in the southeast and southwest corner of the study area, the maps may not reflect the true values of the Moho depth and *Vp/Vs* ratio for these two corners.

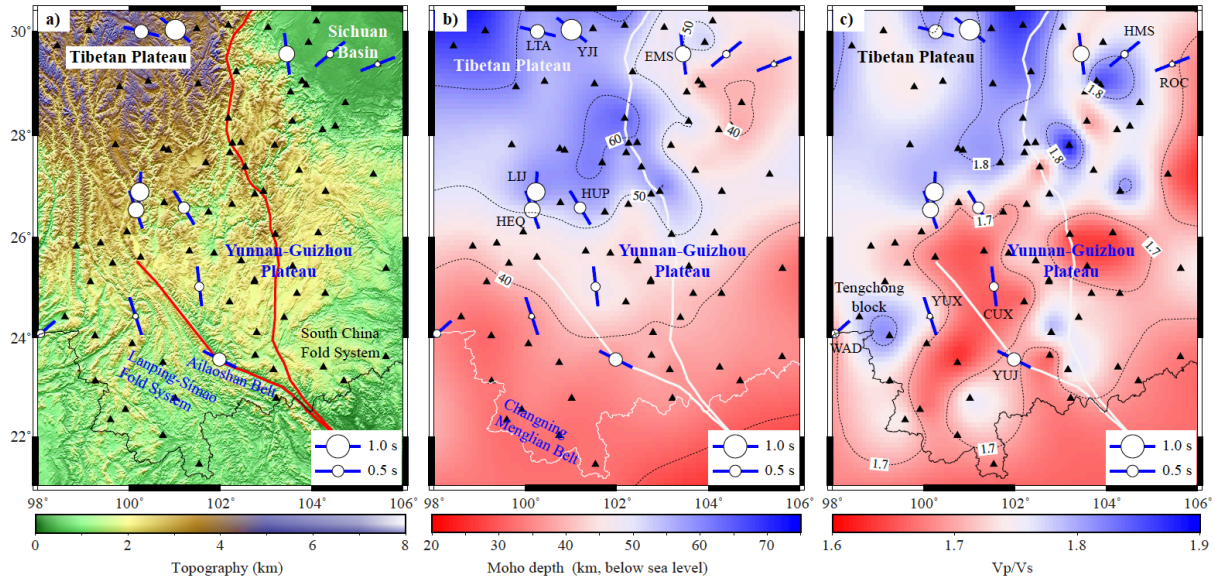

Figure B.7. Maps showing the surface topography (a), Moho topography (b), and the lateral variations of the *Vp/Vs* ratio (c), respectively. The color contour is calculated from observations at stations shown by black triangles. Note the large contrast in Moho depth and *Vp/Vs* ratio between the Tibetan plateau and the rest of the study area. In particular, the Tibetan plateau shows a higher *Vp/Vs* (~1.79) ratio than the Yungui plateau (~1.69), suggesting that it has relatively more mafic lower crustal materials. Also shown on the map are the 12 measurements of the fast directions and splitting times. The fast-axis direction is shown by a bar line, and the amount of splitting is indicated by the size of the circle plotted at the location of each station.

Note the large splitting times from the 6 stations located at the SE Tibetan plateau. Station YUJ (YN.YUJ) located near the Red River fault also shows a large splitting time (0.58 s).

We also include measurements from 9 PASSCAL stations in the interpolation. 8 stations (MC04, MC07, MC13, MC10, MC12, MC18, MC21 and MC25) were installed by MIT/CIGMR and another 1 station (ES28) was deployed by Lehigh University in 2003 and 2004. Xu et al. (2007) analyzed the receiver function data recorded by the MIT/CIGMR array and estimated crustal thickness and average crustal *Vp/Vs* beneath 22 stations. In general, our measurements are in good agreement with their results. The measured crustal thickness here is also consistent with the results of surface wave studies by Yao et al. (2008; 2010).

B.4.1. Moho Depth

We have a total of 13 stations (including 3 PASSCAL stations) located on the core part of the Tibetan plateau with an elevation above 2500 meters in western Sichuan province. The estimated Moho depth varies from 48.8 km to 71.1 km, with an average depth of 61 km, which is significantly higher than the surrounding regions. The thinnest crust in the study area is found at the southwestern border on the Changning-Menglian Belt, which is about 32 km. A moderately thick crust also underlies stations located on the South China Fold System with a Moho depth in the range of 35.1 to 38.3 km (Table B.1, Figure B.7). Moving toward the north, in the Yunnan-Guizhou plateau, which has an elevation of ~1.7 km, the crust thickens from ~41 km in the south to ~50 km at its northern border (Table B.1, Figure B.7). The thinnest crust within the Sichuan Basin is found at its southern end, with a thickness of approximately 40 km. The Moho beneath the basin deepens gradually towards northwest, and reaches to more than 50

km at its northwestern edge (Table B.1, Figure B.7). All of the receiver functions show significant P to S conversion and multiple reflections between the free surface and the sedimentary-bedrock boundary located at a few to ten kilometers beneath the surface. Watson et al. (1987) suggested that the Sichuan plateau is a flexural basin controlled by southeastward thrusting along its northwestern margin. The observed thickening of the sedimentary cover and crustal thickness towards the northwest agrees with their interpretation of the origin of the Sichuan basin. Overall we observe a gradual thickening of the continental crust from southeast to northwest (Figure B.7b).

B.4.2. Vp/Vs ratio

The measured *Vp/Vs* ratio also shows significant differences between the Tibetan plateau and its surrounding areas, especially the Yungui plateau. The average *Vp/Vs* ratio calculated from the 13 stations with high elevation (>2500 m) is 1.79, while *Vp/Vs* ratio averaged over the stations located on the Yungui plateau is only 1.69 (Table B.1, Figure B.7c). We observe a wide range of *Vp/Vs* ratios across the Sichuan basin (Table B.1, Figure B.7c). We attribute such a variation to the changes in sediment thickness within the basin. In general, sediment has a very high *Vp/Vs*, and the measured *Vp/V*s ratio is a weighted average between sediment and the igneous bedrocks in a crustal column. When the proportion of sediment in the column is high, then the estimated *Vp/Vs* ratio is expected to be high. For example, the western part of the basin has a thick sediment cover; the observed *Vp/Vs* ratio there is much higher than that of the eastern side of the basin. According to Pan and Niu (2011), the NE margin of the Tibetan plateau, north to the study area here, also shows a very low crustal *Vp/Vs* ratio, ~1.69, nearly similar to the one observed beneath the Yungui plateau. Therefore, comparing to the surrounding area, the SE

Tibetan crust has a distinct *Vp/Vs* ratio. We further argue this difference is likely caused by composition.

The ratio of compressional to shear wave velocities has been found by laboratory studies to be useful in constraining the composition of material sampled by seismic waves as varying compositions can have similar *Vp* or *Vs* values but different *Vp/Vs* (e.g., Christensen, 1996). The relative abundance of quartz (*Vp/Vs* = 1.49) and plagioclase (*Vp/Vs* = 1.87) has a dominant effect on the *Vp/Vs* ratio of common igneous rocks and their metamorphosed equivalents. An increase in plagioclase content or a decrease in quartz content can increase the *Vp/Vs* ratio of a rock. For example, the *Vp/Vs* ratio increases from 1.710 for granitic rock, to 1.78 for diorite, and to 1.87 for gabbro (Tarkov and Vavakin, 1982). Mafic/ultramafic igneous rocks generally have high *Vp/Vs* ratios because they usually contain gabbro and peridotite or dunite. On the other hand, felsic rocks possess a large amount of quartz, and consequently have a relatively low *Vp/Vs* ratio. Christensen (1996) also found that *Vp/Vs* seems to be insensitive to temperature when temperature is far below the solidus. However, when temperature is close enough to the solidus to generate partial melt, the *Vp/Vs* ratio is highly sensitive to the amount of melt. Watanabe (1993) found that *Vp/Vs* increases significantly with increasing melt fraction, and can reach to 2 when melt fraction is above 10 vol.%.

Therefore, the large difference in *Vp/Vs* ratio between the SE Tibet and its surrounding areas can be caused by a difference in composition or melts, i.e., the crust beneath the SE Tibetan plateau either is more mafic on average or contains more melts in comparing with the other regions, especially the Yungui plateau. Although our data have no resolution on this ambiguity,

there are at least two lines of evidence that suggest melt content is less likely the cause here. First, the SE Tibet, Yungui plateau and NE Tibet have roughly the same heat flux, suggesting that the thermal structure of the three regions is comparable. Second, the measured seismic velocity beneath the SE Tibet (e.g., Wang et al., 2003; Yao et al., 2010) is not at a low enough level to indicate significant partial melting. We thus conclude that the average composition of the SE Tibetan crust is more mafic, as compared to the crust beneath the Yungui plateau. In other words, a crustal column taken from the SE Tibetan plateau contains a larger portion of mafic lower crustal materials.

B.4.3. Crustal anisotropy

As mentioned in the discussion, measuring shear wave splitting with receiver function data is really challenging due to the low SNR of the Moho Ps conversion phase. We have applied both harmonic and statistical analyses to ensure that the estimated splitting parameters are not artifacts. As a result, we are able to obtain only 12 measurements from the 79 stations, which are shown in Figure B.7 and listed in the Table B.1 (bold italic). We should point out here that for a weak anisotropic or an isotropic medium, the Ps arrival is not expected to show a degree-2 azimuthal variation, and the difference between receiver functions before and after the correction of seismic anisotropy, which lies at the center of the SNR test of Liu and Niu (2012), is expected to be insignificant. These stations were not included in our count. There are 13 stations (Table B.1) with a measured splitting time less than 0.2 s, suggesting that the crust beneath these stations is weakly anisotropic or isotropic. These 13 stations are located inside the Sichuan basin (2), the Yungui plateau (5), the western Yunnan fold systems and belts (4), and the South China fold system (2).

The measured delay times from the 12 stations vary between 0.24 s to 0.9 s, with an average of 0.53. The delay times appear to increase with the Ps arrival time relative to the direct P wave (Figure B.8). The differential travel time between the Ps conversion phase and the direct P, dt_{Ps-P}, roughly equals to the subtraction of the P-wave travel time from the S-wave travel time in the crust. The S-wave travel time of the Ps conversion phase inside the crust is approximately 2.2 times of dt_{Ps-P}. We have also shown the predicted delay times of two anisotropic models in Figure B.8. The dotted lines is the predicted splitting time of the Ps arrival with a 5% seismic anisotropy uniformly distributed within the whole crust, while the solid line is the prediction based on an anisotropic model with 6% azimuthal anisotropy (~0.0165 s per kilometer) being evenly distributed inside the lower crust 15 km below Earth's surface. Mica and amphibole are two strongly anisotropic crustal minerals. Tatham et al. (2008) found that amphibole tends to align preferentially through deformation and can generate up to 13% seismic anisotropy under strong shear. Thus the observed 6% seismic anisotropy can be caused by lattice preferred orientation (LPO) of amphibole associated with the lower crustal flow. On the other hand, Lloyd et al. (2009) found that composite S-C fabrics are usually developed when micaeous rocks are naturally deformed, and the estimated seismic anisotropy of the S-C fabrics is between 5.8% and 7.5%. They further found that mixtures of multiple foliations could generate significant variations in the geometry of the seismic anisotropy. If this is the case then it is difficult to generate the observed 6% azimuthal anisotropy with mica fabrics.

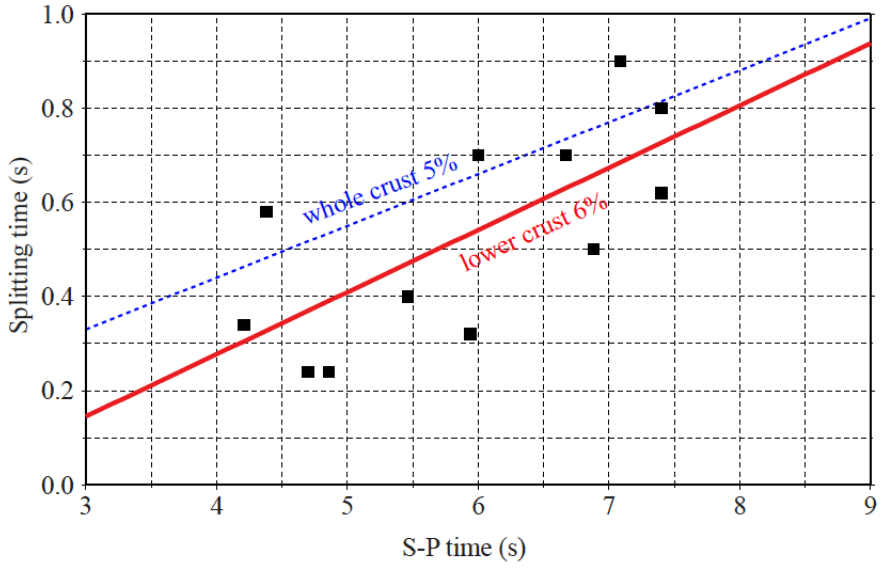

Figure B.8. Splitting times are shown as a function of the S-P travel time. Note the good correlation between the two. Dotted line shows the predicted splitting time from a model with 5% azimuthal anisotropy distributed evenly in the whole crust. The solid line is the prediction from a model with 6% seismic anisotropy only inside the lower crust (defined between 15 km deep and the Moho).

The average splitting time of the 12 measurements is 0.53 s, very close to the 0.58 s averaged delay time measured from the SKS/SKKS data recorded by the MIT/CIGMR array (Lev et al., 2006). The splitting time averaged from the stations located on the Tibetan plateau and its eastern edge is 0.70 s (Figure B.7), which is comparable to the ~ 1s global average of SKS/SKKS splitting time, and is also consistent with the surface wave data by Yao et al. (2010), who observed a ~1s azimuthal anisotropy inside the crust of the SE Tibetan plateau. A station-by-station comparison of the fast polarization direction and splitting time between our measurements and the SKS/SKKS results (Lev et al., 2006) can be found in Table B.1. We find

that the 6 stations located on the Tibetan plateau have a fast polarization similar or very close to, and a delay time comparable to the SKS/SKKS measurements. The agreement between the SKS/SKKS and receiver function data suggests that crustal anisotropy is likely the major source of the observed shear wave splitting of the core phases SKS and SKKS. Lev et al. (2006) found a prominent transition in the SKS/SKKS fast polarization direction at the latitude of ~26°N. We have 4 stations located in the southern region that showed an average azimuthal anisotropy of ~0.39 s. The largest splitting time (0.58 s) is observed at station YN.YUJ, which is located near the Red River fault (Figure B.7). The fault is known to have an annual slip rate of ~7 mm per year (Shen et al., 2005), and the observed large splitting is likely the result of the accumulated simple shear along the fault. Neither the measured fast polarization direction nor the observed splitting times match with the SKS/SKKS results, which showed a dominant EW fast polarization direction with delay times between 0.28 and 0.75 s (Lev et al., 2006).

The good agreement of the shear wave splitting measured from the two radially polarized S-wave conversions at the core-mantle boundary (SKS) and the Moho (Pds) at stations on the SE Tibetan plateau provides a strong constraint on the deformation style in the crust and mantle, as well as on possible mechanisms for how the plateau has been uplifted. First, the combination of our results with the SKS data suggest that the upper mantle beneath the SE Tibetan plateau has little to no azimuthal anisotropy. This is inconsistent with the surface wave study of Yao et al. (2010), which found that the mantle lithosphere has some azimuthal anisotropy with a fast polarization direction different from that of the crust. In principle, a depth varying anisotropy is measurable with SKS splitting data, if there is enough sampling from events that occurred over a wide range of back azimuths. This azimuthal coverage could be difficult to achieve with a one

or two-year temporary deployment, such as the MIT/CIGMR array (Lev et al., 2006), but it eventually will become possible with the CEA permanent station data. We will leave it to future studies to resolve this issue. We share the same interpretation with Yao et al. (2010) in the sense that the crust and mantle beneath the plateau are likely to be decoupled, and have a different deformation style.

In summary, we found two distinct features on the crust beneath the SE Tibetan plateau: 1) a thick crust with a relatively high *Vp/Vs* ratio; 2) the crust is strongly anisotropic, with a fast direction roughly parallel to the direction of the maximum horizontal tensile stress. These seismic observations provide strong constraints on the nature of deformation beneath the SE Tibet. In fact, both observations point to a scenario that lower crustal flow is present beneath the SE Tibetan plateau (Figure B.9).

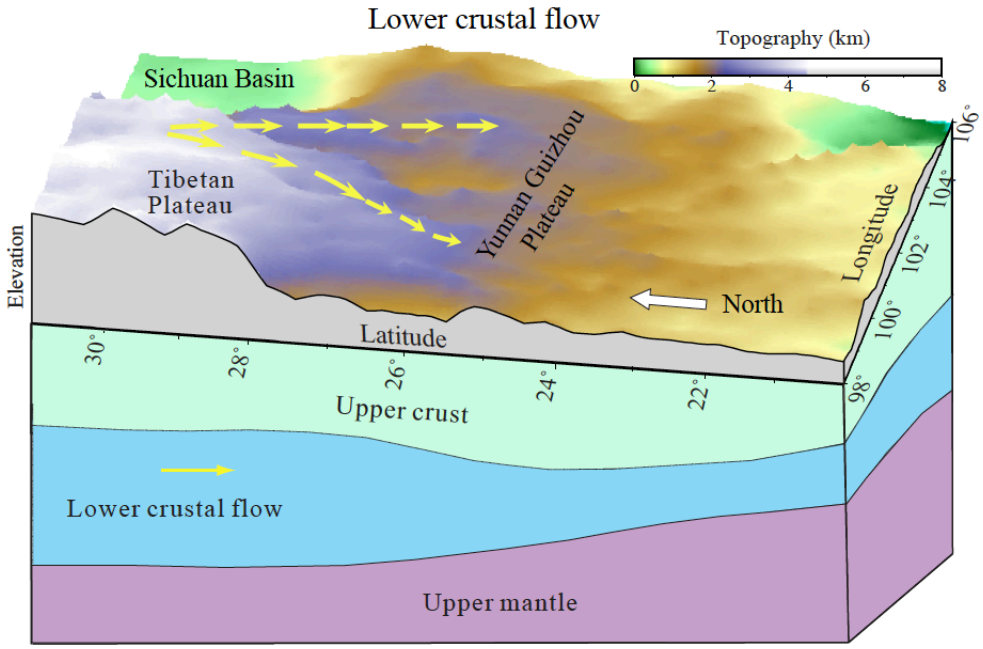

Figure B.9. Cartoon shows the lower crustal flow model and its prediction on the crustal structure and deformation style. Topographic profiles along the west and south sides of the study area are shown in black lines.

We have argued that the SE Tibetan crust is more mafic in composition than the crust beneath the Yungui plateau based on the observed *Vp/Vs* ratio. Now the question is whether the composition difference is inherited during the initial stage of crustal formation or is developed in the late stage of crustal thickening. Although it is almost impossible to use seismic data to argue which one is true, we have some indirect evidence that suggests the difference might have been developed during crustal thickening. First, as mentioned above, to the north of the study area, the NE margin of the Tibetan plateau also has a low *Vp/Vs* ratio of ~1.69, which may suggest that the initial crust in the study area is rather felsic. If this is the case, then the thickened crust is unlikely caused by whole crustal shortening, as the process preserves the felsic composition of the original crust, and consequently can not explain the high *Vp/Vs* ratio. On the other hand, the lower crustal flow model can readily explain the elevated *Vp/Vs* ratio of the SE Tibetan crust. According to Clark and Royden (2000), lower crust materials flow from the center of the Tibetan plateau to its edge due to an elevation-induced pressure contrast between the plateau and its surroundings. Hacker et al. (2000) studied the deep crustal xenoliths from the central Tibetan plateau and found that the xenoliths were erupted from a depth of 30 to 50 km and were comprised of mafic rocks and siliciclastic metasedimentary rocks. The calculated Poisson's ratios of the xenoliths are ~0.27, equivalent to a *Vp/Vs* ratio of ~1.78. Adding these mafic rocks to the original felsic crust can boost the *Vp/Vs* ratio to the observed level of ~1.79.

The S-wave ray path of the Moho Ps conversion goes from the Moho to the surface, and the anisotropy can in principle be anywhere along the path. As the fast direction is almost perpendicular to the direction of the maximum horizontal compressional stress, we argue that it is unlikely caused by stress-induced alignment of cracks in the upper crust above ~15 km, and more likely results from fabric structure developed in the lower crust below ~15 km. To produce the amount of seismic anisotropy, a moderate to strong shear is required. Again, the existence of such shear zones is consistent with the lower crustal flower model.

Our results, combined with the SKS data, can also offer some insights into mantle processes beneath the plateau. The simplest interpretation is that the mantle has little deformation. The other possibility is that vertical flow is the primary mode of mantle deformation, and partial lithosphere removal may have been occurring beneath this part of the Tibetan plateau. This is consistent with recent study of Niu (2011), which measured the depth of the lithosphere and asthenosphere boundary (LAB) beneath China with ScS reverberation data and found that the lithosphere beneath the study area is very thin (~80-100 km). Since the crust is 50-70 km thick beneath the SE Tibet plateau, the mantle lithosphere here is only 10 to 50 km thick. If the original mantle lithosphere is ~100-150 km thick, then a large portion of the mantle lithosphere must have been removed. Studies of rock mechanics indicated that most of the strength of continental lithosphere is contained in two separate strong zones, one in the upper crust and one in the upper mantle (e.g., Brace and Kohlstedt, 1980). It has been shown that an increase in crustal thickness or a decrease in lithosphere thickness can reduce the overall strength of the lithosphere (Dunbar and Sawyer, 1988). We speculate that the high level of seismicity observed

in the study region reflects the weakness of the lithosphere, which is made up primarily of crust rocks.

B.5. Conclusion

We investigate crustal structure and seismic anisotropy beneath the SE Tibetan plateau and its surrounding areas with receiver function data. We find that the crust beneath the SE Tibetan plateau has a thickness of ~50-70 km and a relatively high *Vp/Vs* ratio of ~1.79. The latter suggests that mafic lower crustal materials compose a significant portion of the crust beneath the SE margin of the Tibetan plateau. We also find that the crust beneath the SE Tibetan plateau is highly anisotropic, with fast polarization directions and splitting times comparable to those measured from SKS/SKKS data, suggesting that deformation in the upper mantle is either very weak or primarily in the vertical direction, and different from those seen in the crust. These observations are consistent with a scenario of lower crustal extrusion beneath the margin.

LIST OF REFERENCES

Ammon, C.J. (1991), The isolation of receiver effect from teleseismic p waveforms. Bull. seism. Soc. Am. 81, 2504-2510.

Alkhalifah, T. (1998), Acoustic approximations for processing in transversely isotropic media: Geophysics, 63, 623-631.

Bai, D., Unsworth, M.J., Meju, M.A., Ma, X., Teng, J., Kong, X., Sun, Y., Sun, J., Wang, L., Jiang, C., Zhao, C., Xiao, P., and Liu, M. (2010), Crustal deformation of the eastern Tibetan plateau revealed by magnetotelluric imaging. Nature Geosciences. 3, 358-362, doi:10.1038/ngeo830.

Baysal, E., Kosloff, D.D., and Sherwood J.W.C. (1983), Reverse time migration: Geophysics, 48, 1514-1524.

Bianchi, I., Park, J., Piana Agostinetti, N., and Levin, V. (2010), Mapping seismic anisotropy using harmonic decomposition of receiver functions: An application to Northern Apennines, Italy, J. Geophys. Res., 115, B12317, doi:10.1029/2009JB007061.

Billette, F.J., and Brandsberg-Dahl, S. (2005), The 2004 BP velocity benchmark: 67th Conference and Exhibition, EAGE, Extended Abstracts, B035.

Bowman, J.R., and Ando, M. (1987), Shear-wave splitting in the upper-mantle wedge above the Tonga subduction zone, Geophys. J. R. Astron. Soc., 88, 25-41.

Carcione, J.M., Herman, G.C., and Kroode, A.P.E. ten (2002), Seismic modeling: Geophysics, 67, 1304-1325.

Chen, Y.L., Niu, F., Liu, R.F., Huang, Z.B., and Tkalcic, H. (2010), Crustal structure beneath China from receiver function analysis. J. Geophys. Res. 115, B03307. doi:10.1029/2009JB006386.

Christensen, N.I. (1996), Poisson's ratio and crustal seismology, J. Geophys. Res. 101, 3139-3156.

Clark, M.K., and Royden, L.H. (2000), Topographic ooze: building the eastern margin of Tibet by lower crustal flow, Geology, 28, 703–706.

Clark, M.K., House, M.A., Royden, L.H., Whipple, K.X., Burchfiel, B.C., Zhang X., and Tang, W. (2005), Late Cenozoic uplift of southeastern Tibet, Geology, 33, 525-528, doi: 10.1130/G21265.1.

Clayton, R.W., and Engquist, B. (1977), absorbing boundary conditions for acoustic and elastic wave equations: Bulletin Seismological Society of America, 67, 1529-1540.

Clayton, R.W., and Wiggins, R.A. (1976), Source shape estimation and deconvolution of teleseismic body waves. Geophys. J. R. Astron. Soc., 47, 151-177(1976).

Crampin, S. (1987). Geological and industrial implications of extensive-dilatancy anisotropy, Nature, 328, 491-496.

Crampin, S., and Lovell, J.H. (1991), A decade of shear-wave splitting in the Earth's crust: what does it mean? what use can we make of it? and what should we do next?, Geophys. J. Int., 107, 387-407.

Crampin, S., and Chastin, S. (2003), A review of shear wave splitting in the crack-critical crust, Geophys. J. Int., 155, 221-240.

Dablain, M.A. (1986), The application of high-order differencing to the scalar wave equation: Geophysics, 51, 54-66.

Dai, N., Wu, W., Zhang W., and Wu, X. (2012), TTI RTM using variable grid in depth: IPTC 15050.

Dunbar, J. A., and Sawyer, D. (1988), Continental rifting at pre-existing lithospheric weaknesses. Nature 333, 450-452.

Etgen, J. (1986), High-order finite-difference reverse time migration with the 2-way non-reflecting wave equation: in SEP-48, 133-146, Stanford Exploration Project.

Etgen, J. (1989), Accurate wave equation modeling: in SEP-60, 131-148, Stanford Exploration Project.

Failly, M., Singh, S.C., and Hobbs, R.W. (1993), Lower crustal reflectivity from waveform inversion, 115, 410-420.

Fomel, S., Ying, L., and Song, X. (2012), Seismic wave extrapolation using lowrank symbol approximation: Geophysical Prospecting, 1-11.

Frederiksen, A.W., and Bostock, M.G. (2000), Modeling teleseismic waves in dipping anisotropic structures. Geophys. J. Int., 141, 401-412.

Fukao, Y., Widiyantoro, S., and Obayashi, M. (2001), Stagnant slabs in the upper and lower mantle transition region, Rev. Geophys. 39, 291-323.

Hacker, B.R., Gnos, E., Ratschbacher, L., Grove, M., McWilliams, M., Sobolev, S., Wan, J., and Wu Z.H. (2000), Hot and Dry Deep Crustal Xenoliths from Tibet, Science 287, 2463-2466.

Hahm, D., Hilton, D.R., Cho, M., Wei, H., and Kim, K.R. (2008), Geothermal He and CO2 variations at Changbaishan intra-plate volcano (NE China) and the nature of the sub-continental lithospheric mantle, Geophys. Res. Lett., 33, L12304, doi:10.1029/2008GL035955.

Hetland, E.A., Wu, F.T., and Song, J.L. (2004), Crustal structure in the Changbaishan volcanic area, China, determined by modeling receiver functions, Tectonophysics, 386, 157-175.

Hu, W.S., Cai, C.F., Wu, Z.Y., and Li, J.M. (1998), Structural style and its relation to hydrocarbon exploration in the Songliao Basin, northeast China, Marine and Petroleum Geol., 15, 41-55.

Iidaka, T., and Niu, F. (2001), Mantle and crust anisotropy in the eastern China region as inferred from waveform splitting of SKS and PpSms, Earth, Planets and Space, 53, 159-168.

Ichiki, M., Baba, K., Obayashi, M., and Utada, H. (2006), Water content and geotherm in the upper mantle above the stagnant slab Interpretation of electrical conductivity and seismic P-wave velocity models, Phys. Earth Planet. Inter., 155, 1-15.

Jenkins, G.M., and Watts D.G. (1968), Spectral Analysis and Its Applications, Holden-Day, San Francisco, Calif., 1968.

Kawakatsu, H., and Niu, F. (2004), Seismic evidence for a 920-km discontinuity in the mantle, Nature, 371, 301-305.

Kaneshima, S. (1990), Origin of crustal anisotropy: shear wave splitting studies in Japan, J. Geophys., Res., 95, 11121-11133.

Kennett, B.L.N., and Engdahl, E.R. (1991), Traveltimes for global earthquake location and phase identification, Geophys. J. Int. 105, 429-465.

Kuritani, T., Kimara, J., Miyamoto, T., Wei, H.Q., Shimano, T., Maeno, F., Jin, X., and Taniguchi, H. (2009), Intra-plate magmatism related to deceleration of upwelling asthenospheric mantle: Implications from the Changbaishan shield basalts, northeast China, Lithos 112, 247-258.

Lei, J.S., and Zhao, D.P. (2005), P-wave tomography and origin of the Changbai intraplate volcano in Northeast Asia, Tectonophysics, 397, 281-295.

Lev, E., Long, M. D., and van der Hilst, R.D. (2006), Seismic anisotropy in Eastern Tibet from shear wave splitting reveals changes in lithospheric deformation. Earth Plant. Sci. Lett. 251 293-304.

Levin, V., and Park, J. (1997), P-SH conversions in a flat-layered medium with anisotropy of arbitrary orientation. Geophys. J. Int., 131, 253-266.

Levin, V., Roecker S., Graham, P., and Hosseini, A. (2008), Seismic anisotropy indicators in Western Tibet: Shear wave splitting and receiver function analysis, Tectonophysics, 462, 99-108.

Li, J., and Niu, F. (2010), Seismic anisotropy and mantle flow beneath northeast China inferred from regional seismic networks. J. Geophys. Res. 115, B12327. doi:10.1029/2010JB007470.

Liu, H., Dai, N., Niu, F., and Wu, W. (2013), Effective acoustic wave extrapolation via optimum stencil. Geophysics, submitted.

Liu, H., and Niu, F. (2011), Receiver function study of the crustal structure of Northeast China: seismic evidence for a mantle upwelling beneath the eastern flank of the Songliao Basin and the Changbaishan region. Earth Science, 24, 1, 27-33.

Liu, H., and Niu, F. (2012), Estimating crustal seismic anisotropy with a joint analysis of radial and transverse receiver function data, Geophys. J. Int., 188, 144-164, doi:10.1111/j.1365-246X.2011.05249.x.

Liu, J.Q., Han, J.T., and Fyfe, W.S. (2001), Cenozoic episodic volcanism and continental rifting in northeast China and possible link to Japan Sea development as revealed from K-Ar geochronology, Tectonophysics, 339, 385-401.

Lloyd, G., Butler, R., Casey, M., and Mainprice, D. (2009), Mica, deformation fabrics and the seismic properties of the continental crust, Earth Planet. Sci. Lett., 288, 320–328, doi:10.1016/j.epsl.2009.09.035.

Mainprice, D., and Nicolas, A. (1989), Development of shape and lattice preferred orientations: application to the seismic anisotropy of the lower crust. J. Struct. Geol. 11, 175-189.

Masy, J., Niu, F., Levander, A., and Schmitz M. (2011), Mantle flow beneath northwestern Venezuela: Seismic evidence for a deep origin of the Mérida Andes, Earth planet. Sci. Lett., 305, 396-40, .doi:10.1016/j.epsl.2011.03.024.

McNamara, D.E., and Owens, T.J. (1993), Azimuthal shear wave velocity anisotropy in the Basin and Range Province using Moho Ps converted phases, J. Geophys. Res. 98, 12003-12017.

McNamara, D.E., Owens, T.J., and Silver, P.G. (1994), Shear wave anisotropy beneath the Tibetan Plateau, J. Geophys. Res. 99, 13655-13665.

Meade, C., Silver, P.G., and Kaneshima, K. (1995), Laboratory and seismological observations of lower mantle isotropy, Geophys. Res. Lett., 22, 1293– 1296.

Muirhead, K.J. (1968), Eliminating false alarms when detecting seismic events automatically. Nature. 217, 533-534.

Nagaya, M., Oda, H., Akazawa, H., and Ishise, M. (2008), Receiver Functions of Seismic Waves in Layered Anisotropic Media: Application to the Estimate of Seismic Anisotropy, Bull. seism. Soc. Am., 98, 2990-3006.

Nair, S.K., Gao, S.S., Liu, K.H., and Silver, P.G. (2006), Southern African crustal evolution and composition: Constraints from receiver function studies, J. Geophys. Res., 111, B02304, doi:10.1029/2005JB003802

Nicolas, A., and Christensen, N.I. (1987), Formation of anisotropy in upper mantle peridotites—A review, in Composition, Structure and Dynamics of the Lithosphere-Asthenosphere System, pp. 111 – 123, edited by K. Fuchs and C. Froidevaux, American Geophysical Union, Washington, D.C.

Niu, F. (2011), Mapping lithosphere thickness beneath China with ScS reverberation data: what controls the intraplate seismicity in Mainland China, Abstract S23E-02 presented at 2011 Fall Meeting, AGU, San Francisco, Calif., 5-9 Dec.

Niu, F., Bravo, T., Pavlis, G., Vernon, F., Rendon, H., Bezada, M., and Levander, A. (2007), Receiver function study of the crustal structure of the southeastern Caribbean plate boundary and Venezuela, J. Geophys. Res., 112, B11308, doi:10.1029/2006JB004802.

Niu, F., and James, D.E. (2002), Fine structure of the lowermost crust beneath the Kaapvaal craton and its implications for crustal formation and evolution. Earth Plant. Sci. Lett. 200, 121-130. doi:10.1016/S0012-821X 02 00584-8.

Niu, F., and Li, J. (2011), Component azimuths of the CEArray stations estimated from P wave particle motion. Earthquake Sci. 24: 3-13. doi:10.1007/s11589-011-0764-8.

Niu, F., and Kawakatsu, H. (1998), Determination of the absolute depths of the mantle transition zone discontinuities beneath China: effect of stagnant slabs on transition zone discountinuities, Earth, Planets and Space, 50(11-12), 965-975.

Niu, F., and Perez, A.M. (2004), Seismic anisotropy in the lower mantle: a comparison of waveform splitting of SKS and SKKS, Geophys. Res. Lett., 31, 10.1029/2004GL021196.

Pan, S., and Niu, F. (2011), Large contrasts in crustal structure and composition between the Ordos plateau and the NE Tibetan plateau from receiver function analysis, Earth Planet. Sci. Lett., 303, 291-298, doi:10.1016/j.epsl.2011.01.007.

Peng, X., and Humphreys, E.D. (1997), Moho dip and crustal anisotropy in northwestern Nevada from teleseismic receiver functions, Bull. seism. Soc. Am., 87, 745–754.

Ren, J.Y., Tanaki, K., Li, S.T., and Zhang, J.X. (2001), Late Mesozoic and Cenozoic rifting and its dynamic setting in Eastern China and adjacent areas, Tectonophysics, 344, 175-205.

Royden, L.H., Burchfiel, B.C., King, R.W., Wang, E., Chen, Z., Shen, F., and Liu Y. (1997), Surface deformation and lower crustal flow in eastern Tibet. Science 276, 788-790.

Savage, M.K. (1998), Lower crustal anisotropy or dipping boundaries? Effects on receiver functions and a case study in New Zealand, J. Geophys. Res., 103, 15069-15087.

Schoenbohm, L.M., Burchfiel, B.C., and Chen, L. (2006), Propagation of surface uplift, lower crustal flow, and Cenozoic tectonics of the southeast margin of the Tibetan plateau, 34, 813-816, doi: 10.1130/G22679.1.

Shen, Z.K., Lu. J.J., Wang, M., and Burgmann, R. (2005), Contemporary crustal deformation around the southeast borderland of the Tibetan plateau. J. Geophysical Res. 110, B11409, doi:10.1029/2004JB003421.

Shiomi, K., and J. Park, J. (2008), Structural features of the subducting slab beneath the Kii Peninsula, central Japan: Seismic evidence of slab segmentation, dehydration, and anisotropy, J. Geophys. Res., 113, B10318, doi:10.1029/2007JB005535.

Silver, P.G., and Chan, W.W. (1991), Shear wave splitting and subcontinental mantle deformation. J. Geophy. Res., 96, 16,429-16,454.

Silver, P.G. (1996), Seismic anisotropy beneath the continents: probing the depths of Geology, Annu. Rev. Earth Planet. Sci., 24, 385–432.

Song, X., and Fomel, S. (2011), Fourier finite-difference wave propagation: Geophysics, 76,T123-T129.

Soubaras, R., and Zhang, Y. (2008), Two-step explicit marching method for reverse time migration: 78th Annual International Meeting, SEG, Expanded Abstracts, 2272-2276.

Sun, Y., Niu, F., Liu, H., Chen, Y., and Liu, J. (2012), Crustal structure and deformation of the SE Tibetan plateau revealed by receiver function data, 349-350, 186-197.

Sun, Y., and Toksöz, M.N. (2006), Crustal structure of China and surrounding regions from P wave traveltime tomography, J. Geophys. Res., 111, B03310, doi:10.1029/2005JB003962.

Tal_Ezer, H., Kosloff, D., and Koren, Z. (1987), An accurate scheme for seismic forward modeling: Geophysical Prospecting, 35, 479-490.

Tapponnier, P., Peltzer, G., Le Dain, A.Y., Armijo, R., and Cobbold P. (1982), Propagating extrusion tectonics in Asia: New insights from simple experiments with plasticine. Geology 10, 611-616.

Tapponnier, P., Lacassin, R., Leloup, P.H., Schärer, U., Zhong, D., Wu, H., Liu, X., Ji, S., Zhang, L., and Zhong, J. (1990), The Ailao Shan/Red River metamorphic belt: Tertiary left-lateral shear between Indochina and South China, Nature 343, 431 - 437.

Tarantola, A. (1984), Inversion of seismic reflection data in the acoustic approximation: Geophysics, 49, 1259–1266.

Tarkov, A.P., and Vavakin, V.V. (1982), Poisson's ratio behavior in crystalline rocks: Application to the study of the Earth's interior, Phy. Earth Planet. Inter. 29, 24-29, doi:10.1016/0031-9201(82)90134-0.

Tatham, D.J., Lloyd, G.E., Butler, R.W.H., and Casey, M. (2008), Amphibole and lower crustal seismic properties. Earth Planet. Sci. Lett. 267, 118–128.

Thomsen, L. (1986), Weak elastic anisotropy: Geophysics, 51, 1954-1966.

Vinnik, L.P. (1977), Detection of waves converted from P to SV in the mantle, Phys. Earth Planet. Inter. 15, 39– 45.

Wang, C.Y., Chan, W.W., and Mooney, W.D. (2003), Three-dimensional velocity structure of crust and upper mantle in southwestern China and its tectonic implications, 108, B9, 2442, doi:10.1029/2002JB001973.

Watanabe, T. (1993), Effects of water and melt on seismic velocities and their application to characterization of seismic reflectors, Geophys. Res. Lett. 20, 2,933-2936.

Wang, C.Y., Flesch, L.M., Silver, P.G., Chang, L.J., and Chan, W.W. (2008), Evidence for mechanically coupled lithosphere in central Asia and resulting implication. Geology. 36, 363-366, doi:10.1130/G24450A.1.

Whitmore, N.D. (1983), Iterative depth migration by backward time propagation: 53rd Annual International Meeting, SEG, Expanded Abstracts, 382-385

Wolfe, C.J., and Silver, P.G. (1998), Seismic anisotropy of oceanic upper mantle: shear wave splitting methodologies and observations. J. Geophys. Res., 103, 749–771.

Xu, L., Rondenay, S., and van der Hilst, R.D. (2007), Structure of the crust beneath the southeastern Tibetan plateau from teleseismic receiver functions. Phys. Earth Planet. Inter. 165, 176-193.

Yao, H., Beghein, C., and van der Hist, R.D. (2008), Surface wave array tomography in SE Tibet from ambient seismic noise and two-station analysis: II. Crustal and upper-mantle structure. Geophys. J. Int., 163, 205-219, doi: 10.1111/j.1365-246X.2007.03696.x.

Yao, H., Van der Hilst, R.D., and Montagner, J.P. (2010), Heterogeneity and anisotropy of the lithosphere of SE Tibet from surface wave array tomography, J. Geophys. Res. 115, B12307, doi: 10.1029/2009JB007142.

Yin, A., and Harrison, T.M. (2000), Geologic evolution of the Himalayan-Tibetan orogen, Annu. Rev. Earth Planet Sci. 28, 211-280.

Zhao, D.P., Tian, Y., Lei, J.S., Liu, L., and Zheng, S.H. (2009), Seismic image and origin of the Changbai intraplate volcano in East Asia: Role of big mantle wedge above the stagnant Pacific slab, Phys. Earth Planet. Inter., 173, 197-206.

Zhang, Y., and Zhang, G. (2009), One-step extrapolation method for reverse time migration: Geophysics, 74, A29-A33

Zheng, X.F., Ouyang, B., Zhang, D.N., Yao, Z.X., Liang, J.H., and Zheng, J. (2009), Technical system construction of Data Backup Centre for China Seismograph Network and the data support to researches on the Wenchuan earthquake. Chinese J. Geophys. (in Chinese), 52(5):1412~1417, DOI:10.3969/j.issn.0001-5733.2009.05.031.

Zhu, L.P., and Kanamori, H. (2000), Moho depth variation in southern California from teleseismic receiver functions, J. Geophys. Res., 105(B2), 2,969-2,980.

Zou, H.B., Fan, Q.C., and Yao, Y.P. (2008), U–Th systematics of dispersed young volcanoes in NE China: Asthenosphereupwelling caused by piling up and upward thickening of stagnant Pacific slab, Chemical Geology, 255, 134-142.